Dynamics of immersed objects in a dense granular medium

by

Bitang Kwrung Tripura
Roll No: 156107034

A thesis submitted
in Partial Fulfillment of the Requirements
for the Degree of
DOCTOR OF PHILOSOPHY.

Supervisor
Dr. K. Anki Reddy

Department of Chemical Engineering
Indian Institute of Technology Guwahati
Guwahati 781039, India.

June 2022

Dynamics of immersed objects in a dense granular medium

by

Bitang Kwrung Tripura
Roll No: 156107034

A thesis submitted
in Partial Fulfillment of the Requirements
for the Degree of
DOCTOR OF PHILOSOPHY.

Supervisor
Dr. K. Anki Reddy

Department of Chemical Engineering
Indian Institute of Technology Guwahati
Guwahati 781039, India.

June 2022

DECLARATION

I hereby certify that the work compiled in this thesis is the outcome of the research work, performed by myself, else stated, under the guidance of Dr K. Anki Reddy.

Any part of this work has not been submitted for the award of any degree, diploma, associate-fellowship, fellowship or it's equivalent to any university or institution.

Bitang Kwrung Tripura,
Registration No: 156107034
Department of Chemical Engineering
IIT Guwahati,
Guwahati-781039, Assam, India.
DATE: JUNE 2022

CERTIFICATE

It is certified that the work contained in the thesis entitled " *Dynamics of immersed objects in a dense granular medium*" by Mr Bitang Kwrung Tripura, a student of the Department of Chemical Engineering, IIT Guwahati was carried out under my supervision and has not been submitted elsewhere for the award of any degree.

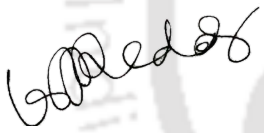

Dr K. Anki Reddy,
Department of Chemical Engineering, IIT Guwahati,
Guwahati-781039, Assam, India.
DATE: JUNE 2022

ACKNOWLEDGMENTS

First and foremost, I want to express my gratitude to Dr. K. Anki Reddy, my supervisor, without whom this thesis would not have been accomplished. During my research, his constant assistance, inspiration, and recommendations influenced my basic grasp of this topic to a large extent. I have learned a lot from him over my research career, and I expect to learn much more in the years ahead.

Apart from my supervisor, I would like to thank the members of my doctoral committee, Prof. Anugrah Singh, Dr. Rajesh Kumar Upadhyay, Dr. R Anandalaksmi, and Prof. Sitangshu Bikas Santra, for their valuable recommendations and insightful remarks throughout my research activities, which have kept me motivated. Further, special appreciation for the support staff of the Department of Chemical Engineering. I would also like to thank IITG for providing the HPC (PARAM-ISHAN) facility for performing my simulations and the Government of India. I want to extend my sincere gratitude to the Ministry of Human Resource Development and Indian Institute of Technology Guwahati for providing financial assistance, which reinforced me to study comfortably.

I would sincerely appreciate all my fellow lab-mates-friends: Mr. Rupam Sinha, Dr. Kuldeep Roy, Ms. Barnali Bhui, Dr. Ritesh Prakash, Mr. Shivam Tiwari, late Mr. Kranthi Kumar, Mr. Prashanth Tyagi, Mr. Aman, Mr. Raja Sekhar, Mr. Vasistha, Mr. Nagendra Prasad for their contributions towards my dissertation: be it providing valuable suggestions in manuscripts or assisting me in coding or any technical issues. I sincerely thank Dr. Vamsi Krishna Anyam and Mr. Sonu Kumar for enriching discussions, immense contributions, and valuable suggestions in my works. Without this group, my journey perhaps would have been less fun.

I do want to express my gratitude to my mother and father, Mrs. Himani Debbarma and Mr. Birendra Tripura, as well as my younger siblings Yakma Kwrung Tripura and Boris Tripura, for their unwavering love and support. I do want to express my heartfelt gratitude to my wonderful wife, Mrs. Rabina Debbarma, for her unwavering love and

support throughout this long trip. Finally, I'd want to express my gratitude to all of my other friends and family members who have consistently supported me during this wonderful trip.

Bitang Kwrung Tripura
Indian Institute of Technology Guwahati
November 2021

Abstract

This thesis investigates the motion of an intruder through a granular medium and interesting phenomena associaed with it. The continued efforts in understanding the motion of a solid object through a fluid medium has resulted in innovative designing of automobiles, aircraft, submarines etc. Similarly, the studies on the motion of a solid object through a granular medium can lead to designing vehicles or robots that can be used in rescue operations during andslides or snow avalanches or for exploring new terrains. In these types of studies, the prominent factors that affect the solid motion are drag and lift forces. These forces around a solid moving in the fluid medium has been understood well. However, the drag and lift forces on an intruder moving through a granular medium have been poorly understood. The reason for this is the complex nature of the granular medium which exhibits a wide variety of phenomena when subjected to external perturbations. A thorough understanding of the intruder's motion through granular medium helps in mining/drilling operations and designing automobiles that can move through sand or snow. To this end, three types of intruder's motion have been investigated: translation, oscillation and rotation.

Firstly, we studied the translational motion of the intruder. Most of the works in the recent past were dedicated to the comprehension of the spherical intruder moving through a granular medium. In our work, we studied the effect of the intruder's shape while it is translating through a system of circular particles. We observed that the drag force is minimally affected by the shape of the intruder provided their cross-section is kept constant. However, the lift force strongly depends on the shape of the intruder. The reason for this is as the shape of the intruder changes, the distribution of contacts around its surface changes, resulting in the variation of the net lift experienced by it. We further studied how the shape of the granular particles affect the translatory motion of an intruder as the granular systems in practice mostly comprise of non-spherical particles. To this end, we considered a system comprising of either discs or dumbbells or a mixture

of those two. The drag force increases with an increase in the fraction of dumbbells though the total mass of a dumbbell and a disc particle is kept constant. This is due to an additional resistance offered by the dumbbells owing to their geometry. Surprisingly, this additional resistance seems to disappear in the absence of inter-particle friction. Furthermore, we presented the mean flow fields of various parameters to understand the effect of particle dynamics surrounding the moving intruder. They revealed the presence of a cluster of particles in front of the intruder which plays a major role in determining the drag effects on it.

Then, we investigated the horizontal wiggling motion of an intruder in a granular medium. This work is inspired by the motion of sand-dwelling creatures which can penetrate through the sand by inducing wavy motion of their bodies. Previous studies have demonstrated that a horizontal oscillation of an intruder in the granular medium results in its vertical motion at certain amplitudes and frequencies of oscillation. In our work, we probed the shape of the intruder on its vertical motion and the rate of vertical displacement. The larger the intruder's top surface, the greater the rate of negative vertical displacement due to the additional stress from the particles above. The smaller the intruder's bottom surface, the greater the rate of positive vertical displacement. In addition, we proposed a mathematical model which predicts the intruder's motion with given oscillation parameters.

Finally, we studied the simultaneous translation and rotation motion of an intruder through a granular mixture of disc and dumbbell particles. We noticed an inverse-Magnus effect which has been observed previously in a system of discs. The lift force, which is responsible for inverse-Magnus effect, is noticed to increase with an increase in the fraction of dumbbells.

Table of Contents

Page

List of Figures **1**

List of Tables **9**

1 Introduction **11**

1.1 Granular materials 11

1.2 Locomotion in a granular medium 12

1.3 Drag in a granular medium 13

1.4 Lift in a granular medium 14

1.5 Objectives 15

Bibliography **17**

2 Simulation Method **19**

Bibliography **23**

3 Role of shape on the forces on an intruder moving through a dense granular medium **25**

3.1 Introduction 25

3.2 Simulation Methodology 27

3.3 Results and Discussion 29

3.3.1 Drag on the moving intruder 29

3.3.2 Number of contacts, kinetic drag, and drag regimes 34

3.3.3 Lift on the moving intruder 37

3.3.4 Depth-dependence of forces on the moving intruder 42

3.3.5 Force profile along the surface of the intruder 45

3.4 Conclusions 48

Bibliography **49**

4 Drag on a circular intruder traversing a shape heterogeneous granular mixture **53**

4.1 Introduction 53
4.2 Simulation Methodology 55
4.3 Results and Discussion 57
4.3.1 Dumbbell fraction 57
4.3.2 Absence of frictional forces 65
4.3.3 Area fraction 66
4.3.4 Diameter of the intruder 67
4.3.5 Mean flow fields 69
4.4 Conclusions 76

Bibliography **79**

5 Shape dependence on the rise and sink of a wiggling intruder **81**

5.1 Introduction. 81
5.2 Simulation methodology 84
5.3 Results and Discussion 85
5.3.1 Vertical displacement of oscillating intruder 86
5.3.2 Rate of rise of intruder with time-period 89
5.3.3 Average rate of vertical displacement of an intruder with phase angle 93
5.3.4 Drag force on oscillating intruder 95
5.3.5 Mean flow fields 96
5.3.6 Theoretical model 100
5.4 Conclusions 106
5.4.1 Vertical displacement of oscillating intruder 106
5.4.2 Rate of rise or sink of intruder with time-period 106
5.4.3 Average rate of vertical displacement of an intruder with phase angle 106
5.4.4 Mean flowfields 107

5.4.5 Theoretical Model 107

Bibliography **109**

6 Role of constituents of a granular medium on the lift force experienced by a translating and rotating intruder. **111**

6.1 Introduction. 111

6.2 Simulation Methodology 112

6.3 Results and Discussion 114

6.3.1 Translational and Rotational movement of the intruder 115

6.3.2 Area fraction 118

6.3.3 Force distribution around the intruder 120

6.3.4 Mean flowfields around the intruder 122

6.4 Conclusions 128

Bibliography **131**

7 Conclusions **133**

7.1 Scope for future work 134

List of Figures

2.1 The flowchart depicting the flow of operations in a DEM technique. Here 'N_{step}' corresponds to the total number of simulation timesteps, which vary depending on the problem of interest. 20

2.2 Two spherical particles i and j are in contact, with $\boldsymbol{r_i}$, $\boldsymbol{r_j}$ the positon vector, u_i u_j the velocity vector, and ω_i,ω_j the rotational velocity vector. F^n, and F^t are the normal and tangential components of contact forces and δ is the overlap between the two particles i and j. 21

3.1 The various shapes considered in our study. In the simulations they move from left to right. 27

3.2 Initial configuration for one of the shapes (backward triangle, S6) at a depth $h = 105d$. Periodic boundary conditions are applied in the x-direction. The system is confined by a wall at $y = 0$ composed of particles of size $1d$ (blue particles), while the top surface is unconstrained. The origin is located at the left bottom corner. 28

3.3 The variation of drag on an intruder with the velocity at (a) $\mu = 0$, (b) $\mu = 0.1$, and (c) $\mu = 0.5$ for all the shapes in our study on a log-log scale. The inset figures show $\psi = F_D/v^2$ for higher velocities. 30

3.4 The variation of drag on an intruder at low velocity in the range ($0.1\sqrt{dg}$ to $4\sqrt{dg}$) for μ (a) 0.0, (b) 0.1, and (c) 0.5 on a log-log scale for all the shapes. . 31

3.5 The variation of drag on an intruder with at intermediate to high velocity in the range ($5\sqrt{dg}$ to $20\sqrt{dg}$) for μ (a) 0.0, (b) 0.1, and (c) 0.5 on a semi-log scale for all the shapes. 31

3.6 The variation of the mean number of contacts N on an intruder with the velocity at (a) $\mu = 0$, (b) $\mu = 0.1$, and (c) $\mu = 0.5$ for all the shapes in our study. 33

3.7 The variation of lift on an intruder with the velocity at (a) $\mu = 0$, (b) $\mu = 0.1$, and (c) $\mu = 0.5$ for all the shapes in our study. 37

3.8 Snapshots showing the region around the $S2$(rectangle) intruder for $\mu = 0$ at different intruder velocities ($v/\sqrt{dg}$) (a) 1, (b) 8, (c) 12 and (d) 18. 38

3.9 Snapshots showing the region around the $S1$ (square) intruder for $\mu = 0$ at different intruder velocities ($v/\sqrt{dg}$) (a) 1, (b) 8, (c) 12 and (d) 18. 39

3.10 Snapshots showing the region around the $S3$ (disc) intruder for $\mu = 0$ at different intruder velocities ($v/\sqrt{dg}$) (a) 1, (b) 8, (c) 12 and (d) 18. 40

3.11 Snapshots showing the region around the $S4$ (an ellipse with major axis aligned with the x-direction) intruder for $\mu = 0$ at different intruder velocities ($v/\sqrt{dg}$) (a) 1, (b) 8, (c) 12 and (d) 18. 41

3.12 Snapshots showing the region around the $S5$ (ellipse with minor axis aligned with the x- direction) intruder for $\mu = 0$ at different intruder velocities ($v/\sqrt{dg}$) (a) 1, (b) 8, (c) 12 and (d) 18. 41

3.13 Snapshots showing the region around the $S6$ (equilateral triangle with edge pointing opposite to the moving direction) intruder for $\mu = 0$ at different intruder velocities ($v/\sqrt{dg}$) (a) 1, (b) 8, (c) 12 and (d) 18. 42

3.14 Snapshots showing the region around the $S7$ (equilateral triangle with edge pointing along the moving direction) intruder for $\mu = 0$ at different intruder velocities ($v/\sqrt{dg}$) (a) 1, (b) 8, (c) 12 and (d) 18. 43

3.15 The variation of drag force on an intruder at $\mu = 0.1$ with depth for (a) $v/\sqrt{dg} = 1$ and (b) $v/\sqrt{dg} = 5$ on a log-log scale. The dotted line represents a straight line of slope 1 on the log-log scale. The variation of lift force on an intruder at $\mu = 0.1$ with depth for (c) $v/\sqrt{dg} = 1$ and (d) $v/\sqrt{dg} = 5$ on a linear scale. 43

3.16 Geometric representation of four intruder shapes (a)S1 (a square), (b) S4 intruder (an ellipse with the major axis aligned with the direction of motion of the intruder), (c) S6 (an equilateral triangle with edge pointing opposite to the moving direction), and (d) S7 (an equilateral triangle with edge pointing along the moving direction). The contact position is given by the angle θ with $-\pi < \theta < \pi$ with the upper (lower)half corresponding to positive (negative) values. 45

3.17 The variation of (a) the normalized drag force ($F_{D,\theta}/F_D$) and (b) lift force ($F_{l,\theta}$) around the intruder surface for various intruder velocities. Please refer to Fig. 3.16 for the definition of θ. 46

4.1 One of the initial configuration of our system with an intruder placed at a depth of $h = 300\ cm$. Here, the green colour particles indicate dumbbells and the brown colour is that of discs. At $y = \pm 300$, the system is confined by walls made of glued particles (black) having a diameter of 1 cm. Whereas, in the x direction, periodic boundary conditions are applied. Note that the origin is located at the centre of the intruder. A zoomed in image of the region around the intruder is shown to the right side of the intial configuration. 55

4.2 The instantaneous drag force on the intruder (grey line) and its cumulative average (brown line) with respect to (a) time (s) and distance/d. Here, the coefficient of friction is $\mu = 0.5$, the intruder velocity $V_i = 10cm/s$, $\phi = 0.82$ and the intruder diameter $D_i = 5cm$ 57

4.3 (a) The time-averaged drag force F_D normalized by the square of intruder's velocity V_i , (b) the stress decline slope σ_s, and (c) the averaged number of particles in contact (N_c) as a function of intruder's velocity V_i for the fractions of dumbbells (db_{frac}) = 0, 0.5 and 1. The area fraction is $\phi = 0.82$, and the coefficient of friction is $\mu = 0.5$ and the diameter of the intruder is $D_i = 5\ cm$. 58

4.4 (a) The time-averaged drag force F_D as a function of intruder's velocity V_i , (b) the stress decline slope (σ_s) and (c) the averaged number of particles in contact (N_c) as a function of intruder's velocity V_i for the fractions of dumbbells (db_{frac}) = 0, 0.5 and 1. The area fraction is $\phi = 0.43$ and the coefficient of friction is $\mu = 0.5$ and the diameter of the intruder is $D_i = 5\ cm$. 58

4.5 (a) The time-averaged drag force F_D as a function of intruder's velocity V_i, (b) the stress decline slope (σ_s) and (c) the averaged number of particles in contact (N_c) as a function of intruder's velocity V_i for the fractions of dumbbells (db_{frac}) = 0, 0.5 and 1. The area fraction is $\phi = 0.77$ and the coefficient of friction is $\mu = 0.5$ and the diameter of the intruder is $D_i = 5\ cm$. 59

4.6 The two possible type of contacts in a dumbbell-dumbbell or dumbbell-disc interaction. a) The two parts of a dumbbell are simultaneously in contact with a disc or one part of another dumbbell. b) Only one part of a dumbbell is in contact with a disc or one part of another dumbbell. Here, the green ones represent dumbbells and the pink ones that of discs. 59

4.7 The magnitude of stress σ as a function of distance infront of the intruder surface (a) for different db_{frac} and ϕ 0.82 , (b) for different intruder velocity V_i with system having $db_{frac} = 0.5$ and ϕ 0.82, (c) for $V_i = 10cm/s$ at different area fraction ϕ with system having $db_{frac} = 0.5$ and (d) for different intruder diameter (D_i) with $\phi = 0.77$. The coefficient of friction is $\mu = 0.5$ in all the cases and the intruder diameter $D_i = 5cm$ is for system in plots (a), (b,) and (c). 60

4.8 The probability distribution function Ψ of the stress σ experienced by the intruder for four different velocities of the intruder V_i (a) 0.5 cm/s (b)2 cm/s (c) 10 cm/s and (25 cm/s). Here, $db_{frac} = 0$, and 1 are the fraction of dumbbells in the system. 61

4.9 The average number of particles in contact N_{c_θ} as a function of angular position (θ) for the fraction of dumbbells db_{frac} = a) 0.0, b) 0.5 and c) 1.0. The average pressure P_θ as a function of angular position at different intruder velocities V_i for the fraction of dumbbells db_{frac} = d) 0.0, e) 0.5 and f) 1.0. The coefficient of friction is $\mu = 0.5$, the area fraction is $\phi = 0.82$, and the inset in (e) displays how the angular positions are calcuated around the intruder surface. 62

4.10 The average number of particles in contact N_{c_θ} as a function of angular position (θ) for the fraction of dumbbells db_{frac} = a) 0.0, b) 0.5 and c) 1.0. The average normalised pressure P_{theta}/P_i as a function of angular position at different intruder velocities V_i for the fraction of dumbbells db_{frac} = d) 0.0, e) 0.5 and f) 1.0. The coefficient of friction is $\mu = 0.0$, the area fraction is $\phi = 0.82$ and the inset in (f) displays how the angular positions are calcuated and P_i denotes the pressure experienced by the intruder. 63

4.11 (a) The time-averaged drag force F_D, (b) the stress decline slope σ_s, and (c) the averaged number of particles in contact (N_c) as a function of intruder's velocity V_i for the fractions of dumbbells (db_{frac}) = 0, 0.5 and 1. The coefficient of friction is $\mu = 0.0$, the area fraction is $\phi = 0.82$, and the diameter of the intruder is $D_i = 5\ cm$. 64

4.12 (a) The time-averaged drag force F_D, (b) the stress decline slope σ_s, and (c) the number of contacts (N_c) as a function of the intruder's velocity V_i for systems with area fraction of (ϕ) = 0.43, 0.77 and 0.82. The fraction of dumbbells (db_{frac}) is 0.5, the diameter of the intruder (D_i) is 5 cm, and the coefficient of friction (μ) is 0.5. 67

4.13 (a) The time-averaged drag force F_D, (b) the drag force normalised by the intruder's diameter (F_D/D_i), (c) the stress decline slope σ_s, and (d) the number of particle contacts (N_c) as a function of the intruder's velocity V_i for different diameters of the intruder (D_i). The fraction of dumbbells (db_{frac}) is 0.5, the area fraction of the system (ϕ) is 0.77, and the coefficient of friction (μ) is 0.5. 68

4.14 The time-averaged flow fields for depicting pressure $P(dyne/cm^2)$, velocity $V(cm/s)$ and shear stress $|\sigma_{xy}|(dyne/cm^2)$ infront of the intruder for different fractions of dumbbells (db_frac): (a), (d), (g) 0.0, (b) (e), (h) 0.5 and (c), (f), (i) 1.0. The modulus of σ_{xy} is basically the magnitude of shear stress. The diameter of the intruder is $D_i = 5cm$, $V_i = 5cm/s$, the coefficient of friction $\mu = 0.5$, and the area fraction (ϕ) of the system is 0.82. 70

4.15 The time-averaged flow fields for depicting pressure $P(dyne/cm^2)$, velocity $V(cm/s)$ and shear stress $|\sigma_{xy}|(dyne/cm^2)$ infront of the intruder for different intruder diameter (D_i): (a), (d), (g) 1cm, (b) (e), (h) 5cm and (c), (f), (i) 10cm. The velocity of the intruder is $V_i = 5cm/s$, $\mu = 0.5$, $\phi = 0.77$, and the fraction of dumbbell (db_{frac}) in the system is 0.5. 71

4.16 The time-averaged flow fields for depicting pressure $P(dyne/cm^2)$, velocity $V(cm/s)$ and shear stress $|\sigma_{xy}|(dyne/cm^2)$ infront of the intruder for different fractions of dumbbells(db_frac): (a), (d), (g) 0.0, (b) (e), (h) 0.5 and (c), (f), (i) 1.0. The modulus of σ_{xy} is basically the positive value (or absolute value) of shear stress. The velocity of the intruder is $V_i = 5\ cm/s$, the coefficcient of friction $\mu = 0.0$, and the area fraction (a_{frac}) of the system is 0.82. 73

4.17 The time-averaged flow fields for depicting pressure $P(dyne/cm^2)$, velocity $V(cm/s)$ and shear stress $|\sigma_{xy}|(dyne/cm^2)$ infront of the intruder ($D_i = 5cm$) for different fractions of dumbbells (db_{frac}): (a), (d), (g) 0.0, (b) (e), (h) 0.5 and (c), (f), (i) 1.0. The velocity of the intruder is $V_i = 5\ cm/s$, $\mu = 0.5$ and the area fraction (ϕ) of the system is 0.77. 74

4.18 The time-averaged flow fields for depicting pressure $P(dyne/cm^2)$, velocity $V(cm/s)$ and shear stress $|\sigma_{xy}|(dyne/cm^2)$ infront of the intruder ($D_i = 5cm$) for different area fractions (a_{frac}): (a), (d), (g) 0.43, (b) (e), (h) 0.77 and (c), (f), (i) 0.83. The velocity of the intruder is $V_i = 5\ cm/s$, $\mu = 0.5$ and the dumbbell fraction (db_{frac}) of the system is 0.5. 75

5.1 Initial configuration with one of the shapes (triangle) kept at a depth $h = 105d$ from the free surface. The base is made of particles of size $1d$(blue particles) at $y = 0$ while the top surface is free to move and periodic boundary conditions are applied in x direction.The intruder shapes that are considered in our study are disc $OS1$, square $OS2$, rectangle with its longer dimension along the y-axis $OS3$, rectangle with its longer dimension along the x-axis $OS4$, and equilateral triangle $OS5$. 83

5.2 The vertical displacement of the intruder (a) disc (b) square, (c) narrow-rectangle (d) wide-rectangle, and (e) triangle shapes as a function of simulation time(t) for an oscillation amplitude A/d= 3 and at different time-period($T/\sqrt{d/g}$). The settling level at the top and bottom of the graphs depicts the IO reaching the top and bottom surface of the medium. 85

5.3 A pictorial representation depicting the position of the narrow-rectangle $OS3$ for A/d=3 and $T/\sqrt{d/g}$ =7 at different simulation time $t/\sqrt{d/g}$: (a) 0 (b) 100 (c) 300 (d) 500 (e) 700 and (f) 1000. 86

5.4 A pictorial representation depicting the position of the narrow-rectangle $OS3$ for A/d=3 and $T/\sqrt{d/g}$ =1 at different simulation time $t/\sqrt{d/g}$: (a) 0 (b) 100 (c) 300 (d) 500 (e) 700 and (f) 1000. 87

5.5 The rise rate(V_y) of the horizontally oscillating intruder as a function of its time-period(T) for different amplitude A. Here, each plot corresponds to a different intruder shape: (a) disc, (b) square, (c) narrow-rectangle, (d) wide-rectangle, and (e) triangle 87

5.6 The rise rate (V_y) of the horizontally oscillating intruder as a function of its time-period (T) for different friction coeficient μ and amplitude $A/d = 3$. Here, each plot corresponds to a different intruder shape: (a) disc, (b) square, (c) narrow-rectangle, (d) wide-rectangle, and (e) triangle. 89

5.7 Oscillatory motion of the intruder as sine wave function representing the phase angle(ϕ) 91

5.8 The rise rate(Vy) of the intruder vs the phase angle at $A/d = 3$ and different $T/\sqrt{d/g}$ for (a)disc, (b)square, (c)narrow-rectangle, (d)wide-rectangle, and (e)triangle shaped intruder object. 93

5.9 The figure shows the drag experienced at various phase angle with varying T for (a)disc, (b)square, (c)narrow-rectangle, (d)wide-rectangle, and (e)triangle shaped intruder object 95

5.10 The time-averaged flow fields for depicting velocity V, pressure P, and area fraction Φ around the intruder $OS1$ (disc) for $T/\sqrt{d/g} = 1$ and different phase angle ϕ : (a), (f), (k) 0.0, (b) (g), (l) 5.0, and (c), (h), (m) 10.0, (d), (i), (n) 15.0 and (e), (j), (o) 19.0. The oscillating amplitude of the intruder is $A/d = 3$. . . . 97

5.11 The time-averaged flow fields for depicting velocity V, pressure P, and area fraction Φ around the intruder $OS3$ (rectangle with its longer dimension along the y-axis) for $T/\sqrt{d/g} = 1$ and different phase angle ϕ : (a), (f), (k) 0.0, (b) (g), (l) 5.0, and (c), (h), (m) 10.0, (d), (i), (n) 15.0 and (e), (j), (o) 19.0. The oscillating amplitude of the intruder is $A/d = 3$. 98

5.12 The time-averaged flow fields for depicting velocity V, pressure P, and area fraction Φ around the intruder $OS5$ (triangle) for $T/\sqrt{d/g} = 1$ and different phase angle ϕ : (a), (f), (k) 0.0, (b) (g), (l) 5.0, and (c), (h), (m) 10.0, (d), (i), (n) 15.0 and (e), (j), (o) 19.0. The oscillating amplitude of the intruder is $A/d = 3$. 99

5.13 A general shape ocillating horizontally with granular particles around it. . . 101

5.14 The shapes $OS1$, $OS2$ and $OS5$ with the points y and y^0 where the particles coving this distance of $(y - y^0)$ will fall beneath the base of the intruder. . . . 102

5.15 The height of the intruder object. 102

5.16 The colormap represents the rise rate V_y of the intruder(a) disc (b) square (c) narrow-rectangle and (d) wide-rectangle, and (e) triangle for all the oscillated T and A. 105

6.1 Initial configuration of our system with an intruder placed at a depth of $h = 300cm$ from the top wall. The granular mixture is comprised of dumbbells (black) and disc (grey) particles. At $y = \pm 300cm$, the system is confined by walls made of glued particles of size $1cm$ (orange), and periodic boundary conditions are applied in the x direction. The origin is located at the center of the intruder. In the right side of the figure the zoomed in region around the intruder is shown. 113

6.2 (a) Variation of drag force F_D with intruder velocity V_i for area fraction $\phi = 0.82$ on a log-log plot, (b) Variation of averaged particle contact N_c with V_i for $\phi = 0.82$, and (c) Variation of shear stress $|\tau_{xy}|$ with V_i for $\phi = 0.82$. . . 114

6.3 (a) Variation of drag force F_D with intruder spin ratio Ω for area fraction $\phi = 0.82$ on a log-log plot, (b) Variation of lift force F_L with Ω for $\phi = 0.82$ and (c) Variation of averaged particle contact N_C with Ω for $\phi = 0.82$. 116

6.4 The lift to drag force ratio F_L/F_D vs spin ratio ($\Omega = r_o R/V_i$) for different intruder velocities V_i (a)$1cm/s$, (b) $5cm/s$, (c) $25cm/s$ and, (d) $100cm/s$ and three different dumbbell fraction X_{db} of 0.0, 0.5 and 1.0, with system area fraction ϕ=0.82. 118

6.5 F_L/F_D as a function of friction coefficient μ for various ϕ. The more dilute the system is, the closer the value of F_L/F_D to the proposed model. 119

6.6 The drag force at a certain spin ratio $F_{D\Omega}$ normalized by the drag force at spin ratio of zero $F_{D\Omega=0}$ as a function of Ω for db_{frac} ranging from 0.0 to 1.0 for different intruder velocities U_i (a) $1cm/s$, (b) $25cm/s$, and (c) $100cm/s$. The $N_{C\Omega}/N_{C\Omega=0}$ as a function of Ω for various X_{db} and intruder velocities V_i (a) $1cm/s$, (b) $25cm/s$, and (c) $100cm/s$. The system has an area fraction ϕ of 0.82 and $\mu = 0.5$ 120

6.7 The lift to drag force ratio F_L/F_D vs spin ratio ($\Omega = r_o R/V_i$ for $V_i = 25cm/s$ and dumbbell fraction X_{db} 0.0 to 1.0 with system area fraction ϕ= (a)0.43, and (b) 0.82 in a semi-log plot. 121

6.8 The drag force at a certain spin ratio $F_{D\Omega}$ normalized by the drag force at spin ratio of zero $F_{D\Omega=0}$ as a function of Ω for db_{frac} ranging from 0.0 to 1.0 and ϕ = (a) 0.43 and (b) 0.82. The $N_{C\Omega}/N_{C\Omega=0}$ as a function of Ω for various X_{db} and ϕ = (c) 0.43 and (d) 0.82. 122

6.9 The mean (a) drag force F_D and (b) lift force F_L as a function of friction coefficient for $\phi = 0.43$ and 0.82, $V_i = 25cm/s$, $X_{db} = 0.5$ and $\Omega = 20$ 123

6.10 The distribution of drag force (a) $F_{D\Omega}/F_{D\Omega=0}$ and number of particle contact (b) $N_{C\Omega}/N_{C\Omega=0}$ as a function of its contact angle θ around the intruder surface for fraction of dumbbell $X_{db} = 0.0$ and $\phi = 0.82$. 123

6.11 The distribution of drag force (a) $F_{D\Omega}/F_{D\Omega=0}$ and number of particle contact (b) $N_{C\Omega}/N_{C\Omega=0}$ as a function of its contact angle θ around the intruder surface for fraction of dumbbell $X_{db} = 1.0$ and $\phi = 0.82$. 124

6.12 The distribution of tangential force $F_{t\theta}$ as a function of its contact angle θ around the intruder surface for fraction of dumbbell $X_{db} = 1$ and $\phi = 0.82$. . . 124
6.13 The time-averaged flow fields for depicting pressure P, shear stress $|\sigma_{xy}|$ and area fraction ϕ infront of the intruder for different spin ratio (Ω): (a), (d), (g) 0.0, (b) (e), (h) 1.0 and (c), (f), (i) 10.0. The velocity of the intruder is $V_i = 25cm/s$ and the fraction of dumbbell (X_{db}) in the system is 0.0. 125
6.14 The time-averaged flow fields for depicting pressure P, shear stress $|\sigma_{xy}|$ and area fraction ϕ infront of the intruder for different spin ratio (Ω): (a), (d), (g) 0.0, (b) (e), (h) 1.0 and (c), (f), (i) 10.0. The velocity of the intruder is $V_i = 25cm/s$ and the fraction of dumbbell (X_{db}) in the system is 0.5. 127
6.15 The time-averaged flow fields for depicting pressure P, shear stress $|\sigma_{xy}|$ and area fraction ϕ infront of the intruder for different spin ratio (Ω): (a), (d), (g) 0.0, (b) (e), (h) 1.0 and (c), (f), (i) 10.0. The velocity of the intruder is $V_i = 25cm/s$ and the fraction of dumbbell (X_{db}) in the system is 1.0. 129

LIST OF TABLES

3.1 Comparison of ϕ obtained from numerical simulations and the theoretical estimate, l_{cs}/S. 34
3.2 The values of fits and constants 36

5.1 The parameters and its values used in our numerical simulations 84
5.2 Comparison between value of T_{rising} from theoretical estimate and the numerical simulations. 104
5.3 Table showing the theoretical value of A_{min} for all the intruder shapes. 105

6.1 The parameters and its values used in our numerical simulations 114

CHAPTER 1

INTRODUCTION

1.1 Granular materials

Granular matter is a collection of discrete macroscopic particles that exists around us in multiple forms, such as sand in the deserts or as grains in food industries. Granular materials are being handled at several places such as the pharmaceutical industry, agriculture, and energy production. Although granular matter looks simple from the outset, they exhibit complex behaviour resulting from the inelastic particle collisions and the associated frictional effects. For instance, the system as a whole exhibit properties reminiscent to either fluids or solids depending on the forces it is subjected to. Due to its complex physical mechanism and engineering applications, granular matter has garnered interest among the researchers and the engineers alike. Moreover, granular physics can be applied to any kind of system which involves the movement of discrete particles that are primarily governed by contact forces and body forces. These could be the reasons for an increase in the interest in this field in the recent decades. Some of the important topics of interest for researchers are force chains [1], pattern formation [2], segregation [3, 4], robotic locomotion [5], meteor impacts [6], silo clogging [7], etc.

In a granular medium, the stress is transmitted from one particle to the other through a network of contacts commonly termed as force chains [8]. When granular particles are in motion, they may exhibit pattern formation like that of sand dunes [9]. A mixture

of different sized or different shaped particles subjected to external perturbations may often lead to segregation. Granular systems are known to jam and go through a jamming transition [10]. Moreover, the velocity fluctuations, the volume fraction, and the shear stress regulate the transition from a fluid-like to a solid-like behaviour of the granular system as a whole. The universal gripper has recently been developed using the jamming behaviour of granular material [11] which can hold any arbitrary shaped object. The motion of sand-dwelling creatures has been understood using the concepts of granular physics [5, 12]. It is important to understand this kind of motion as it can help in designing vehicles or robots that can travel through sand or snow.

1.2 Locomotion in a granular medium

Understanding the intruder's movement within the sand has been quite challenging to the researchers owing to the complex nature of granular particulate system. Earlier studies on the locomotion within a granular material were inspired by the movements of certain animals and reptiles in nature such as Scincus Scincus (commonly known as sandfish skink) [12], Crotalus cerastes (desert snake) [13], etc. Maladen *et al* [5] observed that the sand-lizard does not use its limbs but it uses undulatory motion of its body for propulsion while it is under the surface. Researchers tried to comprehend this phenomenon by modeling the movement of these creatures as a self-energized objects [14, 15]. Further studies were carried out to comprehend the process underlying the movement of a self-energized object oscillating horizontally in both two-dimensional [14] and three-dimensional systems [15]. Huang *et al.* [14] have used a cavity model to describe the process underlying the rise and sink of an intruder in a two-dimensional system. The authors reported that the amplitude and the frequency with which the intruder oscillates are the most important factors in determining whether it rises or sinks in a granular medium. They also observed a minimal oscillation amplitude (A_{min}) below which the intruder never sink, regardless of the frequency of the oscillating intruder object. The two forces which significantly influence the movement of an intruder through the granular medium are the drag and lift forces.

1.3 Drag in a granular medium

Drag force is the resistive force acting on the intruder in the direction opposite to its motion. In a granular medium, the drag force arises due to the interactions between the intruder and the particles around it. There are many works [16–21] dedicated to characterize the drag on an intruder. These studies includes an intruder moved horizontally or vertically within the granular media either at a low [16] or high velocities [18]. In a high velocity regime, the drag force increases monotonically with the intruder's velocity [18]. Whereas in a low velocity regime, it is independent of the intruder's velocity for a frictional system [16]. The resistive force or drag force not only depends on the velocity of the intruder but also its direction of motion: Liu *et al.* [22] noticed a maximum drag force when the intruder is moved vertically downward in a gravity system while a minimum drag force when dragged upward. Albert *et al.* [17] stated that the drag force is almost independent of the shape of the intruder in a low-velocity regime. Whereas in a high-velocity regime, drag is found to be dependent on the shape of the intruder. The authors further stated that an increase in the intruder's flatness increases the drag due to an increase in the number of inter-particle and particle-intruder collisions. The drag force depends on not only the properties of the intruder but also the external forces. For example, the drag is noticed [20, 23] to be higher in a confined system than the one with a free surface due to the presence of the confining pressure. Moreover, the nature of contact forces between the interacting granules in the dense granular medium under high pressure can also impact the granular flow behavior [24]. In addition, the drag increases with an increase in the gravitational acceleration [25]. On the other hand, in a system without gravity, the drag was observed to increase with the square of the intruder's velocity [26]. As it may be expected, the drag depends on the properties of the granular media surrounding it. Zhou *et al.* [20] reported a higher drag on an intruder traversing a polydispersed granular media than a monodispersed one owing to their packing effects. The drag also depends on the shape of the granular particles. Zhou *et al.* [23] noticed a higher drag force on an intruder moving through a system of dumbbell-shaped granules than that of elliptical granules. The horizontal movement of the intruder in granular media is influenced by the drag force whereas, the vertical movement is affected by the lift force.

1.4 Lift in a granular medium

Lift force is the force experienced by the intruder in a direction perpendicular to its motion. Despite its importance, there have been very few studies devoted to understanding this phenomenon [27–29] in granular systems as compared to that in fluids. Soller and Kohler [30] found that the lift force on rotating vanes increases with an increase in the size of the granular particles. They also stated that with the increase of the immersion depth of the vanes, the vertical lift force increases supralinearly. Ding *et al.* [27] stated that a symmetric object, such as a cylinder, when dragged within a granular medium, experiences a weak lift force that varies linearly with the depth. They have reported that the lift force has a dependence on the depth of the intruder within the granular medium. Maladen *et al.* [31] in their study of a sand swimming robot that mimics the movement of sand lizard within the granular media, found that the lift force can be controlled by varying the head shape of the robot. They have varied the angle of the upper leading surface of the wedge, α, due to which a variation in lift force occurs. The extent of lift forces is larger for $\alpha < 90^{\circ}$, due to the inclined surface that pushes the particles around it downwards where the yield stress is the maximum than other positions in the system. Therefore an increase in yield stress in the media makes the flow asymmetric, leading the particles around the intruder to rise, providing it a positive lift force. They also found that the robot with a symmetric head shape experiences an upward lift in a granular medium, whereas, in fluid, a translating symmetric body does not experience any lift force. Potiguar [28] reported that in a dilute granular flow, there was no net lift force on a circular obstacle, while the net lift force on an asymmetric obstacle depends non-monotonically on the intruder velocity and depth. Guillard *et al.* [32] found that a cylindrical intruder moving within the granular media experiences strong lift force, but at depths greater than its diameter, there is a saturation in lift force. Potiguar and Ding [29] found that the lift force is a non-monotonic function of the intruder's velocity and depth in an inertial-regime.

The existing literature on the intruder dynamics within granular medium is confined mostly to the spherical intruders traversing a system of spherical particles. However, the granular particles existing in nature and those used in the industries are mostly non-spherical in shape. Moreover, the effect of the intruder's shape on its locomotion properties is hardly explored. In addition, a coupled effect of different types of intruder motion on its surroundings has scarcely been studied to the best of our knowledge.

1.5 Objectives

The objectives of this thesis are as follows:

- Role of shape on the forces on an intruder moving through dense granular medium
- Drag on a circular intruder traversing a shape heterogeneous granular mixture
- Shape dependence on the rise and sink of a wiggling intruder in granular medium
- Role of constituents of a granular medium on the lift force experienced by a translating and rotating intruder

The thesis is organized as follows:

Chapter 2: Simulation technique with algorithm is explained.

Chapter 3: Here, we studied the effect of an intruder's shape and orientation has on the drag and lift force it experiences during its movement within the granular medium. The force distribution on the intruder surface with the surrounding particles has been analysed.

Chapter 4: In this chapter, we reported the effect of the fraction of dumbbells on the drag characterstic of an intruder moving through a heterogeneous mixture of dumbbell and disc in a gravityless system. We further studied different system parameters like the area fraction ϕ, coefficient of friction μ and their effect on the intruder dynamics. The mean flow field are presented to understand the stress characterstic for different fractions of dumbbell.

Chapter 5: In this chapter, we presented the role of an intruder's shape and orientation on its vertical dynamics when oscillated horizontally within the dense granular medium. We studied the rate of vertical displacement as a function of the intruder's amplitude (A) and timeperiod (T). The rise and sink of an intruder as a function of phase angle is analysed.

Chapter 6: A rotating and translating object in a fluid due to the pressure difference can deviate from its straight path, this phenomena is known as Magnus effect. In this chapter, we analyse the lift force on a translating and rotating intruder in a mixture of dumbbell and disc for various spin ratios.

Chapter 7: Conclusion and suggestions for future work.

BIBLIOGRAPHY

[1] Colin Thornton. Force transmission in granular media. *Kona Powder and Particle Journal*, 15:81–90, 1997.

[2] E Lemaire, Y Ould Mohamed Abdelhaye, J Larue, R Benoit, P Levitz, and H Van Damme. Pattern formation in noncohesive and cohesive granular media. In *Fractals in Natural Sciences*, pages 563–571. World Scientific, 1994.

[3] Hans J Herrmann, J-P Hovi, and Stefan Luding. *Physics of dry granular media*, volume 350. Springer Science & Business Media, 2013.

[4] N Thomas. Reverse and intermediate segregation of large beads in dry granular media. *Physical Review E*, 62(1):961, 2000.

[5] Ryan D Maladen, Yang Ding, Paul B Umbanhowar, and Daniel I Goldman. Undulatory swimming in sand: experimental and simulation studies of a robotic sandfish. *The International Journal of Robotics Research*, 30(7):793–805, 2011.

[6] Amanda M Walsh, Kristi E Holloway, Piotr Habdas, and John R de Bruyn. Morphology and scaling of impact craters in granular media. *Physical review letters*, 91(10):104301, 2003.

[7] A. Vamsi Krishna Reddy, Sonu Kumar, K. Anki Reddy, and Julian Talbot. Granular silo flow of inelastic dumbbells: Clogging and its reduction. *Phys. Rev. E*, 98:022904, Aug 2018.

[8] Qicheng Sun and Guangqian Wang. *Mechanics of granular matter*. WIT Press, 2013.

[9] Hans-J Herrmann. Pattern formation of dunes. *Nonlinear Dynamics*, 44(1):315–317, 2006.

[10] Haye Hinrichsen and Dietrich E Wolf. *The physics of granular media*. John Wiley & Sons, 2006.

[11] John R Amend, Eric Brown, Nicholas Rodenberg, Heinrich M Jaeger, and Hod Lipson. A positive pressure universal gripper based on the jamming of granular material. *IEEE transactions on robotics*, 28(2):341–350, 2012.

[12] Edwin Nicholas Arnold. Identifying the effects of history on adaptation: origins of different sand-diving techniques in lizards. *Journal of Zoology*, 235(3):351–388, 1995.

[13] Hamidreza Marvi, Chaohui Gong, Nick Gravish, Henry Astley, Matthew Travers, Ross L Hatton, Joseph R Mendelson, Howie Choset, David L Hu, and Daniel I Goldman. Sidewinding with minimal slip: Snake and robot ascent of sandy slopes. *Science*, 346(6206):224–229, 2014.

[14] Ling Huang, Xianwen Ran, and Raphael Blumenfeld. Vertical dynamics of a horizontally oscillating active object in a two-dimensional granular medium. *Phys. Rev. E*, 94:062906, Dec 2016.

[15] Liu Ping, Xianwen Ran, and Raphael Blumenfeld. Sink-rise dynamics of horizontally oscillating active matter in granular media: Theory. *arXiv preprint arXiv:2006.04160*, 2020.

[16] R. Albert, M. A. Pfeifer, A.-L. Barabási, and P. Schiffer. Slow drag in a granular medium. *Phys. Rev.*

Lett., 82:205–208, Jan 1999.

[17] I. Albert, J. G. Sample, A. J. Morss, S. Rajagopalan, A.-L. Barabási, and P. Schiffer. Granular drag on a discrete object: Shape effects on jamming. *Phys. Rev. E*, 64:061303, Nov 2001.

[18] Fabricio Q. Potiguar and Yang Ding. Lift and drag in intruders moving through hydrostatic granular media at high speeds. *Phys. Rev. E*, 88:012204, Jul 2013.

[19] A Seguin and P Gondret. Drag force in a cold or hot granular medium. *Physical Review E*, 96(3):032905, 2017.

[20] Fuping Zhou, Suresh G Advani, and Eric D Wetzel. Slow drag in polydisperse granular mixtures under high pressure. *Physical Review E*, 71(6):061304, 2005.

[21] CR Wassgren, JA Cordova, R Zenit, and A Karion. Dilute granular flow around an immersed cylinder. *Physics of fluids*, 15(11):3318–3330, 2003.

[22] Chuanping Liu, Hongmei Wan, and Li Wang. Effect of movement direction on resistance force in granular media. *Powder Technology*, 344:545–550, 2019.

[23] Fuping Zhou, Suresh G Advani, and Eric D Wetzel. Simulation of the slow drag of a cylinder through a confined pressurized bed of dumbbell and elliptically cylindrical granules using the discrete element method. *Computer Modeling in Engineering and Sciences (CMES)*, 39(1):49, 2009.

[24] F Zhou, SG Advani, and ED Wetzel. Characterization of the viscous behavior of compacted ceramic particles under shear and pressure loads. *International Journal of Applied Mechanics and Engineering*, 10(3):505–514, 2005.

[25] D. J. Costantino, J. Bartell, K. Scheidler, and P. Schiffer. Low-velocity granular drag in reduced gravity. *Phys. Rev. E*, 83:011305, Jan 2011.

[26] A. Seguin, A. Lefebvre-Lepot, S. Faure, and P. Gondret. Clustering and flow around a sphere moving into a grain cloud. *The European Physical Journal E*, 39(6):63, Jun 2016.

[27] Yang Ding, Nick Gravish, and Daniel I. Goldman. Drag induced lift in granular media. *Phys. Rev. Lett.*, 106:028001, Jan 2011.

[28] Fabricio Q Potiguar. Lift force on an asymmetrical obstacle immersed in a dilute granular flow. *Physical Review E*, 84(6):061302, 2011.

[29] Fabricio Q. Potiguar and Yang Ding. Lift and drag in intruders moving through hydrostatic granular media at high speeds. *Phys. Rev. E*, 88:012204, Jul 2013.

[30] Raenell Soller and Stephan A Koehler. Drag and lift on rotating vanes in granular beds. *Physical Review E*, 74(2):021305, 2006.

[31] Ryan D Maladen, Paul B Umbanhowar, Yang Ding, Andrew Masse, and Daniel I Goldman. Granular lift forces predict vertical motion of a sand-swimming robot. In *2011 IEEE International Conference on Robotics and Automation*, pages 1398–1403. IEEE, 2011.

[32] François Guillard, Yoël Forterre, and Olivier Pouliquen. Lift forces in granular media. 26, 03 2014.

CHAPTER 2

SIMULATION METHOD

We used the discrete element method (DEM) for all of our studies. Using DEM technique, we can access various particle attributes such as their positions, velocities, forces, torques etc at different times of the simulation. This aids us in understanding the particle level dynamics. The first step in the DEM technique is the detection of contacts. Two particles i and j having radii of r_i and r_j are said to be in contact, if the overlap between them is $\delta \geq 0$. Here, $\delta = r_i + r_j - |r_{ij}|$, where r_{ij} is the distance between the centres of two particles i and j. Once the particle contacts are determined, we compute the contact forces for each of the particles. The normal and tangential components of contact force F_{ij}^n and F_{ij}^n[1] of a particle i due to its contacting particle j are computed as:

$$F_{ij}^n = \sqrt{(R_{\text{eff}}\delta_{ij})}(K_n\delta_{ij}\hat{\boldsymbol{r}}_{\boldsymbol{ij}} - m_{\text{eff}}\gamma_n v_{ij}^n) \tag{2.1}$$

$$F_{ij}^t = -min(\mu F_n, \sqrt{(R_{\text{eff}}\delta_{ij})}(K_t\boldsymbol{\Delta s_{ij}} + m_{\text{eff}}\gamma_t v_{ij}^t) \tag{2.2}$$

Then, the positions and velocities of the particles are updated at regular intervals of time by integrating the equations of motion.

$$\frac{d(m_i u_i)}{dt} = F_g + \sum_{j=1}^{N} F_{c_j} \tag{2.3}$$

We also integrated the angular momentum equation at regular interval of time to update the angular velocity of the particles.

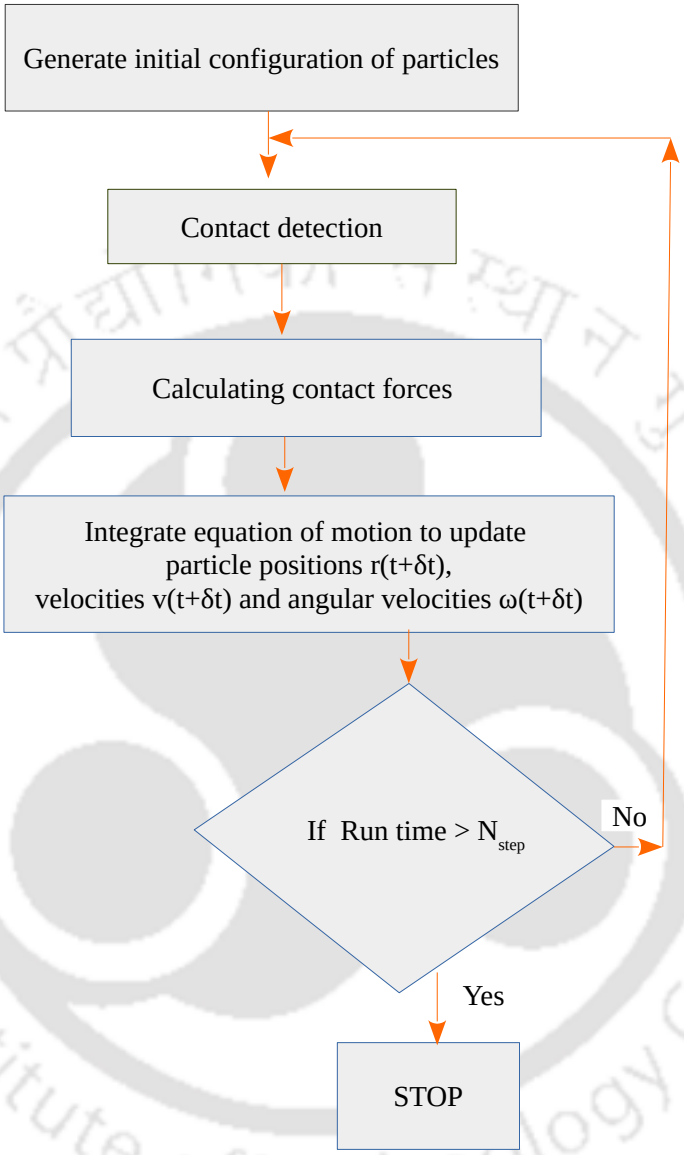

Figure 2.1: The flowchart depicting the flow of operations in a DEM technique. Here 'N_{step}' corresponds to the total number of simulation timesteps, which vary depending on the problem of interest.

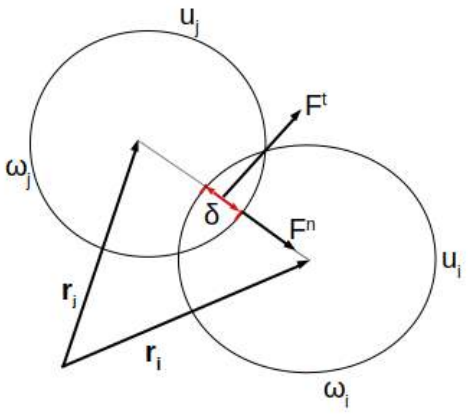

Figure 2.2: Two spherical particles i and j are in contact, with $\boldsymbol{r_i}$, $\boldsymbol{r_j}$ the positon vector, u_i u_j the velocity vector, and ω_i,ω_j the rotational velocity vector. F^n, and F^t are the normal and tangential components of contact forces and δ is the overlap between the two particles i and j.

$$I_i\omega_i = \sum \tau_i \tag{2.4}$$

The forces considered on the particles are the contact forces F_c and the gravity forces F_g. Fig 2.1 depicts the sequence of a DEM method.

The superscript n,t denotes the normal and tangential components of the corresponding parameters, whereas the subscript i, j denotes the i^{th},$and j^{th}$ particles. The effective radius is defined as $R_{\text{eff}} = \frac{r_i r_j}{r_i + r_j}$, where r_i and r_j are the particle radii. K is the elastic constant, $\boldsymbol{\hat{r}_{ij}}$ is the unit vector in the direction of line joining the particles i and j and $m_{\text{eff}} = \frac{m_i m_j}{m_i + m_j}$ is the effective mass where m is mass. γ is the damping coefficient, μ is the coefficient of friction, $\boldsymbol{\Delta s_{ij}}$ is the tangential displacement vector and v_{ij}^t is the tangential component of the relative velocity. In our work, the dumbbells are created by fusing two discs of same size without any overlap. The positions and velocities of a dumbbell are computed as the centre of mass and centre of mass velocities of the two constituting parts of the dumbbell. The total force acting on a dumbbell is determined by adding the force experienced by the two constituent discs of it. The total torque experienced by a dumbbell is determined in the same way as that of the force. The forces or torques experienced by one constituent particle of a dumbbell due to another particle of the same dumbbell are set to zero. All of our simulations are performed using LAMMPS package [2] and they are visualized using OVITO [3] package.

Due to the advent of supercomputer and vast increase in the computational resources, the use of DEM technique has increased in variuos problems including industrial one's

as well. The DEM technique has been proved useful in determining the dynamics of granular particles in various enviroments such as problems involving an intruder moving through granular media [4, 5], particles flowing over an inclined plane ([6, 7], particle flow through a hopper [8], contact networks in granular media [9]. This numerical technique has also been applied to determining jamming probability in confined granular systems [10–12], probing segregation dynamics [13, 14], analysing mixing properties [15, 16], understanding of force chain networks[17, 18], and studying particle motion in rotating cylinders[19, 20].

BIBLIOGRAPHY

[1] Nikolai V. Brilliantov, Frank Spahn, Jan-Martin Hertzsch, and Thorsten Pöschel. Model for collisions in granular gases. *Phys. Rev. E*, 53:5382–5392, May 1996.

[2] Steve Plimpton. Fast parallel algorithms for short-range molecular dynamics. *Journal of Computational Physics*, 117(1):1 – 19, 1995.

[3] Alexander Stukowski. Visualization and analysis of atomistic simulation data with ovito–the open visualization tool. *Model. Simul. Mater. Sci. Eng*, 18(1):015012, 2010.

[4] Manish Dhiman, Sonu Kumar, K. Anki Reddy, and Raghvendra Gupta. Origin of the long-ranged attraction or repulsion between intruders in a confined granular medium. *Journal of Fluid Mechanics*, 886:A23, 2020.

[5] Sonu Kumar, Manish Dhiman, and K. Anki Reddy. Magnus effect in granular media. *Phys. Rev. E*, 99:012902, Jan 2019.

[6] Stanislav Parez, Einat Aharonov, and Renaud Toussaint. Unsteady granular flows down an inclined plane. *Phys. Rev. E*, 93:042902, Apr 2016.

[7] Anurag Tripathi and D. V. Khakhar. Rheology of binary granular mixtures in the dense flow regime. *Physics of Fluids*, 23(11):113302, 2011.

[8] Amlan Datta, B. K. Mishra, S. P. Das, and A. Sahu. A dem analysis of flow characteristics of noncohesive particles in hopper. *Materials and Manufacturing Processes*, 23(2):195–202, 2008.

[9] A. Sufian, A. R. Russell, and A. J. Whittle. Anisotropy of contact networks in granular media and its influence on mobilised internal friction. *Géotechnique*, 67(12):1067–1080, 2017.

[10] Su-San Park and Eung Soo Kim. Jamming probability of granular flow in 3d hopper with shallow columns: Dem simulations. *Granular Matter*, 22(4):77, Sep 2020.

[11] Ya Zhao, Ray A. Cocco, Shiliang Yang, and Jia Wei Chew. Dem study on the effect of particle-size distribution on jamming in a 3d conical hopper. *AIChE Journal*, 65(2):512–519, 2019.

[12] Michel Tsukahara, Lionel Pournin, and Thomas M. Liebling. Simple probabilistic modeling of granular jamming and validation using dem. *AIP Conference Proceedings*, 1145(1):507–510, 2009.

[13] Shiliang Yang, Liangqi Zhang, Kun Luo, and Jia Wei Chew. Dem study of the size-induced segregation dynamics of a ternary-size granular mixture in the rolling-regime rotating drum. *Physics of Fluids*, 29(12):123301, 2017.

[14] Ahmed Jarray, Hao Shi, Bert J. Scheper, Mehdi Habibi, and Stefan Luding. Cohesion-driven mixing and segregation of dry granular media. *Scientific Reports*, 9(1):13480, Sep 2019.

[15] F. Bertrand, L.-A. Leclaire, and G. Levecque. Dem-based models for the mixing of granular materials. *Chemical Engineering Science*, 60(8):2517 – 2531, 2005. 5th International Symposium on Mixing in

Industrial Processes (ISMIP5).

[16] Steffen Schmelzle and Herrmann Nirschl. Dem simulations: mixing of dry and wet granular material with different contact angles. *Granular Matter*, 20(2):19, Feb 2018.

[17] Wei Wang, Wei Gu, and Kun Liu. Force chain evolution and force characteristics of shearing granular media in taylor-couette geometry by dem. *Tribology Transactions*, 58(2):197–206, 2015.

[18] Lingran Zhang, Nho Gia Hien Nguyen, Stéphane Lambert, François Nicot, Florent Prunier, and Irini Djeran-Maigre. The role of force chains in granular materials: from statics to dynamics. *European Journal of Environmental and Civil Engineering*, 21(7-8):874–895, 2017.

[19] J. R. Third, D. M. Scott, S. A. Scott, and C. R. Müller. Tangential velocity profiles of granular material within horizontal rotating cylinders modelled using the dem. *Granular Matter*, 12(6):587–595, Dec 2010.

[20] S.S. Shirsath, J.T. Padding, H.J.H. Clercx, and J.A.M. Kuipers. Dynamics of granular flows down rotating semi-cylindrical chutes. *Procedia Engineering*, 102:731 – 740, 2015. New Paradigm of Particle Science and Technology Proceedings of The 7th World Congress on Particle Technology.

CHAPTER 3

ROLE OF SHAPE ON THE FORCES ON AN INTRUDER MOVING THROUGH A DENSE GRANULAR MEDIUM[1]

3.1 Introduction

Granular matter is a collection of discrete macroscopic particles that exhibit properties of solids or fluids depending on the volume fraction [1]. It is present everywhere around us in multiple forms such as sand in the deserts or as grains in food industries. Dry granular matter exhibits properties that resemble those of Newtonian fluids such as capillary action [2], Magnus effect [3], Kevin-Helmholtz [4] and Rayleigh-Taylor [5] instabilities. In addition, understanding the forces on objects moving in fluids has been an active area of research for the last few decades, as it has applications in the development of vehicles in the automobile [6] and aerospace industries [7], etc. Though drag and lift forces are well understood in fluids, they have been less investigated in granular media.

Drag is the retarding force exerted on a body by surrounding medium. Studies performed for various configurations [8–10] in granular media to understand the drag include an intruder object moving horizontally or vertically at low [8] or high velocities [11]. In the slow velocity regime, the drag force is either independent of, or weakly

[1]The article based upon the work reported in this chapter is published in *Partcl. Scn and Tech. 2021* ; title: Role of shape on the forces on an intruder moving through a dense granular medium; authors: Bitang K Tripura, S Kumar, Julian Talbot and KA Reddy.

dependent on, the intruder's velocity [8]. At higher velocity the drag force increases monotonically with the intruder velocity. Albert *et al* [9] studied objects of different shapes and found that the difference in drag for any pair was less than twenty percent in the low-velocity regime. This work, however, did not explore the behavior at higher velocities. In a recent study of intruders of various shapes in a slow granular silo flow it was observed that the dimensionless number characterizing the drag force varied significantly with shape [12].

In addition to drag, objects may also experience a lift force while moving in a granular medium. However, there have been very few studies devoted to understand this phenomenon [10, 13–15]. Ding *et al* [10] stated that a symmetric object, such as a cylinder, when dragged within a granular medium experiences a weak lift force that varies linearly with the depth. Potiguar [13] reported that in a dilute granular flow there was no net lift force on a circular obstacle, while the net lift force on an asymmetric obstacle depends non-monotonically on the intruder velocity and depth. Guillard *et al* [14] studied the lift force on a cylinder moving horizontally in a granular medium under gravity. They observed that the lift force saturates at depths greater than the cylinder diameter and noted that the gravitational pressure gradient breaks the up/down symmetry of the moving intruder thereby modifying the flow around its surface. Debnath *et al* [15] observed that the lift force for a disc-shaped intruder rises with the immersion depth and reaches a constant value at larger depths. It was argued that the lift is the result of the asymmetry in the dilation and shear rate in the regions above and below the intruder.

The studies mentioned above are relevant for understanding animal locomotion in granular media. Subsurface motion is essential for sand dwelling animals to shelter from high temperatures in deserts during day time or to escape from predators. Animals such as sand lizards propel themselves using undulatory movements [16, 17]. Hence, it is crucial to address the effect of shape on drag, and the induced lift, as the shape of the object determines the strength of the jammed region built in front of the intruder [9].

The objective of the present work is to understand the shape and friction dependence of the drag and lift forces on an intruder immersed in a granular medium as a function of its velocity and depth. We provide details about the simulation method in section 3.2, results and discussion in section 3.3, followed by our conclusions in section 3.4.

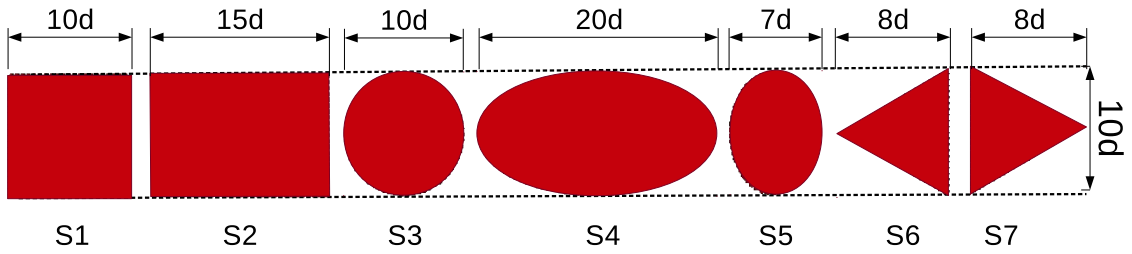

Figure 3.1: The various shapes considered in our study. In the simulations they move from left to right.

3.2 Simulation Methodology

In this work, we employed the Discrete Element Method (DEM) [18] to study the forces on variously-shaped objects being dragged through a granular medium in the presence of gravity. The simulations were performed in two dimensions with periodic boundary conditions in the x-direction. A gravitational field of magnitude g acts along the negative y direction and a wall, composed of particles of diameter d, confines the simulation system along $y = 0$. The density (mass per unit area) is taken as ρ. In our simulations we used non-dimensionalised quantities with g, d, and ρ as the basic units. The intruder position is fixed and then some 63000 particles are radomly poured in the system from above. The diameter of the particles range uniformly from 0.9d to 1.1d to avoid crystalization. The particles are allowed to settle under the influence of gravitational and dissipative forces (discussed later) until the energy of the system reaches a minimum. The simulation system spans $300d$ along the x direction while a free surface is present at a height of about $195d$ measured from the bottom. The depth of the center of mass of the intruder from the free surface is denoted by h(see Fig. 3.2).

The intruder is displaced at a constant velocity v along the positive x-direction for a total distance of $1200d$. We considered 7 different shapes in our study: a square (S1), a rectangle (S2), a disk (S3), an ellipse with major axis aligned with the direction of motion of the intruder (S4), an ellipse with minor axis aligned with the x- direction (S5), an equilateral triangle with edge pointing opposite to the moving direction (S6) and an equilateral triangle with edge pointing along the moving direction (S7): See Fig. 5.14. The maximum cross-section of all shapes has the same length of $10d$. Fig. 3.2 shows an initial configuration for S6 at a depth of $h = 105d$. Each of these shapes is created

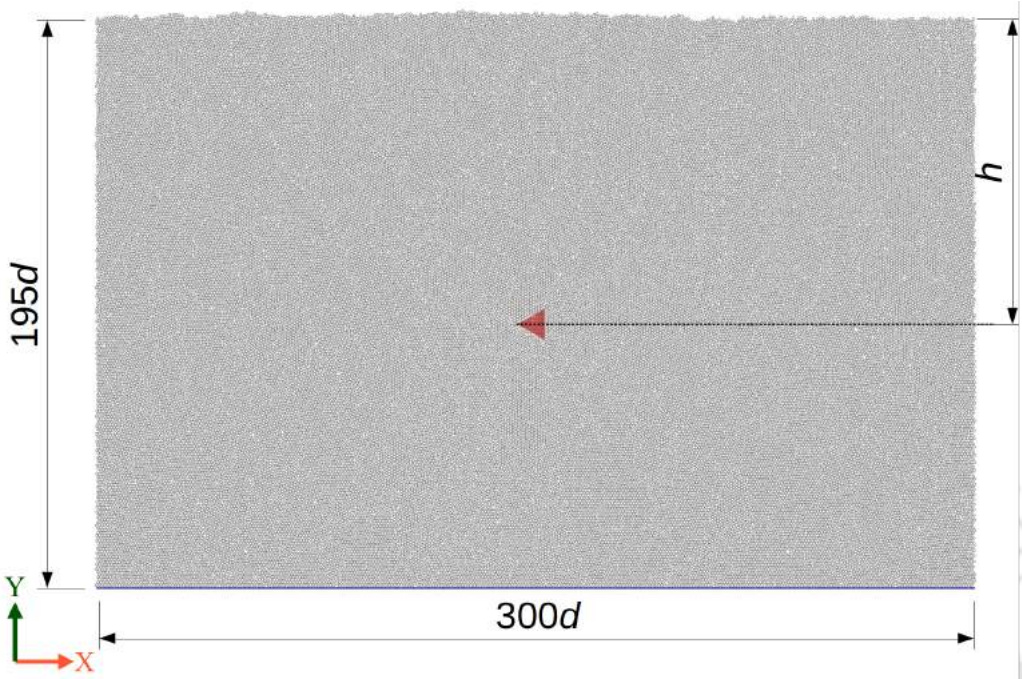

Figure 3.2: Initial configuration for one of the shapes (backward triangle, S6) at a depth $h = 105d$. Periodic boundary conditions are applied in the x-direction. The system is confined by a wall at $y = 0$ composed of particles of size $1d$ (blue particles), while the top surface is unconstrained. The origin is located at the left bottom corner.

from a set of particles, for example the square shape (S1) is made by arranging twenty layers of particles, with each layer consisting 20 particles, each particle with a diameter of 0.5d, and a total of 400 particles are used. The rectangle shape (S2) is created by arranging twenty layers of particles, with each layer having thirty particles having a total of 600 particles. The disc shape (S3) is created by placing seven consecutive layers of particles in a circular form having 339 particles in total. Similarly, the elliptical shape (S4 and S5) is created by placing the particles on the circumference of the ellipse, and then consecutive layers of particles are placed to make the desired shape. The S4 shape (ellipse-x-major) is created using 595 particles, while for the S5 shape (ellipse-y-major), 224 particles are used. Lastly, the equilateral triangles (S6 and S7) are created out of 231 particles. The particles that are used for creating the shapes have a diameter of 0.5d each. The intruder object as a whole is considered a single entity and its momentum is governed by rigid body dynamics. At each timestep the total force (torque) on the rigid intruder is computed as the sum of the forces (torques) on its constituent particles. We

have maintained the same cross-section facing the flow direction and also we maintained the same mass for each intruder even though we used a different number of particles to construct the intruder.

The DEM technique is discussed elaborately in chapter 2. The values of variuos constant used in the simulations are given as $k_n = 2 \times 10^6 \rho dg$ an $k_t = 2.54 \times 10^6 \rho dg$. The normal and tangential damping coefficients, γ_n and γ_t, were taken as $\gamma_n = \gamma_t = 3200\sqrt{g/d^3}$. The forces on the intruder are recorded at time intervals of $5 \times 10^{-4}\sqrt{d/g}$. The length of the simulation corresponds to the time that it takes for an intruder to travel $1200d$ for a specific velocity. All the simulations were performed with LAMMPS [22] (https://lammps.sandia.gov/index.html) and OVITO [23] was used for post-simulation visualisation.

3.3 Results and Discussion

In this section, we present the results for all seven intruder shapes (see Fig. 5.14). The intruder moves at a constant velocity v along the positive x direction at depth h. The study was carried out for various velocities v, depths h, and coefficients of friction μ. Subsection 3.3.1 presents the drag on the intruder for various velocities v and coefficient of friction μ at a constant depth $h = 105d$. Subsection 3.3.2 addresses the particle contacts on the intruder for various v and μ at a constant depth $h = 105d$ and kinetic drag regimes. Subsection 3.3.3 provides the details on the lift force experienced by the intruder for various v and μ at a constant depth $h = 105d$. Subsection 3.3.4 explores the depth dependence of forces on the intruder for velocities $v/\sqrt{dg} = 1$, 5, and $\mu = 0.1$. Lastly, Subsection 3.3.5 examines the distribution of forces around the intruder for various velocities v at a fixed h and μ. Reported quantities such as drag F_D, lift F_L, and number of contacts N_c have been calculated by averaging over several configurations after the intruder achieves a mean steady state behavior, *i.e.*, the instantaneous drag fluctuates around a well defined mean.

3.3.1 Drag on the moving intruder

In this subsection, we present and discuss the drag on the moving intruder at several velocities v and coefficients of friction μ. The drag F_D against velocity v (log-log plot)

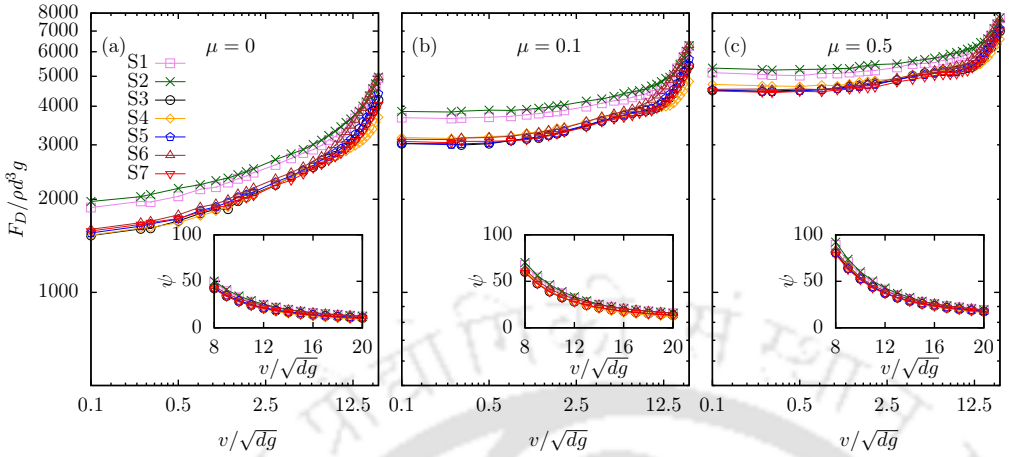

Figure 3.3: The variation of drag on an intruder with the velocity at (a) $\mu = 0$, (b) $\mu = 0.1$, and (c) $\mu = 0.5$ for all the shapes in our study on a log-log scale. The inset figures show $\psi = F_D/v^2$ for higher velocities.

for $\mu = 0$, 0.1 and 0.5 is shown in Fig. 4.2 (a), (b) and (c), respectively, for all the shapes. Additionally, $\psi = F_D/v^2$ is shown in the insets of each figure.

A minimum force, known as the yield drag [24–26], is required to initiate the motion of an object in granular media. Therefore, we can write the drag as $F_D = F_Y + F_K$ where F_Y is the yield drag necessary to initiate the motion, while F_K is the kinetic drag. Assuming that the drag for the lowest velocity at which we performed our simulations gives us the yield drag, F_Y is highest for S2 followed by S1 for all μ. The other shapes have nearly identical yield drag (within seven percent of each other) for all values of μ considered.

It is known from a few published studies [24–28] that the drag regimes and drag laws in granular media are strongly correlated with the intruder's velocity. In the present work we observe that, without friction, the drag increases gradually with v (see Fig. 4.2 (a)). However, in the presence of friction, specifically, $\mu = 0.1$ and 0.5, we observe a constant drag regime at low velocities (see Fig. 4.2 (a) and (b)). Hilton and Tordesillas, [25] and Sonu *et al* [26] studied these drag regimes in the context of a dimensionless Froude number Fr which is the ratio of two timescales associated with the falling of grains in the wake and the forward motion of the intruder (assuming the intruder dimensions are much larger than the grains). They suggested that the constant drag regime exists for $Fr < 1$. Applying their individual definitions of Fr to our shape S3, Ref. [25] predicts that the constant drag regime should persist until $v/\sqrt{dg} \approx 1.12$, while Ref. [26] predicts

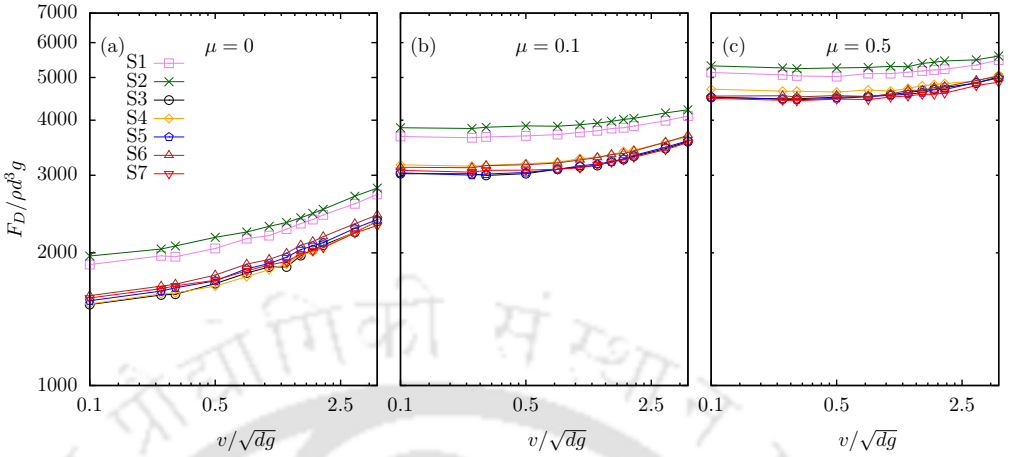

Figure 3.4: The variation of drag on an intruder at low velocity in the range ($0.1\sqrt{dg}$ to $4\sqrt{dg}$) for μ (a) 0.0, (b) 0.1, and (c) 0.5 on a log-log scale for all the shapes.

the constant drag regime to exist until $v/\sqrt{dg} \approx 1.23$. Both definitions predict a constant drag regime in the velocity range very close to what we have observed in our study. While it is not clear how this definition of Fr can be extended to non-spherical intruders, we observe that the constant drag regime occurs for almost the same velocity range for all the shapes.

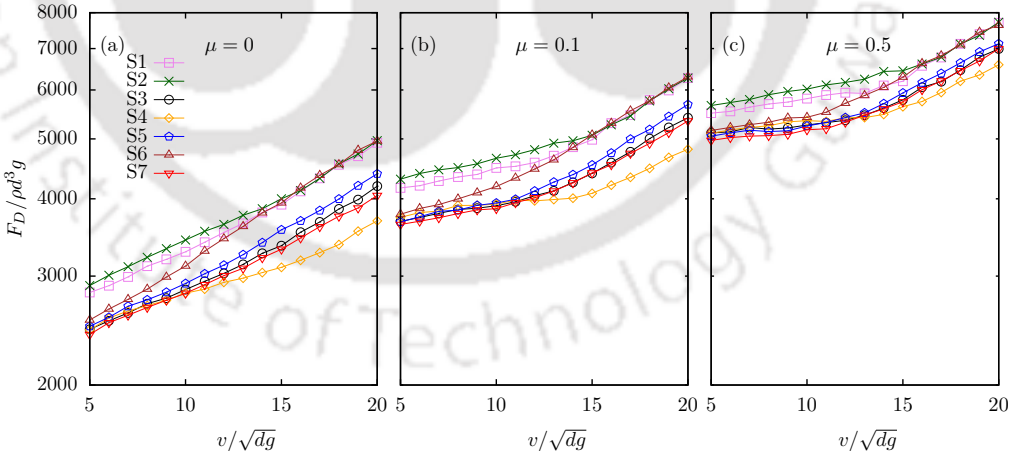

Figure 3.5: The variation of drag on an intruder with at intermediate to high velocity in the range ($5\sqrt{dg}$ to $20\sqrt{dg}$) for μ (a) 0.0, (b) 0.1, and (c) 0.5 on a semi-log scale for all the shapes.

Beyond the constant drag regime that is observed at low intruder velocities for frictional system (see Fig 3.4), whereas the drag on the intruder increases with velocity for all the system (see Fig 3.5). The slope of the curve on the log-log plot seems to be

varying with v suggesting that, for some constant a, $F_D \propto v^a$ is not valid for a granular medium. The kinetic drag contribution to the drag F_K dominates yield drag F_Y at high velocities. This can be observed in the insets of Fig. 4.2 where $\psi = F_D/v^2$ approaches a constant value. We shall elaborate further on F_K and the drag regimes in the next subsection. By comparing directly the values of F_D at higher velocities ($v > 10\sqrt{dg}$), we note that the drag forces are in the order: $F_{D,S1} \approx F_{D,S2} \approx F_{D,S6} > F_{D,S5} > F_{D,S3} \approx F_{D,S7} > F_{D,S4}$, where $F_{D,i}$ is the drag F_D for shape i. Even though the differences are not large, this trend is observed consistently for all velocities higher than $10\sqrt{dg}$, and for all μ considered in our study. At velocities lower than 1.23 ($v/\sqrt{(}dg) < 1.23$), the trend is: $F_{D,S2} > F_{D,S1} > F_{D,S6} \approx F_{D,S5} \approx F_{D,S3} \approx F_{D,S7} \approx F_{D,S4}$.

Albert *et al* [9], in their study of the effect of shape of slowly moving object in a granular medium on jamming of grains around the object, highlighted that (a) streamlining the intruder significantly reduces the resistance offered by the granular medium to its motion, and (b) the increase in the drag on intruders that are longer in the flow direction is due to the creation of a more jammed state in front of the intruder. [10] demonstrated that the local surface stress on an intruder is approximately equal to that on a plate oriented at the same angle as the local surface and moving at the same velocity and depth. Therefore, one could calculate the forces on an intruder by summing up the individual contributions of these stresses.

At low velocities (see Fig. 4.2), it is evident that streamlining an object significantly reduces the drag. An example of this would be the shapes S2 (a rectangle) and S4 (an ellipse) of $20d \times 10d$ along x and y, respectively. Since an ellipse is more streamlined than a rectangle of similar dimensions, the latter has a higher drag than the former. The streamlining of a body reduces the drag since the force chains applying a force of f_P^{fc} at a point P on the intruder contributes only $f_P^{fc} \sin\gamma$ to the drag, where γ is the tangential orientation of the intruder at point P with x axis ($\gamma = 0$ corresponds to the direction of motion). If the force chains developed were equally strong, streamlining of a body would significantly reduce drag.

Moreover, similar shapes such as S3, S4, and S5 have identical drag at low velocities suggesting that viscosity is not a major contribution to the drag force in granular media [9]. Although S4 is the longest shape and it creates the most jammed force chains in front of itself compared to S3 and S5, the force chains tend to occur more laterally, thus, contributing less to the drag. However, it must be emphasized that if the bodies are equally streamlined, the drag increases with the length of the intruder at low velocities

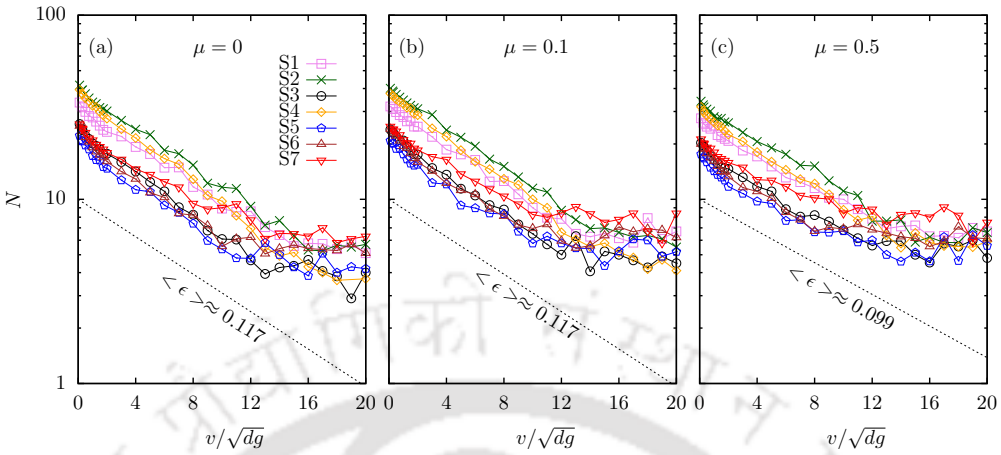

Figure 3.6: The variation of the mean number of contacts N on an intruder with the velocity at (a) $\mu = 0$, (b) $\mu = 0.1$, and (c) $\mu = 0.5$ for all the shapes in our study.

as can be seen from F_D for shapes S1 and S2 (Fig. 3.3) This is because longer shapes delay the collapse of force chains in the intruder's wake allowing those with higher stress to be formed in front of the intruder. Also since the forward facing surfaces of S1, S2 and S6 are blunt ($\sin\gamma = 1$), the force chains contribute more to drag compared to the other shapes. Moreover, the triangle S6 allows the force chains to collapse almost immediately and thus, has lower drag than S1 or S2. S7 is also streamlined and, therefore, has less drag than S1 or S2 at lower velocities. This will be shown in later subsections.

As previously stated, at higher velocities, the drag forces are in the order $F_{D,S1} \approx F_{D,S2} \approx F_{D,S6} > F_{D,S5} > F_{D,S3} \approx F_{D,S7} > F_{D,S4}$. Firstly, S1, S2 and S6 are subject to an approximately equal drag, unlike at low velocities. Interestingly, [10] showed that stress acting on a flat plate being dragged in granular media is identical to the small element on the intruder with a similar orientation to the flow γ, irrespective of the shape of the intruder. Since the front faces (side facing the flow) of these three intruders are oriented at the same angle to the flow, they experience the same magnitude of stress on the front face. Additionally, the other faces contribute very little to the drag as they do not experience contacts with the grains. This leads to the three shapes S1, S2 and S6 having an identical drag. It is noteworthy that, at low velocities, the drag is not equal for the three shapes, because of the way these shapes hinder the jamming and collapse of grains around them. Other shapes with curved front surfaces experience a lower drag than S1, S2, and S6. The curved surfaces contribute $\sin\gamma < 1$ times the normal force on the intruder's surface to the drag. Therefore, the more blunt an object is, the more drag

it experiences. Hence, S5 has a lower drag than S1, S2, and S6, but higher than S3. As the shape becomes less blunt, the drag is further reduced with S4 having a lower drag than S3. Interestingly, S7 also has a higher F_D than S4 because two of the sides of S7 are tilted at an angle of $\pi/3$ to the flow. This is very close to the angle at which a plate moved through granular media experiences the maximum stress [10]. S3 and S7 experience similar drag due to the summation of drag components being almost similar. We discuss the force profiles on the intruders in Sec. 3.3.5.

3.3.2 Number of contacts, kinetic drag, and drag regimes

In order to understand the forces acting on an intruder, it is imperative to reflect on the role of the grains in contact with the intruder: it is these grains that are 'directly' responsible for the forces. The average number of grain contacts, N, changes with the intruder's shape as well as its velocity. Therefore, in this subsection, we present our results and discussion on N and the relation between N, F_K and the drag regimes.

Table 3.1: Comparison of ϕ obtained from numerical simulations and the theoretical estimate, l_{cs}/S.

Shape	$\phi_{\text{simulations}}$	$\phi = l_{cs}/S$
S1	0.20	0.25
S2	0.24	0.20
S3	0.22	0.32
S4	0.17	0.21
S5	0.27	0.37
S6	0.30	0.33
S7	0.34	0.33

The number of contacts N is calculated by averaging over several configurations after the intruder has reached a steady-state behavior, *i.e.*, when the drag force fluctuates around a well-defined mean. Of course, N is a strong function of the shape of the intruder, but it does not imply that two shapes with same number of contacts at a given v experience equal forces. For example, a blunt and a streamlined object may have a similar number of contacts.

The variation of N with v is shown in Fig. 3.6 (a), (b), and (c) on a semi-log plot for $\mu = 0$, 0.1, and 0.5, respectively. Two distinct regimes can be identified; an exponential one in which $N \propto e^{\epsilon v}$, with ϵ constant, and a second in which $N = N_\infty$ is constant. The

latter seems to be in the same velocity range in which the v^2 dependence of drag force is expected. Although we do not exactly understand the physical picture behind this saturation, it is consistently present for all the shapes and for all the μ considered in our study. However, this saturation value can be approximated as $N_\infty \approx \Phi l_{cs}/d$, where Φ is the packing fraction of the bed and l_{cs} is the cross-section length perpendicular to the direction of motion. Let $\phi = N_\infty/N_0$ where N_0 is the number of contacts in the yield limit, which is roughly equal to $\Phi S/d$ where S is the perimeter of the obstacle. Therefore, $\phi \approx l_{cs}/S$. We have compared this rough theoretical estimate of ϕ with that obtained from the numerical simulations in Table 3.1. Additionally, we observe that $\epsilon \approx -0.1$ as can be seen in Fig. 3.6 (a), (b), and (c) and the value of ϵ for each individual shape and μ is presented in Table 3.2.

Based on plots of F_D and N versus v for $\mu \geq 0$ and by comparing their respective behaviors for all the intruder shapes considered in the present study, we propose a three-regime model for the average drag force F_D acting on the intruder. In the first, which is observed in the range $1 < v/\sqrt{dg} < 4$, the drag is constant; the second occurs in the range $8 < v/\sqrt{dg} < 12$ and the third for $10 < v/\sqrt{dg} < 12$. In the remainder of this subsection, we explore the dependence of the kinetic drag on the velocity for each of these regimes.

Each contact exerts a force on the intruder whose magnitude depends on its location with respect to the intruder's line of motion. It is difficult to correlate the average number of contacts N with the force on the intruder. A previous study [25] proposed $F_K \propto Nv^\zeta$ with $\zeta = 1$, but they considered only the first two drag regimes. Here we assume that ζ can vary depending on the regime:

$$\text{Regime I:} \quad F_K = 0 \tag{3.1}$$

$$\text{Regime II:} \quad F_K = \alpha v^{\zeta_1} N/N_0 = \alpha \exp(\epsilon v) v^{\zeta_1} \tag{3.2}$$

$$\text{Regime III:} \quad F_K = \beta v^{\zeta_2} N/N_0 = \beta v^{\zeta_2} l_{cs}/S \tag{3.3}$$

where α and β are constants. Parameters corresponding to the best fit of these equations to our simulation data, along with their coefficient of determination, are presented in Table 3.2. In regime II, it can be seen that $\zeta_1 \approx 1$ for all shapes in accord with the previous results [25] for $\mu > 0$. As for the regime III, $\zeta_2 \approx 2$ is consistent with a v^2 dependence of kinetic drag with velocity. Except for the frictionless ($\mu = 0$) systems where the trends are not clear, the proposed regimes work well for all the shapes with $\zeta_1 \approx 1$ and $\zeta_2 \approx 2$.

Table 3.2: The values of fits and constants

Shape	μ	$-\epsilon$	ζ_1	$R^2_{\zeta_1}$	ζ_2	$R^2_{\zeta_2}$
	0.0	0.133	1.064	0.981	1.970	0.983
S1	0.1	0.120	1.319	0.993	2.168	0.973
	0.5	0.099	1.296	0.999	2.411	0.976
	0.0	0.115	1.106	0.984	2.244	0.974
S2	0.1	0.119	1.403	0.997	2.591	0.991
	0.5	0.100	1.440	0.961	2.420	0.986
	0.0	0.126	1.130	0.986	1.752	0.922
S3	0.1	0.123	1.290	0.997	1.938	0.942
	0.5	0.099	1.186	0.991	2.094	0.955
	0.0	0.132	1.126	0.993	2.143	0.988
S4	0.1	0.133	1.301	0.997	2.300	0.978
	0.5	0.116	1.363	0.991	2.188	0.975
	0.0	0.122	1.063	0.983	1.422	0.905
S5	0.1	0.113	1.25	0.994	1.746	0.945
	0.5	0.090	1.191	0.979	2.022	0.945
	0.0	0.122	1.106	0.981	1.296	0.966
S6	0.1	0.113	1.327	0.998	1.601	0.951
	0.5	0.094	1.296	0.993	2.08	0.976
	0.0	0.092	1.001	0.994	1.579	0.951
S7	0.1	0.099	1.292	0.997	1.807	0.911
	0.5	0.073	1.225	0.983	2.147	0.932
	0.0	-	1.001	-	1.579	-
Mean	0.1	-	1.292	-	1.807	-
	0.5	-	1.225	-	2.147	-

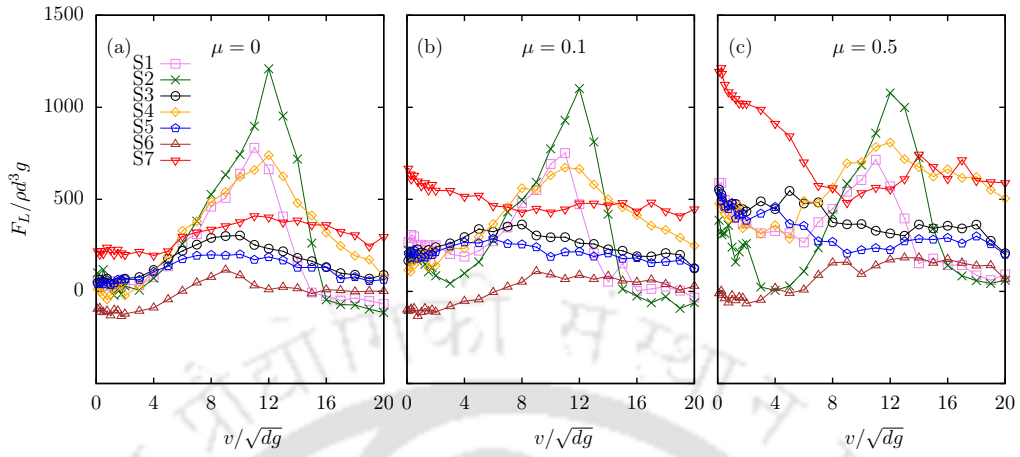

Figure 3.7: The variation of lift on an intruder with the velocity at (a) $\mu = 0$, (b) $\mu = 0.1$, and (c) $\mu = 0.5$ for all the shapes in our study.

3.3.3 Lift on the moving intruder

The component of the force on the intruder perpendicular to the flow direction is defined as the lift force, F_L. Figure 3.7 shows the variation in F_L as a function of the intruder's velocity (v) for various coefficients of friction (μ = 0, 0.1 and 0.5). For a clear exposition of the trends, we consider three velocity regimes: (i) low velocities ($0.1 < v/\sqrt{dg} < 4$); (ii) intermediate velocities ($6 < v/\sqrt{dg} < 14$); and (iii) high velocities ($14 < v/\sqrt{dg} < 20$). For $\mu = 0.0$ (Fig. 3.7(a)), a maximum in F_L for all intruder shapes is observed in the intermediate velocity regime and is ordered as follows: $F_{L,S2} > F_{L,S1} > F_{L,S4} > F_{L,S7} > F_{L,S3} > F_{D,S5} > F_{L,S6}$. For most of the shapes F_L saturates in the third regime. The highest F_L is observed for $S2$ (rectangle) in the intermediate regime. In both the frictional and frictionless systems the maximum lift force for this shape is observed at $v/\sqrt{dg} = 12$, followed by a sharp decrease. The non-monotonic behavior of the lift force is result of flow detachment from the intruder. An example is shown in Fig. 3.8 depicting simulation snapshots of the flow region around the $S2$ shape for $\mu = 0.0$ at different velocities. For $v/\sqrt{dg} = 1$ the granular particles just slide past the intruder without leaving a trail behind it. At $v/\sqrt{dg} = 8$ the flow detachment from the upper surface of the intruder is evident. This can be attributed to the presence of a free surface at the top and a confined wall at the bottom of the assembly of particles. As a result, the particles below the intruder exert a net upward force. As v increases, flow detachment continues to occur only from above the intruder but not below it. The expansion of flow detachment above the intruder is observed until $v/\sqrt{dg} = 12$. Beyond $v/\sqrt{dg} = 12$, however, the intruder

imparts more energy to the granular particles in its path, which eventually results in flow detachment from both the upper and lower surfaces as shown in Fig. 3.8 (d) for $v/\sqrt{dg} = 18$. The $S1$ and $S2$ shapes, both having flat surfaces around the sides, show simillar flow behaviour (Fig 3.8 and 3.9). The intruder shapes $S3$, $S4$ and $S6$, having different radius of curvature in the direction of movement, exhibit low flow detachment up to $v/\sqrt{d/g} = 12$ and beyond that at higher velocities the flow detachment is more (see Fig 3.10, 3.11 and 3.12). The equilateral triangle $S6$, having a flat surface perpendicular the direction of movement (like $S1$ and $S2$), and developes flow detachment from the upper surface up to a certain velocity and later at high velocities flow detachment occurs from both the top and bottom of the shape (Fig 3.13). $S7$ has a pointy edge in the front with its tilted sides in the direction of motion shows low flow detachment up to $v/\sqrt{d/g} = 12$ (Fig 3.14). A large void is witnessed only when the intruder is moving at high velocity of $v/\sqrt{dg} \geq 18$. In a confined system we might not witness such large voids but as our system is open at the top it is possible and a similar behaviour has been oberved by [11] at very high intruder velocities.

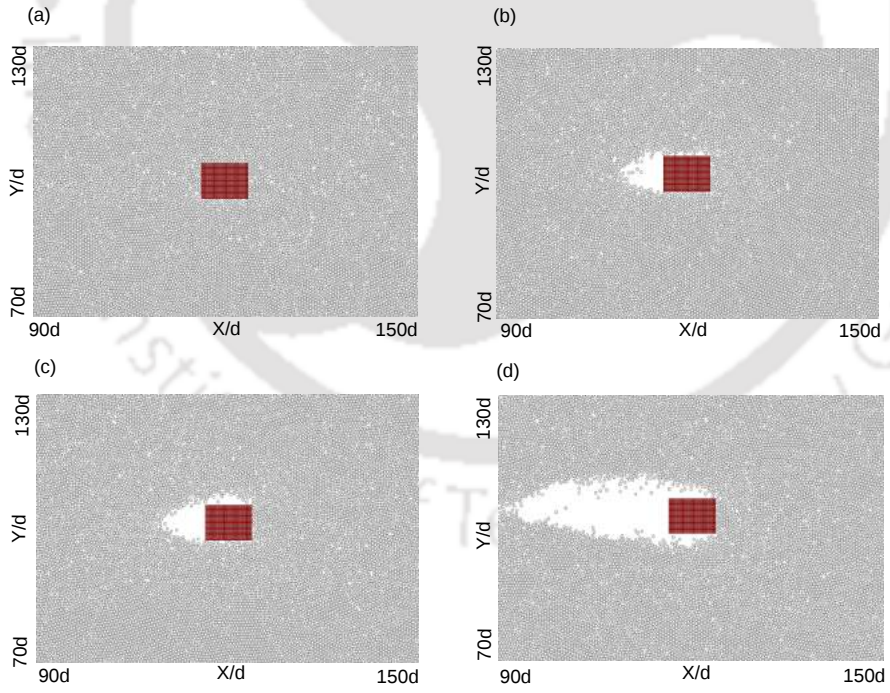

Figure 3.8: Snapshots showing the region around the $S2$(rectangle) intruder for $\mu = 0$ at different intruder velocities ($v/\sqrt{dg}$) (a) 1, (b) 8, (c) 12 and (d) 18.

It is generally observed that above a certain velocity particle contact only occurs on the leading side of the intruder with flow detachment from both its top and bottom

surfaces. This flow detachment plays an important role in the decrease of F_L beyond a certain v for shapes $S1$ (square), $S2$ (rectangle) and $S4$ (ellipse with the major axis aligned with the x-direction), compared to the other intruders. The lift force on the equilateral triangle $S7$ (with an edge pointing to the moving direction), disc $S3$, and ellipse major $S5$ shapes varies little with v for $\mu = 0.0$. This could be due to the maximum particle interaction being concentrated on the frontal part. Interestingly, a negative F_L is observed for an equilateral triangle with its edge pointing opposite to its direction of motion ($S6$) in the low velocity regime. In this case, particles traversing the edges of the blunt surface exert more force on the upper inclined surface than that on the lower one. This is because the particles fall on the upper inclined surface of $S6$, while the particles have to move against gravity to reach the lower inclined surface. It is also evident that the lift force saturates for most of the shapes in the high velocity regime.

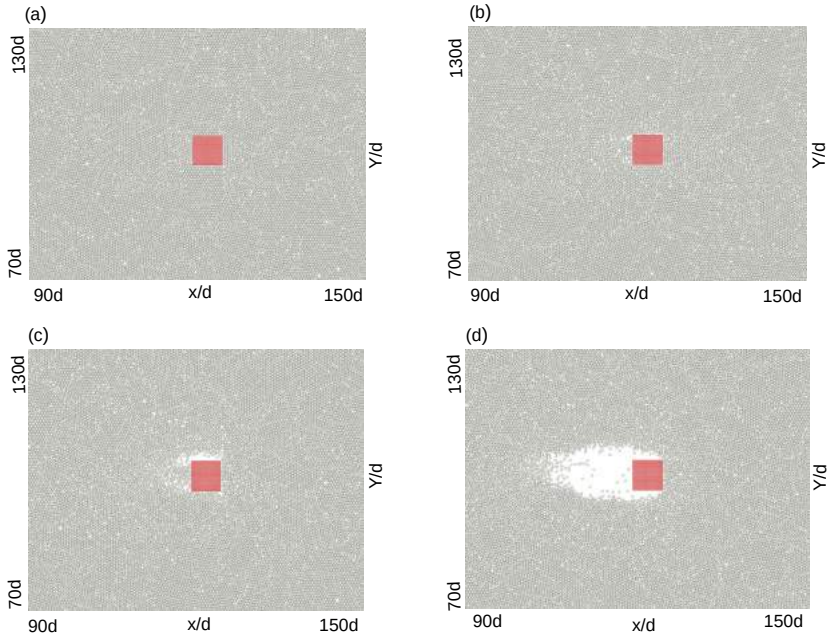

Figure 3.9: Snapshots showing the region around the $S1$ (square) intruder for $\mu = 0$ at different intruder velocities ($v/\sqrt{dg}$) (a) 1, (b) 8, (c) 12 and (d) 18.

For systems with friction coefficients $\mu = 0.1$ and 0.5, the lift forces on $S1, S2$ and $S4$ are higher than on the other shapes in the intermediate velocity regime. The reason is the flow detachment and the larger contact surface around the top and bottom region of the intruder. The lift force on shapes $S3, S5$, and $S6$ shows little variation for $\mu = 0.1$ for a range of v, while for $\mu = 0.5$ the lift force is higher for $S3$ and $S5$, in the low velocity

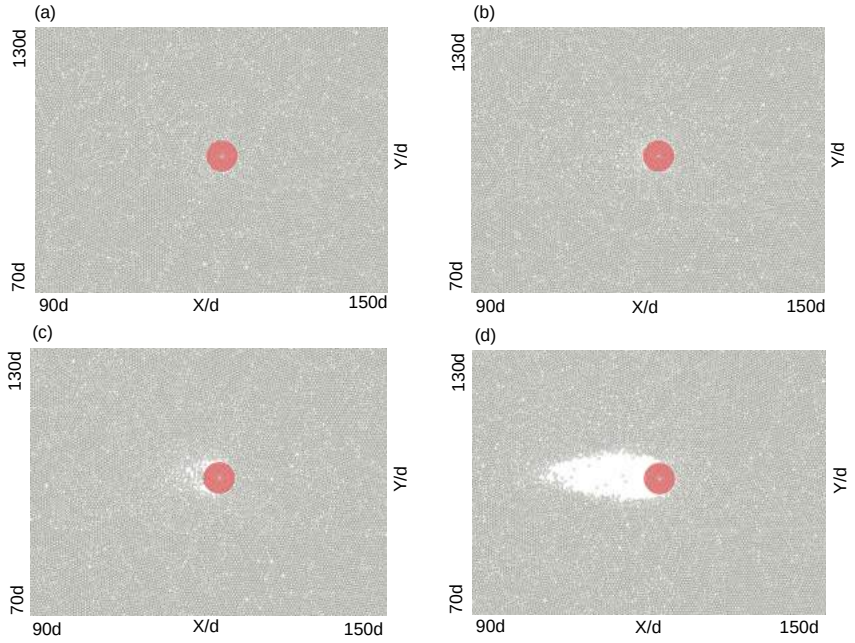

Figure 3.10: Snapshots showing the region around the $S3$ (disc) intruder for $\mu = 0$ at different intruder velocities ($v/\sqrt{dg}$) (a) 1, (b) 8, (c) 12 and (d) 18.

regime and then gradually saturates in the high velocity regime. Unlike the other shapes, the net lift force on $S6$ is small for all values of μ and is negative in the low velocity regime.

The two equilateral triangles $S6$ and $S7$ have different orientations (edges pointing opposite and along the moving direction, respectively). This significantly impacts the F_L experienced by the two shapes as seen in Fig. 3.7. Ding *et al.* have also stated that F_L is sensitive to the cross-section of the intruder.The triangle $S7$ has higher F_L than the triangle $S6$ for all the friction coefficients. The particles in front of the intruder collide with a flat surface in the case of $S6$, whereas they collide with a "V" shaped surface with its edge pointing in the direction of the intruder's motion for the case of $S7$. For $\mu = 0.1$ the lift force is a maximum in the low velocity regime for $S7$ and gradually saturates at higher velocity (Fig. 3.7(b)). The triangle $S7$ has an pointed edge at the moving direction of intruder with its two frontal surfaces inclined to each other at 60° angle and a blunt back. It does have a larger area for particle contact at the leading surface. At low velocities the particles coming into contact with the upper inclined surface slide past the intruder, while there is an accumulation of particles at the bottom front surface due to the confining wall at the bottom. This results in a push in the positive

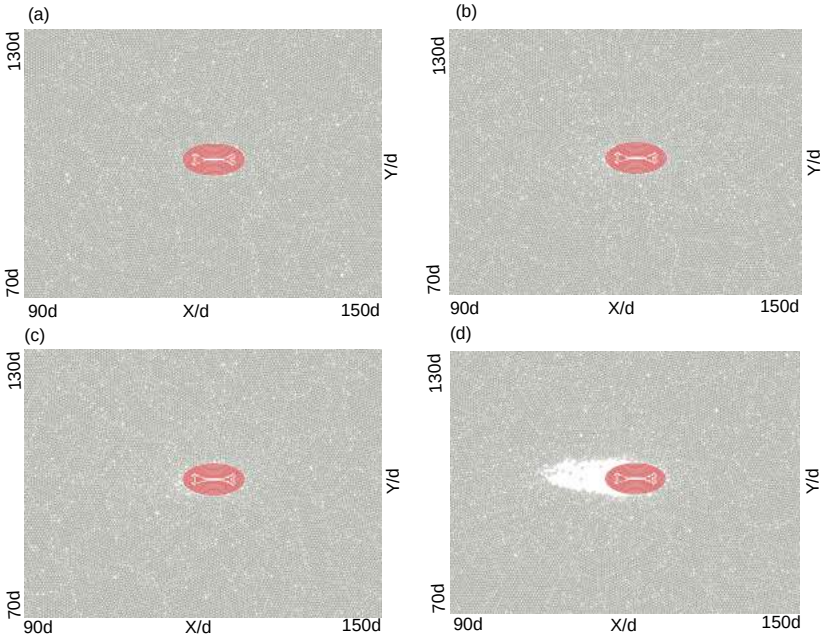

Figure 3.11: Snapshots showing the region around the $S4$ (an ellipse with major axis aligned with the x-direction) intruder for $\mu = 0$ at different intruder velocities ($v/\sqrt{dg}$) (a) 1, (b) 8, (c) 12 and (d) 18.

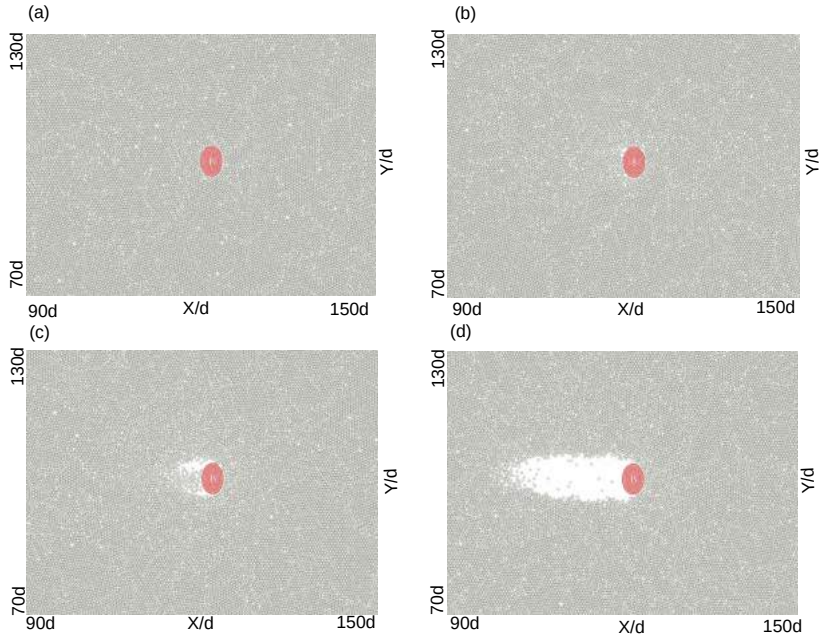

Figure 3.12: Snapshots showing the region around the $S5$ (ellipse with minor axis aligned with the x- direction) intruder for $\mu = 0$ at different intruder velocities ($v/\sqrt{dg}$) (a) 1, (b) 8, (c) 12 and (d) 18.

y-direction. This may explain why $S7$ has a higher F_L in the low velocity regime. Another

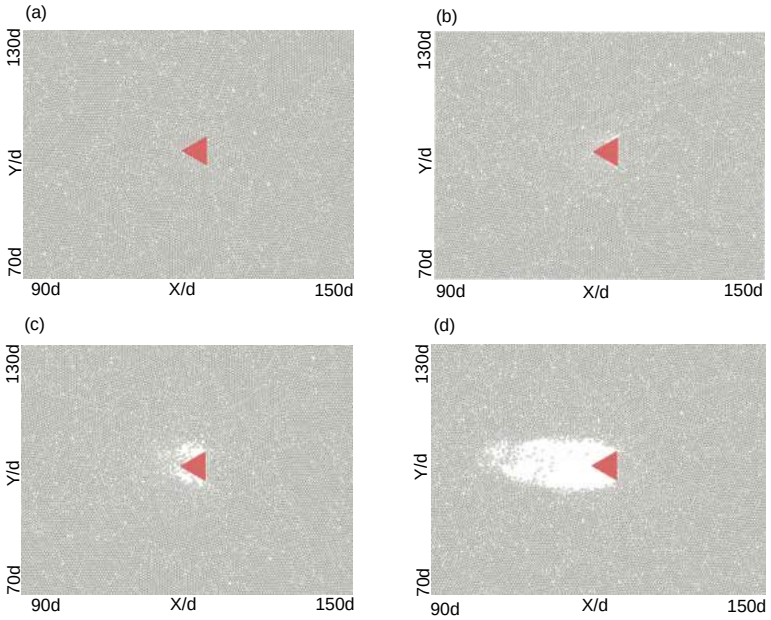

Figure 3.13: Snapshots showing the region around the $S6$ (equilateral triangle with edge pointing opposite to the moving direction) intruder for $\mu = 0$ at different intruder velocities ($v/\sqrt{dg}$) (a) 1, (b) 8, (c) 12 and (d) 18.

interesting observation is the independence of F_L on the intruder's velocity in the range $0.1 < v/\sqrt{dg} < 2$ for $\mu = 0.0$ for all the shapes. This behavior is in contrast with the drag force, for which a gradual increase is observed with intruder velocity. For both frictional and frictionless systems, the maximum F_L is observed for $S2$ (rectangle) in the intermediate velocity regime. The lift force has a dependence on the orientation of the intruder, for example, $S6$ and $S7$ exhibited completely different behavior to each other.

3.3.4 Depth-dependence of forces on the moving intruder

Albert *et al* [9] observed a nonlinear depth dependence of the drag force on a discrete object moving at a low velocity immersed in a granular bed at a depth of 40 - 150 mm (equivalent to 44 - 166 granular bed particles depth). [29] observed a depth-independent drag force on a cylindrical object immersed deep (120 particle lengths or more) in a granular medium and rotated about the vertical axis. A few studies [11, 30, 31] also reported a linear depth dependence. In the context of these results, we compare F_D on the different intruder shapes as a function of their immersion depth in Fig. 3.15 (a) and

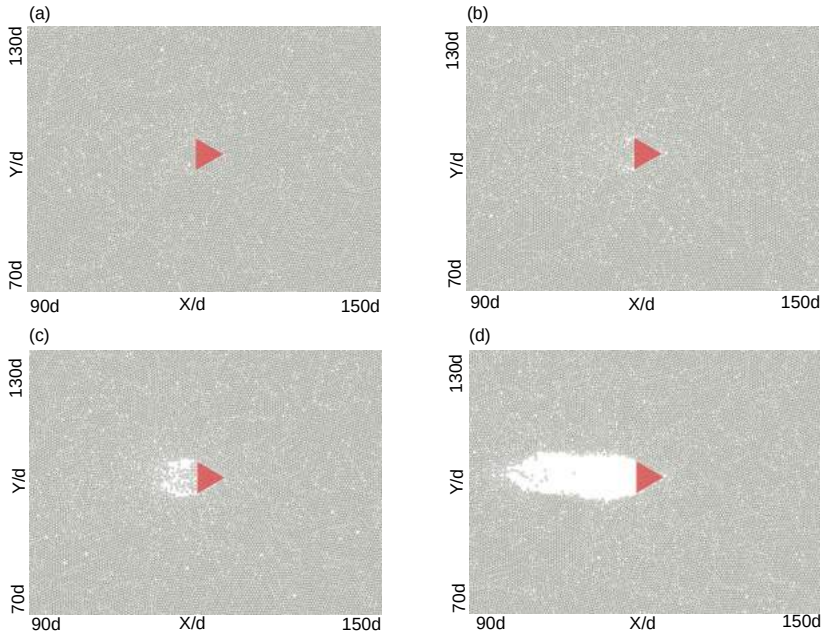

Figure 3.14: Snapshots showing the region around the $S7$ (equilateral triangle with edge pointing along the moving direction) intruder for $\mu = 0$ at different intruder velocities ($v/\sqrt{dg}$) (a) 1, (b) 8, (c) 12 and (d) 18.

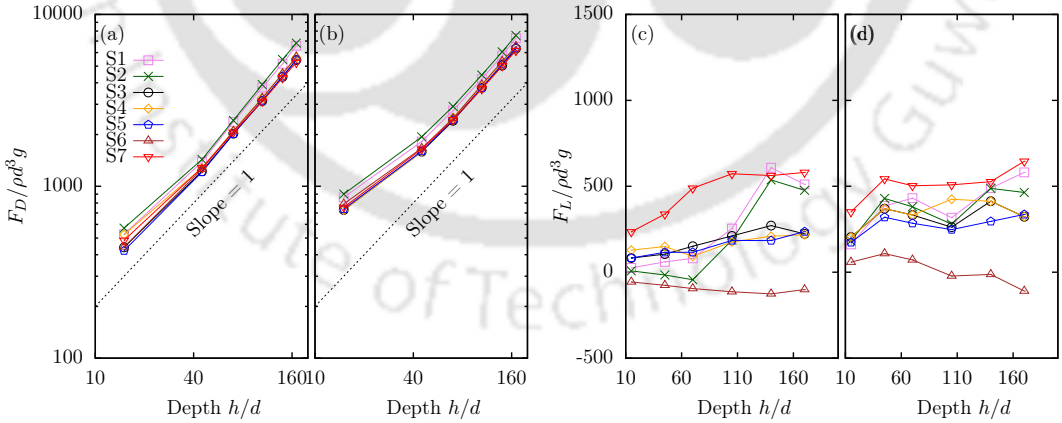

Figure 3.15: The variation of drag force on an intruder at $\mu = 0.1$ with depth for (a) $v/\sqrt{dg} = 1$ and (b) $v/\sqrt{dg} = 5$ on a log-log scale. The dotted line represents a straight line of slope 1 on the log-log scale. The variation of lift force on an intruder at $\mu = 0.1$ with depth for (c) $v/\sqrt{dg} = 1$ and (d) $v/\sqrt{dg} = 5$ on a linear scale.

(b). The results are shown for two intruder velocities $v/\sqrt{dg}$= 1 and 5 at $\mu = 0.1$. In the simulations, the intruder is placed at six different depths $h/d = 15, 45, 70, 105, 140, 170$. F_D increases linearly with an increase in h/d for all the intruders considered here, confirming that the drag is proportional to the hydrostatic pressure. In granular medium the number of particles above the intruder increases with an increase in its depth thus increasing hydrostatic pressure. The F_D for the various heights h/d at $v/\sqrt{dg}$=1 and $\mu = 0.1$ is ordered: $F_{D,S2} > F_{D,S1} > F_{D,S4} \approx F_{D,S7} \approx F_{D,S3} \approx F_{D,S5} \approx F_{D,S6}$. The same trend is also observed for $v/\sqrt{dg} = 5$. The shapes $S1$ and $S2$ experience the maximum drag for all h/d for the two v shown in the plots while the other shapes have identical F_D within five percent of each other at a particular depth. Moreover, the difference between the highest ($S2$) and lowest ($S7$) drag forces calculated for one random depth is not more than 25%.

It has been reported in the literature that the lift force either saturates [14, 15] or increases [10] with the immersion depth of intruder in a granular medium. To determine the shape and depth dependence, we plot the lift force F_L as a function of h/d for two intruder velocities, $v/\sqrt{dg}$=1 and 5, at $\mu = 0.1$ in Fig. 3.15 (c) and (d). Minimal change in lift force for intruders $S3$, $S4$ and $S5$ is observed at $v/\sqrt{dg} = 1$. The lift force on intruders $S1$ and $S2$ increases sharply below a certain depth for $v/\sqrt{dg} = 1$. For the same velocity F_L on $S7$ increases up to a certain depth and then saturates with further increase in the depth. For $v/\sqrt{dg} = 5$ there is a fluctuation in lift force for all the intruders except for $S6$ which shows a gradual decrease in F_L with an increase in h/d. $S6$ and $S7$ with the same geometry but different orientation in the x-direction have the lowest and highest lift forces, respectively for almost at all the depths considered. The lift force acting on $S6$ moving at $v/\sqrt{dg}$=1 shows little variation with depth, while at $v/\sqrt{dg} = 5$ it decreases with the intruder depth.

While the results of Fig. 3.15 suggest that the relation between drag and depth can be easily understood, the same is not true for the lift force, even though both forces result from the repulsive interactions between granular particles and the intruder. The lift force experienced by the intruder also depends upon the number of particle contacts at its upper and lower surface. So the forces depend on the specific region of contact around the intruder surface. Thus, if the force acting perpendicularly on the lower surface is largely due to the particle contacts, then the intruder experiences a positive F_L and otherwise it has a negative F_L. In the next section, we examine the force distribution on the intruder surface and how it influences the drag and lift forces.

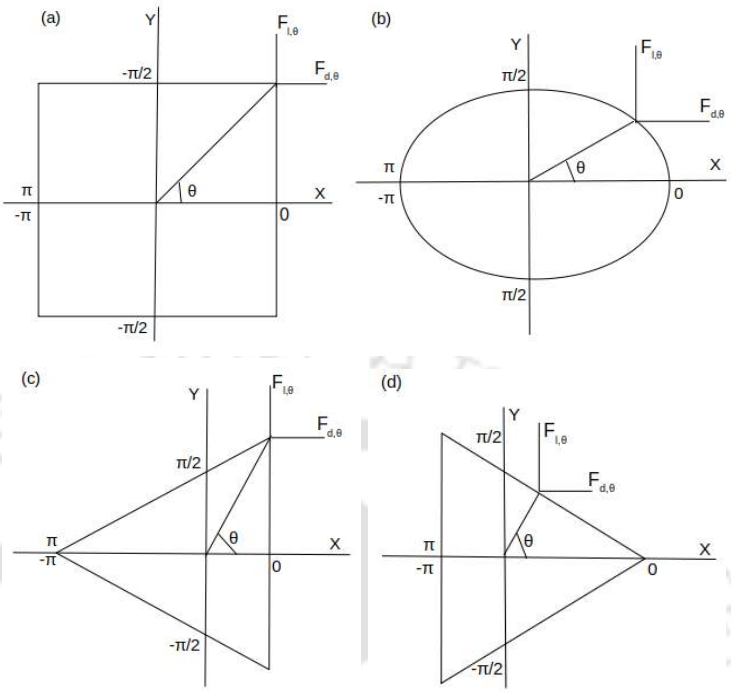

Figure 3.16: Geometric representation of four intruder shapes (a)S1 (a square), (b) S4 intruder (an ellipse with the major axis aligned with the direction of motion of the intruder), (c) S6 (an equilateral triangle with edge pointing opposite to the moving direction), and (d) S7 (an equilateral triangle with edge pointing along the moving direction). The contact position is given by the angle θ with $-\pi < \theta < \pi$ with the upper (lower)half corresponding to positive (negative) values.

3.3.5 Force profile along the surface of the intruder

To develop a better understanding of how the lift and drag forces act around the periphery of a moving intruder, we have examined the force distribution as a function of the angle of contact, θ relative to the centre of the intruder. The geometry and coordinate system for the shapes $S1, S4, S6$, and $S7$, are shown in Fig 3.16 and the force distributions for all objects are shown in Fig 3.17. Angular positions ranging from 0 to π correspond to the upper half of the intruder, while the range $-\pi < \theta < 0$ corresponds to the bottom half of the intruder. $\theta = 0$ is in front of the intruder and $\theta = \pm\pi$ is the back.

Let us examine the distribution of the normalized drag force shown in Fig. 3.17 (a). We first note that the normalized distributions vary only weakly with the intruder velocity. The drag force experienced by the intruder is mainly due to particle contacts at the front. Thus, the shapes $S1, S2$ and $S6$, which present a blunt face in the direction of movement, experience a large contribution to the drag for $|\theta| < \pi/4$ ($S1$ and $S2$) and

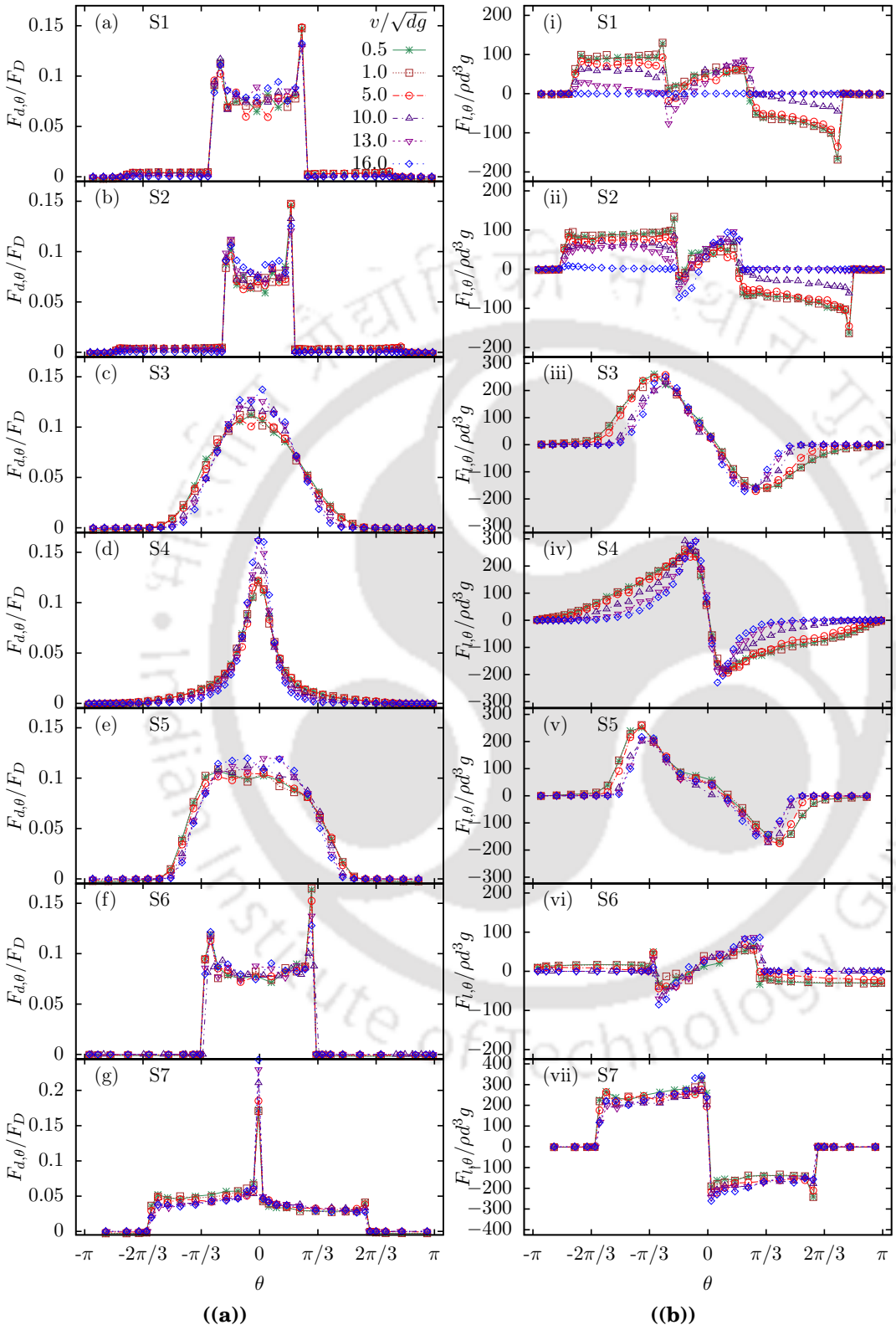

Figure 3.17: The variation of (a) the normalized drag force ($F_{D,\theta}/F_D$) and (b) lift force ($F_{l,\theta}$) around the intruder surface for various intruder velocities. Please refer to Fig. 3.16 for the definition of θ.

$|\theta| < \pi/3$ ($S6$). A sharp increase in drag is observed at the leading edges $\theta = \pm\pi/4$ ($S1$ and $S2$) and $\theta = \pm\pi/3$ ($S6$). This happens because when the blunt-faced intruder moves within the medium, it pushes the particles along with it, and the colliding particles then gradually slide on the intruder surface along the leading corner edges. Due to this, there is maximum perpendicular contact at the edges, and the drag force is higher in that region. There are more particle contacts at the backside of the intruder at low velocities compared with the case of high velocities(no visible contacts as shown in Fig. 3.9). Though the particles exert minimal contact forces on the trailing edges as they just slide down due to gravity after contacting the leading surface of the intruder. Thus the contribution to the drag force is almost zero for $\pi/4 < |\theta|$ ($S1$ and $S2$) and $\pi/3 < |\theta|$ ($S6$). The shapes $S3, S4, S5$ and $S7$ all have a maximum drag force for $\theta = 0$. The curved intruders $S3$ and $S5$ have a maximum drag force for $\theta = 0$. The shapes $S4$ and $S7$, which have a pointed edge in the direction of motion, experience a higher drag at $\theta = 0$. The triangle $S7$ experiences a maximum drag on its front edges, with a strong spike around $\theta = 0$. There is also a slight asymmetry with a stronger drag force on the lower face. As expected, the drag force on the trailing face is very small.

We now consider the distribution of the (un-normalized) lift force shown in Fig. 3.17 (b). The shapes $S1, S2$, and $S6$, exhibit similar lift force profiles for $|\theta| > \pi/4$ as they present a blunt face in the leading direction. The rectangle S2 experiences high lift force for $-\pi/4 < \theta < -2\pi/3$. The curved intruders $S3, S4$ and $S5$ exhibit a higher positive lift force suggesting a larger number of particle contacts on their lower surface. This is due to their more streamlined form compared to other shapes. The equilateral triangles S6 and S7 exhibit different lift force profiles. The former, with its blunt front face, experiences essentially zero lift on its trailing sides ($\theta > \pi/3$), while $S7$ experiences strong positive lift forces on its lower leading face $-2\pi/3 < \theta < 0$ and a weaker negative lift force on its upper leading face, $0 < \theta < 2\pi/3$. We also note that the lift force profile varies weakly with velocity for shapes $S5, S6$, and $S7$, while for the other shapes the variation is more significant. At high velocities the magnitude of the lift force decreases due to flow detachment [11]. These observations are consistent with the variation of the total lift force with velocity shown in Fig 3.7.

3.4 Conclusions

We have presented extensive numerical simulation results of an intruder dragged horizontally through a granular medium to understand the drag and lift forces it experiences as a function of its velocity (v), immersion depth (h/d), and shape. The drag force gradually increases with v in frictionless systems ($\mu = 0.0$), while when friction is present we observe a constant drag regime at low velocities. For a fixed cross section, the drag force depends weakly on the intruder shape. In contrast, the lift force has a strong shape dependence. It may increase in a certain velocity range but at higher velocities we observe a decrease in the lift force. The intruder shape has a major effect on the distribution of contacts around its surface, which explains the strong lift experienced by certain shapes. The force profiles around the intruder surface, resulting from granular contacts, exhibit a strong angular dependence.

BIBLIOGRAPHY

[1] Heinrich M. Jaeger, Sidney R. Nagel, and Robert P Behringer. Granular solids, liquids, and gases. *Rev. Mod. Phys.*, 68:1259–1273, Oct 1996. doi: 10.1103/RevModPhys.68.1259.

[2] Fengxian Fan, Eric J. R. Parteli, and Thorsten Pöschel. Origin of granular capillarity revealed by particle-based simulations. *Phys. Rev. Lett.*, 118:218001, May 2017. doi :10.1103/PhysRevLett.118.218001.

[3] Sonu Kumar, Manish Dhiman, and K. Anki Reddy. Magnus effect in granular media. *Phys. Rev. E*, 99:012902, Jan 2019. doi: 10.1103/PhysRevE.99.012902.

[4] David J. Goldfarb, Benjamin J. Glasser, and Troy Shinbrot. Shear instabilities in granular flows. *Nature*, 415(6869):302–305, Jan 2002. doi: 10.1038/415302a.

[5] Jan Ludvig Vinningland, Øistein Johnsen, Eirik G. Flekkøy, Renaud Toussaint, and Knut Jørgen Måløy. Granular rayleigh-taylor instability: Experiments and simulations. *Phys. Rev. Lett.*, 99:048001, Jul 2007. doi: 10.1103/PhysRevLett.99.048001.

[6] Angel Huminic and Gabriela Huminic. Aerodynamic study of a generic car model with wheels and underbody diffuser. *International Journal of Automotive Technology*, 18(3):397–404, Jun 2017. doi: 10.1007/s12239-017-0040-6.

[7] D M Bushnell. Aircraft drag reduction—a review. *Proceedings of the Institution of Mechanical Engineers, Part G: Journal of Aerospace Engineering*, 217(1):1–18, 2003. doi: 10.1243/095441003763031789.

[8] R. Albert, M. A. Pfeifer, A.-L. Barabási, and P. Schiffer. Slow drag in a granular medium. *Phys. Rev. Lett.*, 82:205–208, Jan 1999. doi: 10.1103/PhysRevLett.82.205.

[9] I. Albert, J. G. Sample, A. J. Morss, S. Rajagopalan, A.-L. Barabási, and P. Schiffer. Granular drag on a discrete object: Shape effects on jamming. *Phys. Rev. E*, 64:061303, Nov 2001. doi: 10.1103/PhysRevE.64.061303.

[10] Yang Ding, Nick Gravish, and Daniel I. Goldman. Drag induced lift in granular media. *Phys. Rev. Lett.*, 106:028001, Jan 2011. doi: 10.1103/PhysRevLett.106.028001.

[11] Fabricio Q. Potiguar and Yang Ding. Lift and drag in intruders moving through hydrostatic granular media at high speeds. *Phys. Rev. E*, 88:012204, Jul 2013. doi: 10.1103/PhysRevE.88.012204.

[12] Hiroaki Katsuragi, Katha Anki Reddy, and Keita Endo. Shape dependence of resistance force exerted on an obstacle placed in a gravity-driven granular silo flow. *AIChE Journal*, 64(11):3849–3856, 2018. doi: https://doi.org/10.1002/aic.16205.

[13] Fabricio Q. Potiguar. Lift force on an asymmetrical obstacle immersed in a dilute granular flow. *Phys. Rev. E*, 84:061302, Dec 2011. doi: 10.1103/PhysRevE.84.061302.

[14] François Guillard, Yoël Forterre, and Olivier Pouliquen. Lift forces in granular media. *Physics of Fluids*, 26(4):043301, 2014. doi: 10.1063/1.4869859.

[15] Bhanjan Debnath, K. Kesava Rao, and Prabhu R. Nott. The lift on a disc immersed in a rotating granular bed. *AIChE Journal*, 63(12):5482–5489, 2017. doi: https://doi.org/10.1002/aic.15991.

[16] Ryan D. Maladen, Yang Ding, Chen Li, and Daniel I. Goldman. Undulatory swimming in sand: Subsurface locomotion of the sandfish lizard. *Science*, 325(5938):314–318, 2009. doi: 10.1126/science.1172490.

[17] Yang Ding, Sarah S. Sharpe, Andrew Masse, and Daniel I. Goldman. Mechanics of undulatory swimming in a frictional fluid. *PLOS Computational Biology*, 8(12):1–13, 12 2012. doi: 10.1371/journal.pcbi.1002810.

[18] P. A. Cundall and O. D. L. Strack. A discrete numerical model for granular assemblies. *Géotechnique*, 29(1):47–65, 1979. doi: 10.1680/geot.1979.29.1.47.

[19] Nikolai V. Brilliantov, Frank Spahn, Jan-Martin Hertzsch, and Thorsten Pöschel. Model for collisions in granular gases. *Phys. Rev. E*, 53:5382–5392, May 1996. doi: 10.1103/PhysRevE.53.5382,.

[20] Leonardo E. Silbert, Deniz Ertaş, Gary S. Grest, Thomas C. Halsey, Dov Levine, and Steven J. Plimpton. Granular flow down an inclined plane: Bagnold scaling and rheology. *Phys. Rev. E*, 64:051302, Oct 2001. doi: 10.1103/PhysRevE.64.051302.

[21] Thomas Schwager and Thorsten Pöschel. Coefficient of normal restitution of viscous particles and cooling rate of granular gases. *Phys. Rev. E*, 57:650–654, Jan 1998. doi: 10.1103/PhysRevE.57.650.

[22] Steve Plimpton. Fast parallel algorithms for short-range molecular dynamics. *Journal of Computational Physics*, 117(1):1–19, 1995. doi: https://doi.org/10.1006/jcph.1995.1039.

[23] Alexander Stukowski. Visualization and analysis of atomistic simulation data with OVITO-the Open Visualization Tool. *Modelling and simulation in materials science and engineering*, 18(1), Jan 2010. doi: 10.1088/0965-0393/18/1/015012.

[24] Yuka Takehara and Ko Okumura. High-velocity drag friction in granular media near the jamming point. *Phys. Rev. Lett.*, 112:148001, Apr 2014. doi: 10.1103/PhysRevLett.112.148001.

[25] J. E. Hilton and A. Tordesillas. Drag force on a spherical intruder in a granular bed at low froude number. *Phys. Rev. E*, 88:062203, Dec 2013. doi: 10.1103/PhysRevE.88.062203.

[26] Sonu Kumar, K. Anki Reddy, Satoshi Takada, and Hisao Hayakawa. Scaling law of the drag force in dense granular media. *arXiv e-prints*, page arXiv:1712.09057, Dec 2017. https://arxiv.org/abs/1712.09057.

[27] Dengming Wang, Yahui Yang, and Wei Du. The drag on a vibrated intruder moving in the confined granular media. *Powder Technology*, 286:385–391, Dec 2015. doi: https://doi.org/10.1016/j.powtec.2015.08.027.

[28] Satoshi Takada and Hisao Hayakawa. Drag law of two-dimensional granular fluids. *Journal of Engineering Mechanics*, 143(1):C4016004, 2017. doi: 10.1061/(ASCE)EM.1943-7889.0001054.

[29] Fran çois Guillard, Yoël Forterre, and Olivier Pouliquen. Depth-independent drag force induced by stirring in granular media. *Phys. Rev. Lett.*, 110:138303, Mar 2013. doi: 10.1103/PhysRevLett.110.138303.

[30] Fran çois Guillard, Yoël Forterre, and Olivier Pouliquen. Origin of a depth-independent drag force

induced by stirring in granular media. *Phys. Rev. E*, 91:022201, Feb 2015. doi: 10.1103/PhysRevE.91.022201.

[31] Andreea Panaitescu, Xavier Clotet, and Arshad Kudrolli. Drag law for an intruder in granular sediments. *Phys. Rev. E*, 95:032901, Mar 2017. doi: 10.1103/PhysRevE.95.032901.

CHAPTER 4

DRAG ON A CIRCULAR INTRUDER TRAVERSING A SHAPE HETEROGENEOUS GRANULAR MIXTURE[1]

4.1 Introduction

A large solid particle moving through a system of smaller particles has been a topic of interest due to its industrial applications such as mining and related activities. Because of the resemblance to the subsurface flows, it is finding applications in the sand locomotion of robots as well. However, this kind of flows are still not completely understood due to the complex nature of the granular materials [1, 2]. One of the prime focus in these kinds of works is comprehending the drag characteristics on the larger solid particle or intruder due to the surrounding granular particles. In granular media, the drag force depends on various parameters such as the properties of the intruder, the external forces acting on it, the arrangement and the geometry of the particles etc.

In a high-velocity regime, the drag force increases monotonically with the intruder's velocity [3] in a system of spherical particles. Whereas in a low-velocity regime, it is independent of the intruder's velocity [4]. The resistive force or drag force not only depends on the velocity of the intruder but also its direction of motion: Liu *et al* [5] noticed a maximum drag force when the intruder is moved vertically downward in a

[1]The article based upon the work reported in this chapter is under review in *Phys. Rev. E* ; title: Drag on a circular intruder traversing a shape heterogeneous granular mixture; authors: Bitang K Tripura, S Kumar, AVK Reddy and KA Reddy.

gravity system while a minimum drag force when it is moved vertically upward. Albert *et al* [6] stated that the drag force is almost independent of the shape of the intruder in a low-velocity regime. Whereas in another work[7], drag is found to be dependent on the shape of the intruder which is moved at high velocities through spherical particles. The authors further stated that an increase in the flatness of the intruder increases the drag owing to an increase in the number of particle-intruder collisions. The drag force not only depends on the properties of the intruder but also the external forces. For example, the drag is noticed [8–11] to be higher in a confined system than the one with a free surface, due to the presence of the confining pressure. Moreover, the nature of contact forces between the interacting granules in the dense granular medium under high pressure can also impact the granular flow behavior[12]. In addition, the drag increases with an increase in the gravitational acceleration [13]. Even in a gravityless system, the drag was observed to increase with the square of the intruder's velocity [14]. As it may be expected, the drag depends on the properties of the granular media surrounding it. For example, Zhou *et al*[9] reported a higher drag on an intruder traversing a polydispersed granular media than a monodispersed one owing to their packing effects. The drag also depends on the shape of the granular particles. To this end, Zhou *et al.* [11] noticed that drag is more in a system of dumbbell-shaped granules than that of elliptical granules. Further, the authors noticed an increase in the drag with an increase in the aspect ratio of the ellipse particles.

Most of the previous studies on intruder dynamics involved a system of spherical particles. However, in recent decades, understanding the dynamics of non-spherical particles [15–17] has garnered much interest in industrial and academic works. The reason is their relevance to practical applications, where the particles are usually mixtures of variegated shapes and sizes. A special case is a mixture [18, 19] of spherical and non-spherical particles. To the best of our knowledge, there is hardly any work that studied the characteristics of an intruder moving through a mixture of granular particles. In this regard, we probed the drag characteristics of an intruder moving through a mixture of discs and dumbbells in a two-dimensional gravityless system. The study is organised as follows: in the next section, the simulation technique is explained and in section 4.3, the numerical results are reported along with our interpretations and finally, the section 4.4 summarizes our key findings.

4.2 Simulation Methodology

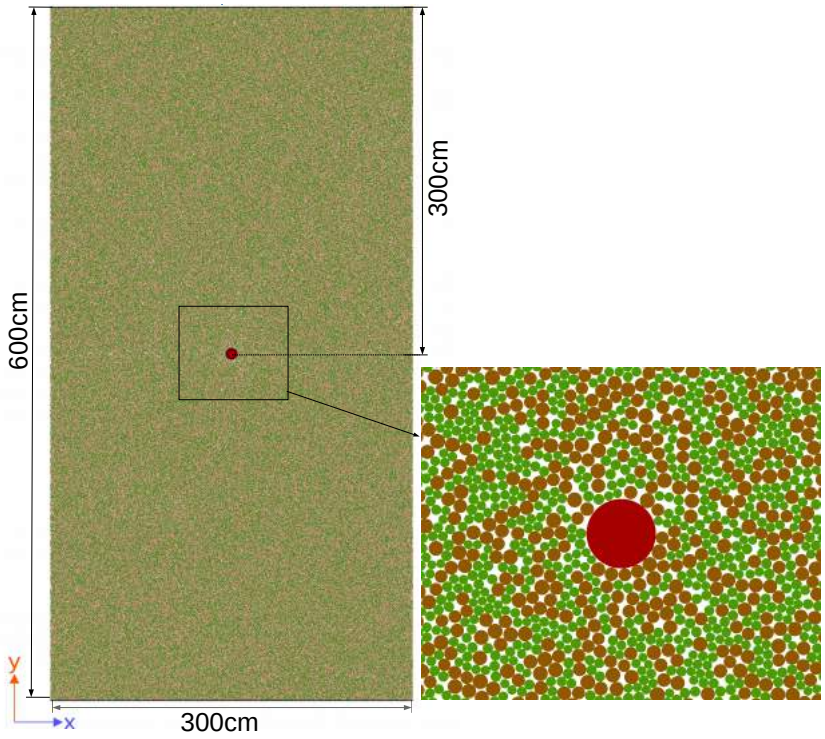

Figure 4.1: One of the initial configuration of our system with an intruder placed at a depth of $h = 300\ cm$. Here, the green colour particles indicate dumbbells and the brown colour is that of discs. At $y = \pm 300$, the system is confined by walls made of glued particles (black) having a diameter of $1\ cm$. Whereas, in the x direction, periodic boundary conditions are applied. Note that the origin is located at the centre of the intruder. A zoomed in image of the region around the intruder is shown to the right side of the intial configuration.

In this work, we employed the discrete element method (DEM) [20] to study the dynamics of a moving intruder and its surroundings at different intruder sizes and at different system properties such as its area fraction and the fraction of dumbbells in it. To generate the initial configuration for a system at $\phi = 0.43$, firstly, we place the intruder of the required size at the origin and then generate particles one by one at random positions inside our system with enclosing walls at $y = \pm 300cm$. During the generation of the particle positions, if the newly created particle overlaps with any previously existing particle or the intruder or the wall, then this new particle is assigned to another randomly generated position using a uniform distribution. This procedure is repeated

untill we achieve the desired area fraction $\phi = 0.43$ (100000 particles). Additionally, to incorporate polydispersity for both dumbbell and spherical particles, their sizes were also generated using a uniform distribution within the bounds of ten percent polydispersity. The system is large enough that the effect of the seed of the random number generator becomes insignificant on our quantification. For a higher area fraction ($\phi = 0.77$ (180000 particles), 0.82 (188000 particles)) we followed the similar procedure as explained before, however initially, the system dimension along the $y-$ direction is kept much larger than actually required. Then, the y dimension is reduced by slowly moving the walls towards each other until the system reaches the required area fraction ϕ while the intruder is fixed at the origin. The system is then allowed to equilibrate till the total kinetic energy (KE) of the particles reaches $KE < 10^{-12} gmcm^2/s^2$. For ensuring that the area fraction is homogeneous throughout the system, the local area fraction is calculated along a grid of $1cm \times 1cm$ to ensure homogeneity within 2%. If the system is not homogeneous, a new system is created. The mean diameter of disk particles is $1cm$, while the dumbbells are constructed using two equally-sized, non-overlapping, and fused disk particles of mean diameter $0.7cm$. This guarantees both disc and dumbbell particles to have equivalent mass on average, while a polydispersity of ten percent avoids crystallization in the system. The density of each particle is set as $\rho = 2\ gm/cm^2$. At time $t = 0$, the intruder is moved at a constant velocity V_i along the positive x-direction for a total distance of 300 cm. Fig. 4.1 shows an initial configuration of one of our simulation systems with the circular intruder having a diameter of $10cm$ placed at a distance of $h = 300cm$ from the top wall.

The simulation technique is explained in chapter 2. It should be noted that as the system is gravityless, only contact forces are considered during the simulation. The various constant and its value used in the simulation are given as $k_n = 2 \times 10^{10} (gm/cm\ s^2)$ and $k_t = 2.456 \times 10^{10} (gm/cm\ s^2)$, while $\gamma_n = \gamma_t = 80000 (cm\ s)^{-1}$. Two coefficient of friction μ (0 and 0.5) were considered in the present study. The timestep is set to $2 \times 10^{-6} s$. The run time for the simulation is calculated and adjusted to the time taken by the intruder to cover a distance of $300cm$ at a given velocity. The position and velocity of a dumbbell is its centre of mass and its centre of mass velocity. The total force and torque on a dumbbell are computed as the sum of the forces and torques on its constituent particles. All the simulations were performed using LAMMPS [21] package, and OVITO [22] was used for post-simulation visualization.

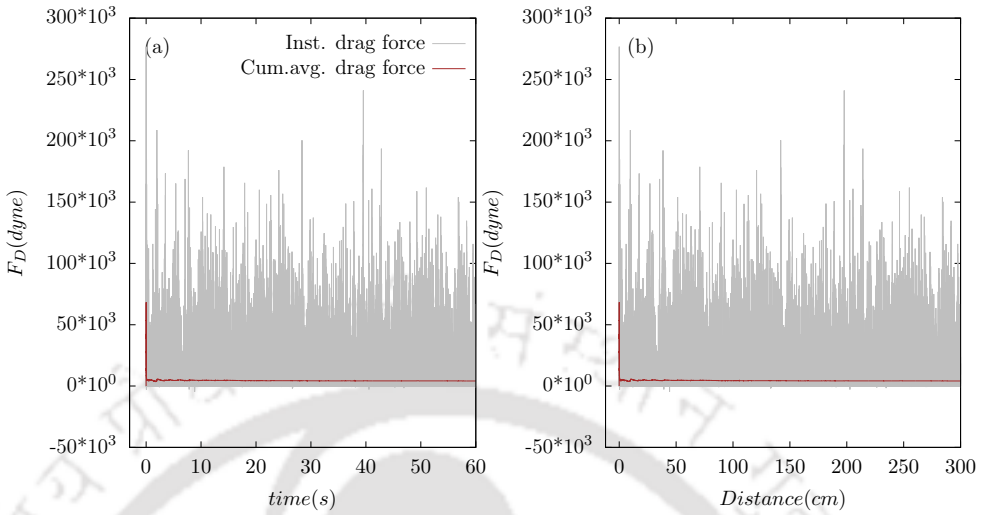

Figure 4.2: The instantaneous drag force on the intruder (grey line) and its cumulative average (brown line) with respect to (a) time (s) and distance/d. Here, the coefficient of friction is $\mu = 0.5$, the intruder velocity $V_i = 10cm/s$, $\phi = 0.82$ and the intruder diameter $D_i = 5cm$

4.3 Results and Discussion

In this section, we will present the numerical results for an intruder translating through a mixture of dumbbells and discs.

4.3.1 Dumbbell fraction

In this subsection, we studied the characteristics of a moving intruder and its surroundings at various mixture concentrations. To this end, we computed the drag force (F_D) and the coordination number (N_c) of the intruder and the stress decline slope (σ_s). When the intruder is moved at time $t = 0$, there is a transient period before it reaches a mean steady state behaviour, i.e., the average of drag force is almost constant with respect to time. In this work, F_D and N_c correspond to their time-averaged values and note that the average doesn't include few values at the beginning of the simulation to avoid initial intermittencies. The total distance the intruder travels is $300d$, therefore, the averaging is done over a distance of $270d$. In figure 4.2, we have shown the instantaneous as well as cumulative average drag force with respect to time, which shows the transient nature of drag force data at the beginning. In this subsection, the area fraction of the system is $\phi = 0.82$, the coefficient of friction is set to $\mu = 0.5$ and the diameter of the intruder

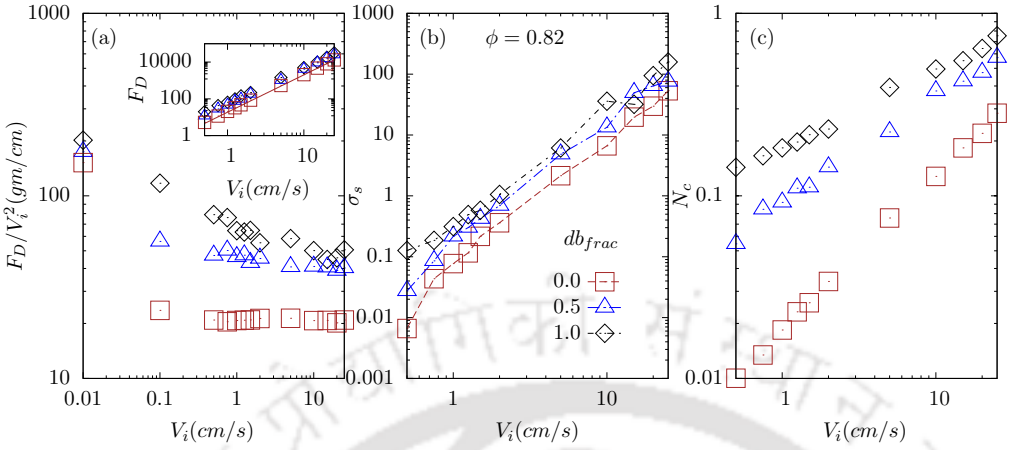

Figure 4.3: (a) The time-averaged drag force F_D normalized by the square of intruder's velocity V_i , (b) the stress decline slope σ_s, and (c) the averaged number of particles in contact (N_c) as a function of intruder's velocity V_i for the fractions of dumbbells (db_{frac}) = 0, 0.5 and 1. The area fraction is $\phi = 0.82$, and the coefficient of friction is $\mu = 0.5$ and the diameter of the intruder is $D_i = 5\ cm$.

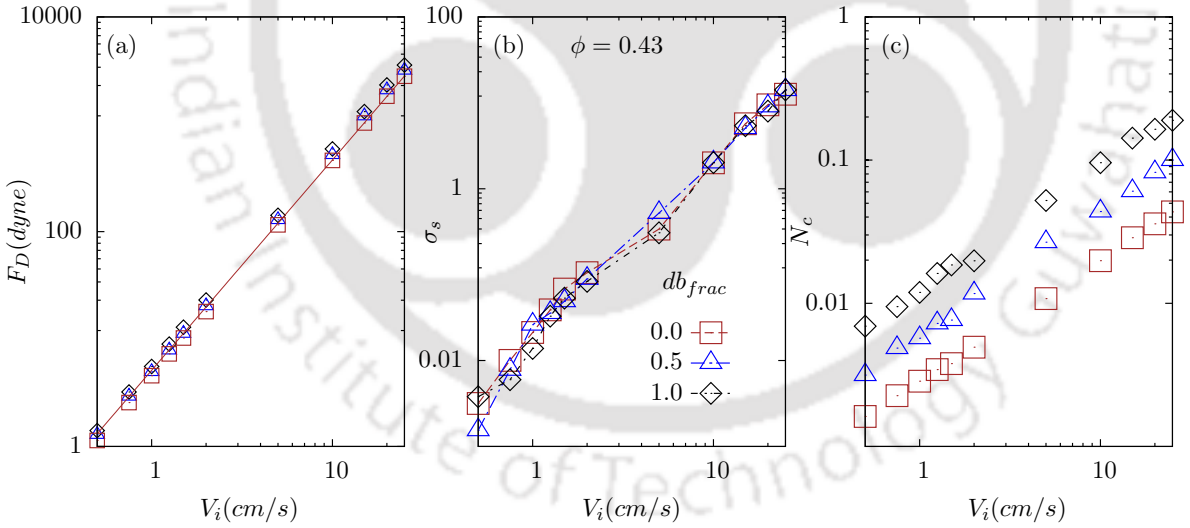

Figure 4.4: (a) The time-averaged drag force F_D as a function of intruder's velocity V_i , (b) the stress decline slope (σ_s) and (c) the averaged number of particles in contact (N_c) as a function of intruder's velocity V_i for the fractions of dumbbells (db_{frac}) = 0, 0.5 and 1. The area fraction is $\phi = 0.43$ and the coefficient of friction is $\mu = 0.5$ and the diameter of the intruder is $D_i = 5\ cm$.

is taken as $D_i = 5\ cm$. At all fractions of dumbbells db_{frac}, the drag force F_D increases quadratically with an increase in the intruder's velocity V_i (see Fig 4.3a). A similar result

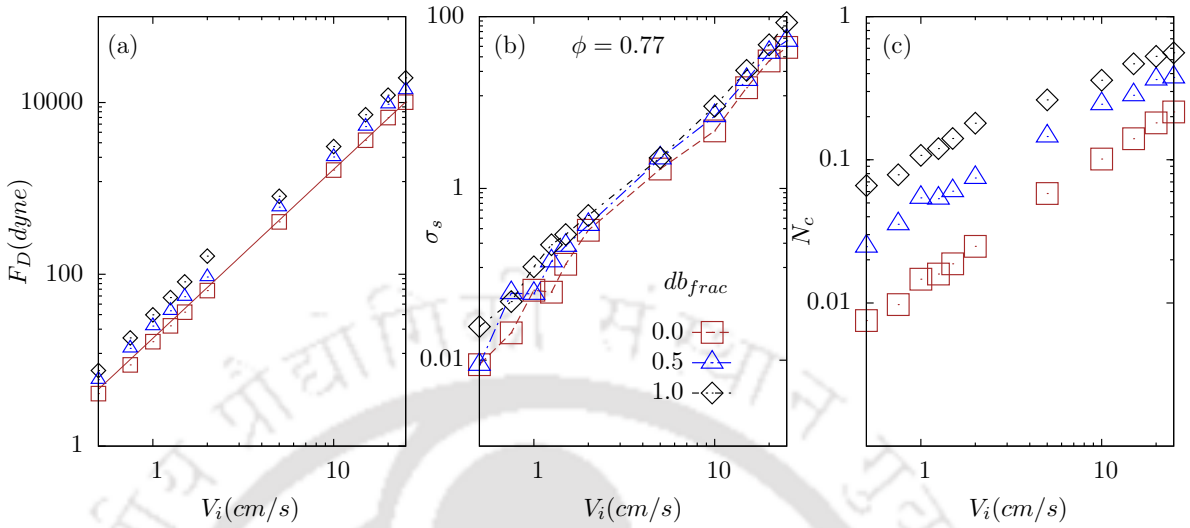

Figure 4.5: (a) The time-averaged drag force F_D as a function of intruder's velocity V_i, (b) the stress decline slope (σ_s) and (c) the averaged number of particles in contact (N_c) as a function of intruder's velocity V_i for the fractions of dumbbells (db_{frac}) = 0, 0.5 and 1. The area fraction is $\phi = 0.77$ and the coefficient of friction is $\mu = 0.5$ and the diameter of the intruder is $D_i = 5\ cm$.

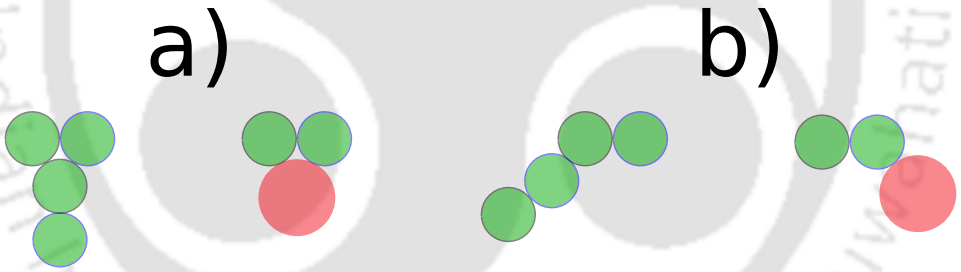

Figure 4.6: The two possible type of contacts in a dumbbell-dumbbell or dumbbell-disc interaction. a) The two parts of a dumbbell are simultaneously in contact with a disc or one part of another dumbbell. b) Only one part of a dumbbell is in contact with a disc or one part of another dumbbell. Here, the green ones represent dumbbells and the pink ones that of discs.

has been noticed for an intruder placed inside a two-dimensional system of spherical granules [23]. However, at very low intruder's velocity ($V_i \leq 0.01$), the drag force doesn't scale as V_i^2 for all the fractions of dumbbells. This is because, in a quasi-static regime($V_i \leq 0.01$), the drag force is weakly dependent on the intruder's velocity. In this regime, the drag mainly depends on the heterogeneous distribution of stresses in the granular media [4]. As the intruder traverse granular media, a dense structure of particles evolve progressively in front of the intruder and then gets saturated [14]. This structure comprises particles that are interconnected through a network of contacts or force chains

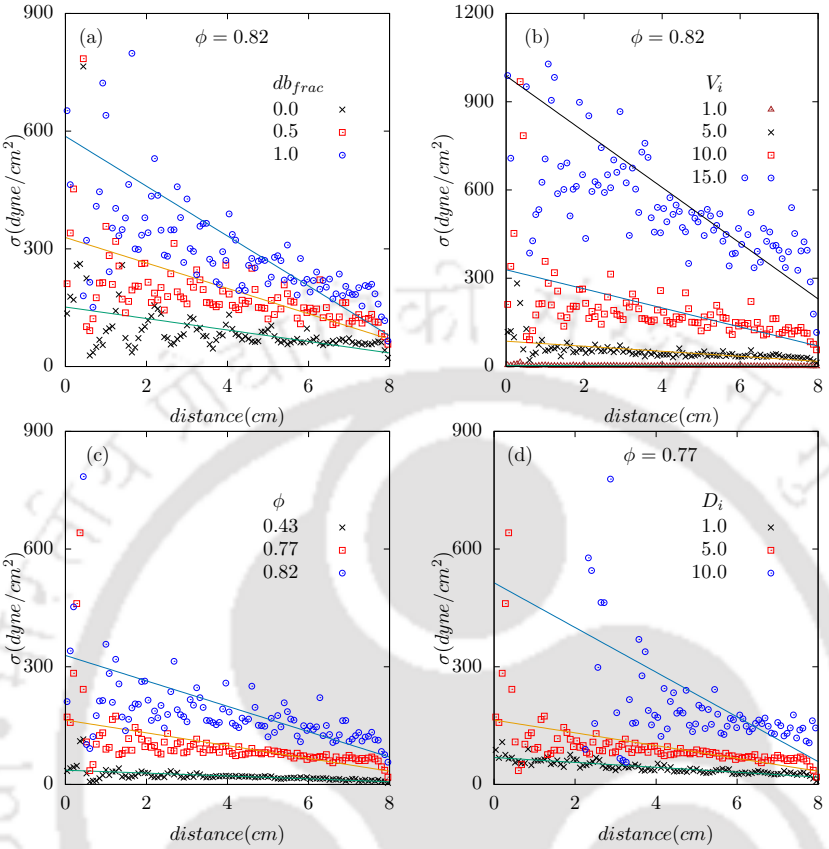

Figure 4.7: The magnitude of stress σ as a function of distance infront of the intruder surface (a) for different db_{frac} and ϕ 0.82 , (b) for different intruder velocity V_i with system having db_{frac} = 0.5 and ϕ 0.82, (c) for $V_i = 10cm/s$ at different area fraction ϕ with system having $db_{frac} = 0.5$ and (d) for different intruder diameter (D_i) with $\phi = 0.77$. The coefficient of friction is $\mu = 0.5$ in all the cases and the intruder diameter $D_i = 5cm$ is for system in plots (a), (b,) and (c).

and it is accompanied by the cyclic evolution and the breakage of force chains. The drag force on the intruder moving through a system of spherical particles is mainly due to the alternating evolution and buckling of force chains in the material and the inter-particle friction [24]. At the same coefficient of friction, the drag force increases with an increase in the fraction of dumbbells db_{frac} (see inset of Fig 4.3a). This result can be attributed to a decrease in the frequency of force-chain buckling events with an increase in db_{frac}. This is due to an increase in the mutual resistance to the relative motion of the particles in contact, particularly the "a" type of contacts as shown in figure 4.6. Two types of

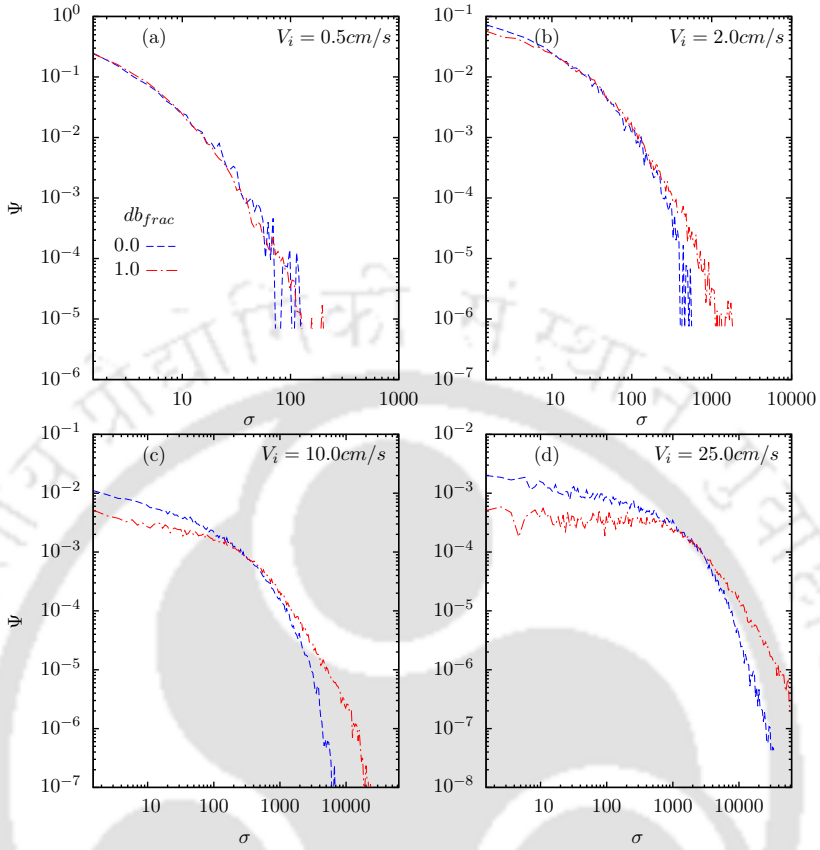

Figure 4.8: The probability distribution function Ψ of the stress σ experienced by the intruder for four different velocities of the intruder V_i (a) 0.5 cm/s (b)2 cm/s (c) 10 cm/s and (25 cm/s). Here, $db_{frac} = 0$, and 1 are the fraction of dumbbells in the system.

contacts are possible between two particles if at least one of those is a dumbbell. In the first type, both the parts of a dumbbell are simultaneously in contact with either disc or one part of another dumbbell (figure 4.6 a). Whereas in the second type, only one part of a dumbbell is in contact with a disc or one part of another dumbbell (figure 4.6 b). As the fraction of dumbbells increases, the chances of occurrence of the "a" type of contacts increases, resulting in an increase in the interlocking type of phenomena. This yields a decrease in the frequency of buckling events in the structure in front of the intruder or in other words an increase in the drag force on the intruder. After analysing the drag on the intruder, we studied its effect on the particles in front of it in terms of the magnitude of the stress decline slope σ_s. In a plot of the stress vs the distance from the intruder (shown in figure 4.6), σ_s is the slope of the line of best fit. The stress tensor σ_{ab} on i^{th} particle due to its N_p pair-wise interactions is calculated as $\sigma_{ab} = \frac{1}{2\times A}\Sigma_{j=1}^{N_p}(r_{i_a}F_{i_b} + r_{j_a}F_{j_b})$ where

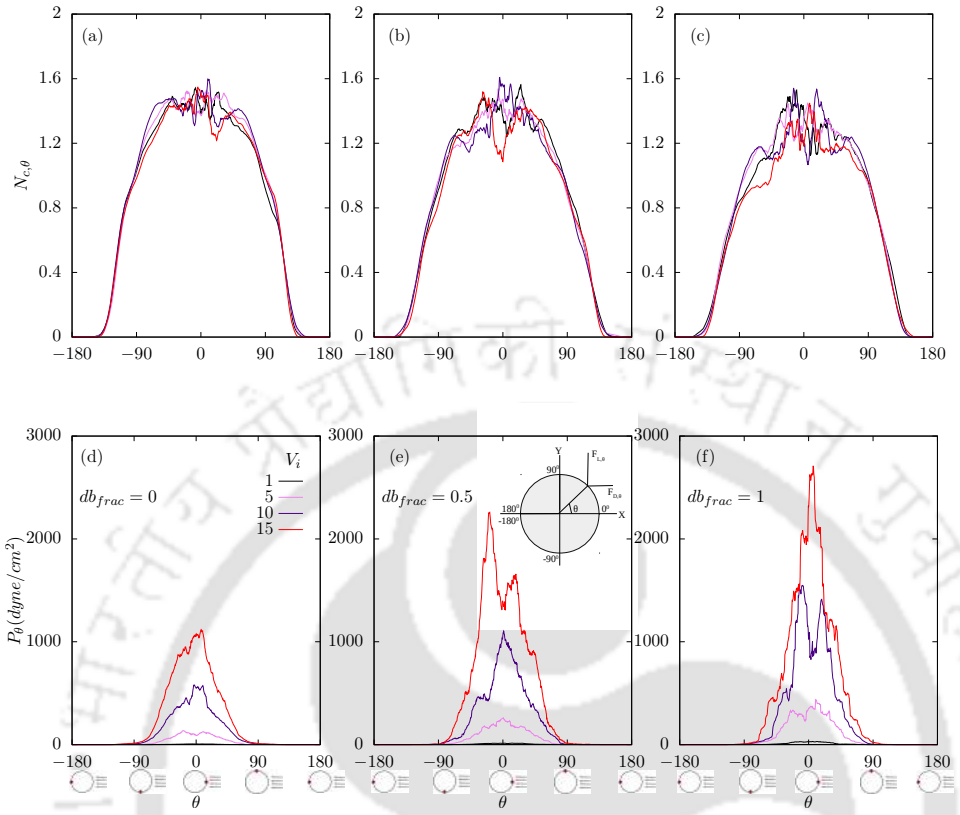

Figure 4.9: The average number of particles in contact N_{c_θ} as a function of angular position (θ) for the fraction of dumbbells db_{frac} = a) 0.0, b) 0.5 and c) 1.0. The average pressure P_θ as a function of angular position at different intruder velocities V_i for the fraction of dumbbells db_{frac} = d) 0.0, e) 0.5 and f) 1.0. The coefficient of friction is $\mu = 0.5$, the area fraction is $\phi = 0.82$, and the inset in (e) displays how the angular positions are calcuated around the intruder surface.

a and b take on x and y values to produce the components of the stress tensor. Here, r_{i_a} is the relative position of the i^{th} particle to the geometric center of the interacting particles, F is the force due to the pair-wise interaction, and A is the area of the i^{th} particle. The stress is calculated as $\sigma = -\frac{1}{2}(\sigma_{xx} + \sigma_{yy})$. Usually, the stress is maximum in the region close to the intruder. The distance between the intruder surface and the region at which the stress is equal to the average stress of the system doesn't vary significantly due to a change in the properties of the system or the intruder. The reason for this is the absence of gravity. A higher σ_s indicates a higher stress near the intruder surface and a rapid decrease in stress as a function of the distance from the intruder surface. As the intruder velocity increases, σ_s increases because the intruder exerts more stress on the particles close to it. Moreover, σ_s increases with an increase in the fraction of dumbbells. This behaviour can be attributed to the interlocking type of phenomena that occurs with

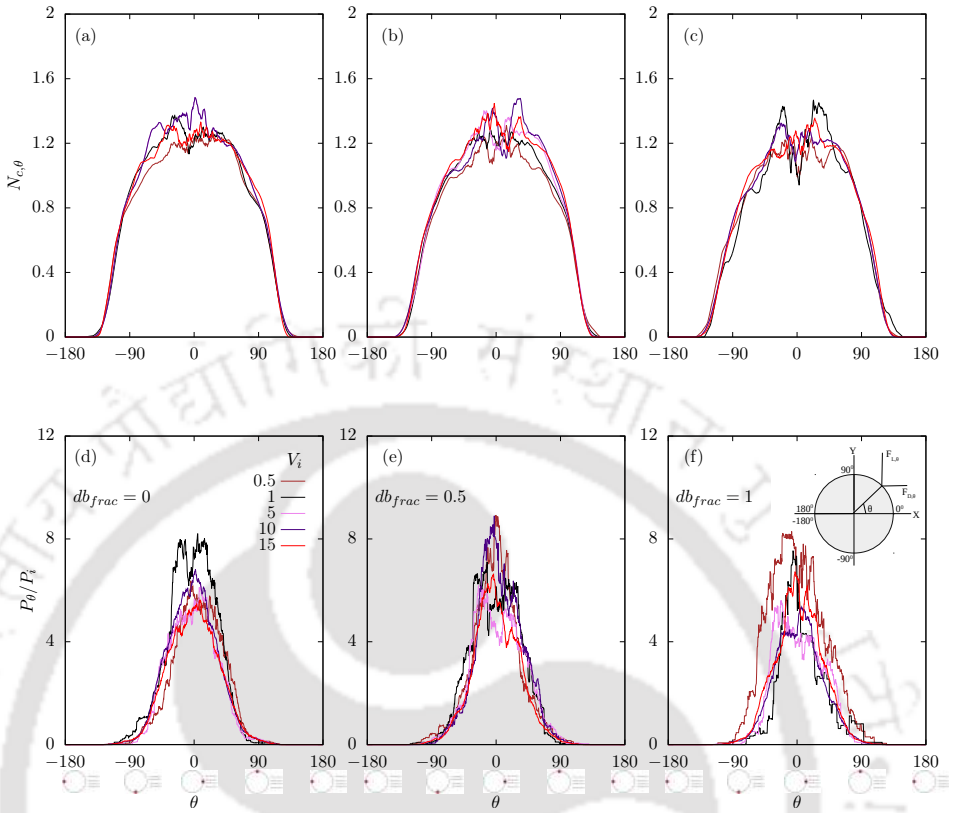

Figure 4.10: The average number of particles in contact N_{c_θ} as a function of angular position (θ) for the fraction of dumbbells db_{frac} = a) 0.0, b) 0.5 and c) 1.0. The average normalised pressure P_{theta}/P_i as a function of angular position at different intruder velocities V_i for the fraction of dumbbells db_{frac} = d) 0.0, e) 0.5 and f) 1.0. The coefficient of friction is $\mu = 0.0$, the area fraction is $\phi = 0.82$ and the inset in (f) displays how the angular positions are calcuated and P_i denotes the pressure experienced by the intruder.

the dumbbell particles which results in a higher stress close to the intruder. The drag force in the granular media arises from the particles in contact and if the average force exerted by each contacting particle is constant, then more the number of contacts greater the drag on the intruder. The increase in the number of contacts N_c with an increase in the intruder's velocity V_i as noticed in figure 4.3c is consistent with the drag force result. A similar result was observed previously for a system of disc particles [25]. As the fraction of dumbbells increases, the number of contacts N_c increases. This is due to a decrease in the frequency of buckling events in the region in front of the intruder because of the interlocking type of phenomena experienced by the dumbbells. We have also shown the similar analysis for system with $\phi = 0.43$ and 0.77 in figure 4.3 and 4.4.

The probability distribution function (PDF) of stress experienced by the intruder

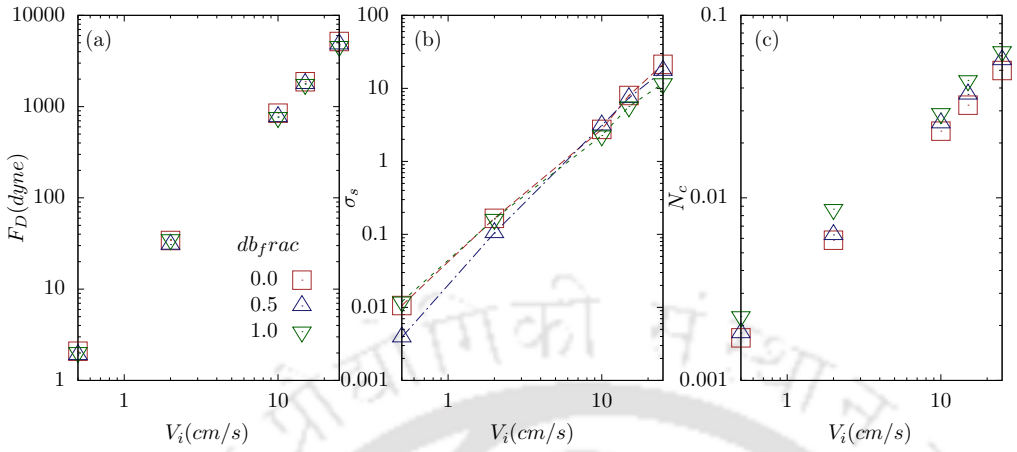

Figure 4.11: (a) The time-averaged drag force F_D, (b) the stress decline slope σ_s, and (c) the averaged number of particles in contact (N_c) as a function of intruder's velocity V_i for the fractions of dumbbells (db_{frac}) = 0, 0.5 and 1. The coefficient of friction is $\mu = 0.0$, the area fraction is $\phi = 0.82$, and the diameter of the intruder is $D_i = 5\ cm$.

at different fractions of dumbbells is studied to understand the effect of interlocking potential of dumbbells on the intruder (figure 4.8). Irrespective of the intruder's velocity, the stress is noticed to be higher in the case of dumbbells as compared to that of discs. This further justifies our claim regarding the interlocking type of phenomena noticed in a system involving dumbbell particles. The drag force on the intruder is due to the particle contacts around its entire periphery. Hence, we analysed the number of contacts and their relative stress contributions at different angular positions on the intruder surface. In this regard, we displayed the stress distributions around it in figure 4.9 for $\phi = 0.82$ and $\mu = 0.5$. Note that the angular positions θ correspond to the region around the intruder and they are computed concerning the centre of the intruder. In both the distributions, the angular positions ranging from 0^o to 180^o correspond to the region around the top half of the intruder whereas, the ones from 0^o to -180^o correspond to the lower half of the intruder where 0^o is in front of the intruder and $\pm 180^o$ is at the rear end as shown in the inset of figure 4.9f. As the intruder moves through the granular media, a wake is formed behind it for all the fractions of dumbbells which can be noticed in $N_{c_\theta} = 0$ at $90^o < \theta < 180^o$ and $-180^o < \theta < -90^o$ in figure 4.9 a,b,c. Potiguar and Ding[26] reported the formation of the wake behind the intruder at high intruder velocities. However, in our work, we noticed the formation of wake even at velocities of the intruder as low as $V_i = 0.5$ and for all fractions of dumbbells because of our system being a gravityless

one. The particles colliding with the intruder are mainly confined to the front part of the intruder in the sense: $-90^o < \theta < 0^o$ and $0^o < \theta < 90^o$. The number of contacts at different angular positions increases with an increase in either the intruder's velocity or the fraction of dumbbells. This result is coherent with that of the average number of contacts as a function of the intruder's velocity as shown in figure 4.3c. The averaged stress (P_θ) in the region around the intruder is confined to the angular positions between 0^o to $\pm 90^o$ because particles lying only in this region collide with the intruder as noticed in the N_{c_θ}. At different θ, the averaged stress at each angular position increases with an increase in the fraction of dumbbells. This result further justifies our claim that with an increase in the fraction of dumbbells there is an increase in drag in a frictional system. Apart from the inter-particle friction, the geometry of the particles infront of the intruder also contribute to an increase in the stress or the drag force [11]. Whereas for the frictionless system i.e. $\mu = 0.0$ (shown in figure 4.9) the magnitude of drag force experience around the intruder surface does not vary much even with an increase in the fraction of dumbbells. To understand the sole effect of the geometry of the particles on the drag force experienced by the intruder, we studied frictionless systems [11]at different fractions of dumbbells in the next subsection.

4.3.2 Absence of frictional forces

In this subsection, the coefficient of friction is set to $\mu = 0.0$. The area fraction of the system is $\phi = 0.82$ and the diameter of the intruder is taken as $D_i = 5\ cm$. The drag force increases with an increase in the fraction of dumbbells in a frictional system, as seen in the inset of figure 4.3 a. Surprisingly, in a frictionless system, we noticed an anomalous behaviour in the intruder's drag (figure 4.11 a), in a sense, the drag is almost independent of the fraction of dumbbells. The tangential forces between the particles are primarily responsible for the interlocking type of phenomena exhibited by the dumbbells. In a frictionless system, the tangential forces are absent and hence the ability of the dumbbells to show interlocking type of phenomena is negligible. Therefore, in such systems, the drag experienced by the intruder is not significantly affected by the fraction of dumbbells. This result reveals that the effect of the particle geometry on the drag dynamics of the intruder can be witnessed only in a frictional system. To this end, we point out that it is difficult to isolate the sole effect of the geometry of the particles on the intruder's drag as the geometry and the frictional forces between

the particles seems to be inter-related [11]. In addition, the drag force experienced by the intruder in a frictional system is 3 ($db_{frac} = 0.0$) to 9 (db_{frac}) = 1.0) times higher than that of the frictionless system. This can be attributed to the size of the cluster of particles infront of the intruder. In the sense, the cluster size is smaller for a frictionless system as compared to that of the frictional system. The tangential forces which are mainly responsible for the evolution of clusters infront of the intruder are absent in a frictionless system leading to smaller cluster size. It was previously noticed that the friction between the contacting particles increases the inherent stability and formation of strong force chains [27] thus supporting our claim regarding the cluster size. The stress decline slope varies insignificantly with the fraction of dumbbells (figure 4.11 b) at all intruder velocities. This is due to the minimal effect of interlocking type of phenomena among dumbbells in a frictionless system, as explained above. Due to the same reason, the average number of contacts of the intruder remains almost the same for all the fraction of dumbbells (figure 4.11 c), unlike a significant difference that has been noticed in the case of a frictional system (figure 4.3c). The results obtained from the frictional and the frictionless system reveal that the frictional interactions between the particles play a major role in the drag dynamics of an intruder. One of the major factors which determine the number of frictional interactions is the area fraction of the system. In the next subsection, we will address the effect of the area fraction of the system on the intruder's drag.

4.3.3 Area fraction

In this subsection, we analysed how the dynamics of an intruder and its surroundings is affected by the area fraction of the system comprising of dumbbells and discs. The area fraction (ϕ) of the system is computed as:

$$\phi = \frac{A_g}{A_s - A_i} \tag{4.1}$$

Here, A_g is the total area occupied by granular particles, A_s is the area of our system, and A_i is the area of the intruder. The area fraction of the system ϕ = 0.43, 0.77, and 0.82 is achieved by using 100000, 180000, and 188000 granular particles, respectively, while fixing the system dimensions same for all the cases. Note that in this subsection, the fraction of dumbbells is $db_{frac} = 0.5$, the coefficient of friction is set to $\mu = 0.5$ and the diameter of the intruder is taken as $D_i = 5\ cm$. The frictional forces come into play

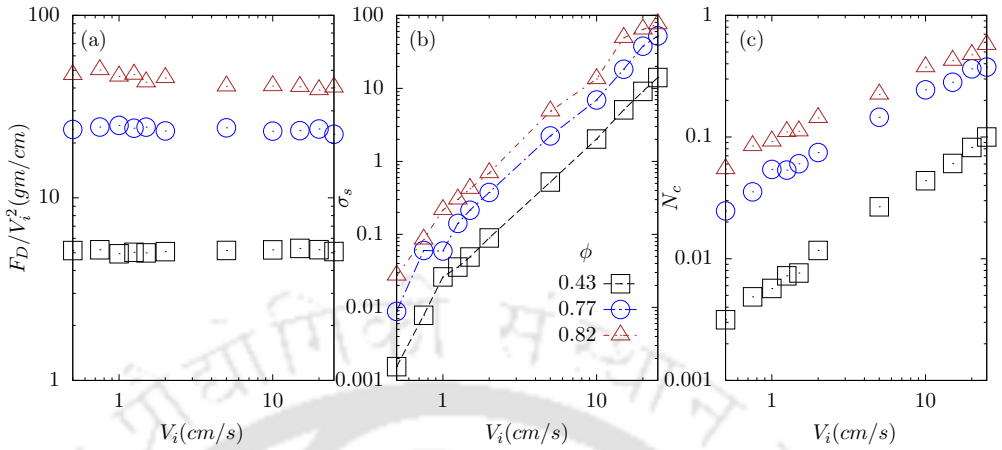

Figure 4.12: (a) The time-averaged drag force F_D, (b) the stress decline slope σ_s, and (c) the number of contacts (N_c) as a function of the intruder's velocity V_i for systems with area fraction of (ϕ) = 0.43, 0.77 and 0.82. The fraction of dumbbells (db_{frac}) is 0.5, the diameter of the intruder (D_i) is 5 cm, and the coefficient of friction (μ) is 0.5.

when two particles interact with each other in a granular medium. As it may be expected, a system with a higher area fraction will have a larger number of frictional interactions among the particles. Apart from an increase in the frictional interactions, a denser granular system results in the evolution of stronger force chain networks that offer greater resistance to the movement of an object through the granular medium[28–30]. These could be the reasons for an increase in the drag force with an increase in the area fraction for all the fractions of dumbbells (figure 4.12 a). The drag force on the intruder for $\phi = 0.82$ is ten times more than that it experiences in a system with $\phi = 0.43$. So, one can infer that, in a denser system, the intruder exerts greater stress on the particles infront of it. Consequently, the stress decline slope increases with an increase in the area fraction (figure 4.12b). Interestingly, the drag force on the intruder is noticed to scale as the square of its velocity V_i irrespective of the area fraction of the system. Moreover, the number of contacts of the intruder increases with an increase in the area fraction (figure 4.12c), which results in higher stress or, in other words, a higher drag force experienced by the intruder.

4.3.4 Diameter of the intruder

The effect of various parameters of the system on the drag dynamics of the intruder has been discussed in the previous subsections. In this subsection, we are going to elucidate

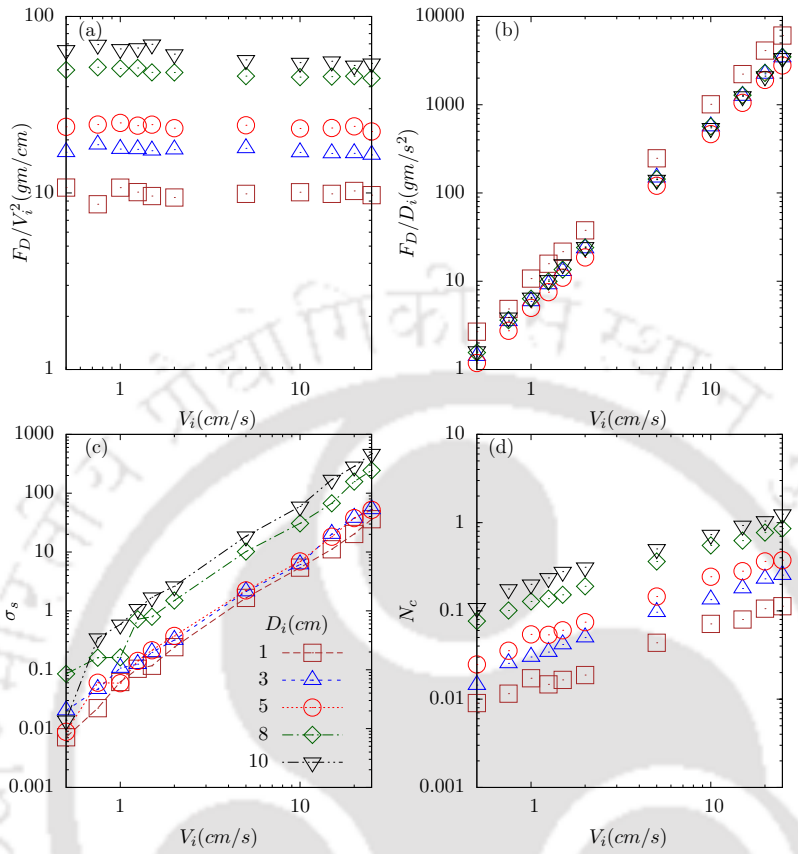

Figure 4.13: (a) The time-averaged drag force F_D, (b) the drag force normalised by the intruder's diameter (F_D/D_i), (c) the stress decline slope σ_s, and (d) the number of particle contacts (N_c) as a function of the intruder's velocity V_i for different diameters of the intruder (D_i). The fraction of dumbbells (db_{frac}) is 0.5, the area fraction of the system (ϕ) is 0.77, and the coefficient of friction (μ) is 0.5.

the drag dependence on the intruder's geometry. To this end, we analysed the system for five different diameters of the intruder, starting from the size of the disc particle and ranging over a magnitude ten times the particle diameter. For all the cases, the fraction of dumbbells is $db_{frac} = 0.5$, the area fraction of the system is set to $\phi = 0.77$, and the coefficient of friction is $\mu = 0.5$. The drag force increases as the diameter of the intruder D_i increases, as shown in figure 4.13a. This is due to an increase in the size of the structure of particles in front of the intruder with an increase in D_i. The reason for this is as D_i increases, the surface of the intruder available for the particles in front of it to form a structure increases, which increases the size of the structure.

Similar behaviour of increase in the drag force experienced by the intruder with an increase in the intruder's diameter was noticed in both the confined [10] as well as the non-confined [4, 31] granular media. The drag force is noticed to scale as the square of the intruder's velocity V_i^2 (see figure 4.13a). Interestingly, when we plot the drag force normalised by the intruder's diameter as a function of velocity V_i (figure 4.13b), all the data collapse onto a single curve. This indicates that the drag force scales as the diameter of the intruder. Figure 4.13c shows that the stress decline slope increases as the intruder diameter increases. This result suggests that the stress experienced by the particles close to the intruder surface increases with an increase in intruder diameter (D_i) due to an increase in drag force. However, the distance from the intruder at which the stress is equal to the average stress of the system doesn't vary significantly with D_i. Therefore, the stress decline slope increases with an increase in D_i. An increase in the intruder's diameter increases the surface area available for the surrounding particles to get in contact with it. This yields an increase in the number of contacts with an increase in the intruder's diameter (figure 4.13d).

4.3.5 Mean flow fields

We have generated time-averaged flow fields by using discrete microscopic data like velocities, positions, stress etc,. of each of the particles in a designated region around the intruder. The Gaussian coarse-graining function, as implemented by Glasser and Goldhirsch[32], is used to calculate the parameters at various spatial locations. At a spatial location p with a position vector $\boldsymbol{r_p}$ and at an arbitrary time t the area fraction $\phi(t)$, velocity $v(t)$, stress tensor $\boldsymbol{\sigma_{ij(t)}}$ and the pressure $P(t)$ are computed using Gaussian coarse-graining technique, as suggested by Glasser and Goldhirsch[32]:

$$\phi(t) = \left[\sum_{i=1}^{n} \frac{\rho\pi d_i^2}{4} \mathcal{W}(\boldsymbol{r_p} - \boldsymbol{r_i(t)})\right]/\rho \tag{4.2}$$

$$\boldsymbol{v}(t) = \left[\sum_{i=1}^{n} \frac{\rho\pi d_i^2}{4} \boldsymbol{v_i} \mathcal{W}(\boldsymbol{r_p} - \boldsymbol{r_i(t)})\right]/\rho\phi \tag{4.3}$$

$$\boldsymbol{\sigma_{ij}}(t) = \sum_{i=1}^{n}\sum_{j=i+1}^{n} (\boldsymbol{F^{ij}r_{ij}}) \int_{s=0}^{1} \mathcal{W}(\boldsymbol{r_p} - \boldsymbol{r_i(t)} + s\boldsymbol{r_{ij}})ds \tag{4.4}$$

$$P(t) = \frac{-tr(\sigma_{ij}(t))}{2} \tag{4.5}$$

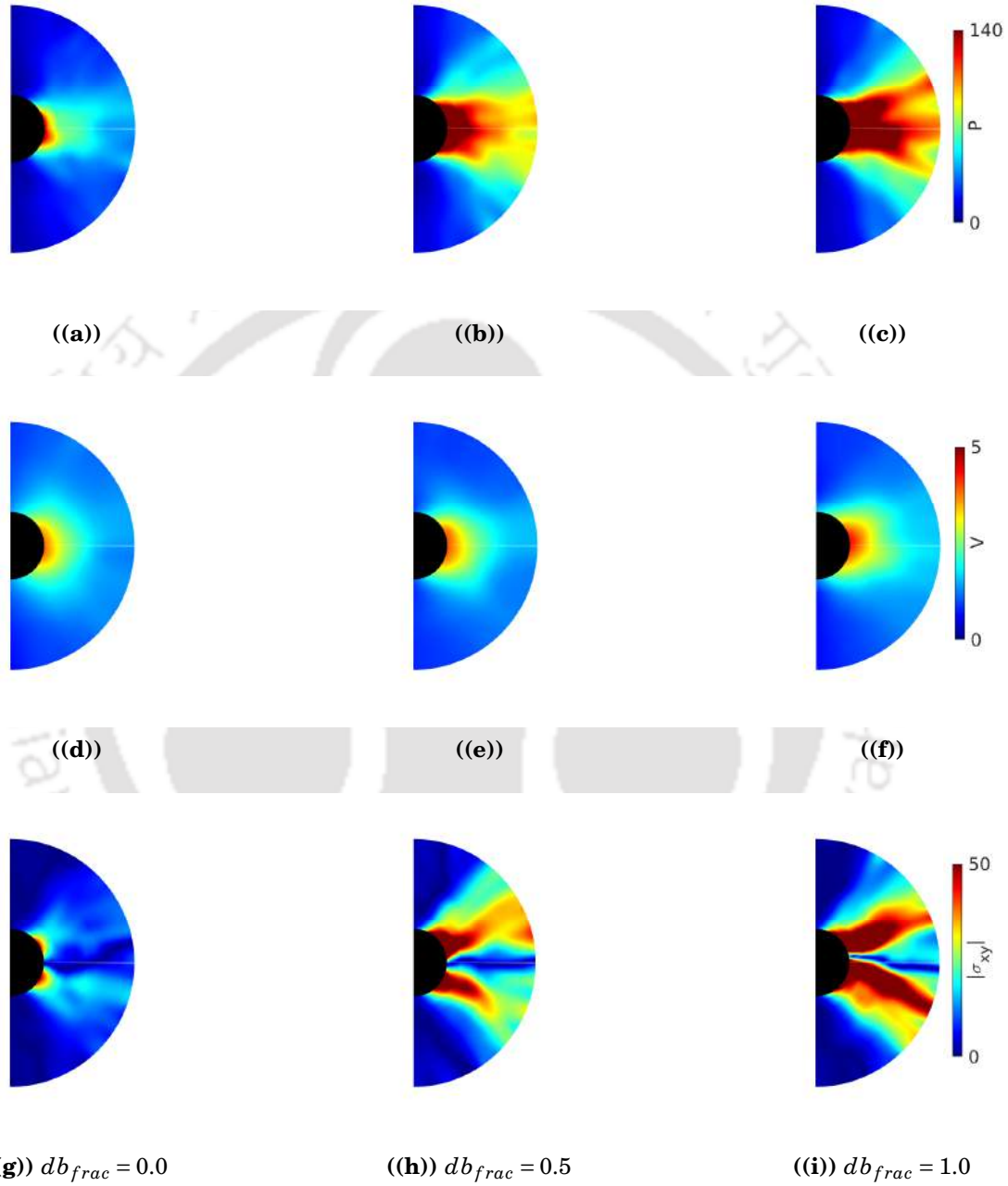

((a)) ((b)) ((c))

((d)) ((e)) ((f))

((g)) $db_{frac} = 0.0$ ((h)) $db_{frac} = 0.5$ ((i)) $db_{frac} = 1.0$

Figure 4.14: The time-averaged flow fields for depicting pressure $P(dyne/cm^2)$, velocity $V(cm/s)$ and shear stress $|\sigma_{xy}|(dyne/cm^2)$ infront of the intruder for different fractions of dumbbells (db_frac): (a), (d), (g) 0.0, (b) (e), (h) 0.5 and (c), (f), (i) 1.0. The modulus of σ_{xy} is basically the magnitude of shear stress. The diameter of the intruder is $D_i = 5cm$, $V_i = 5cm/s$, the coefficient of friction $\mu = 0.5$, and the area fraction (ϕ) of the system is 0.82.

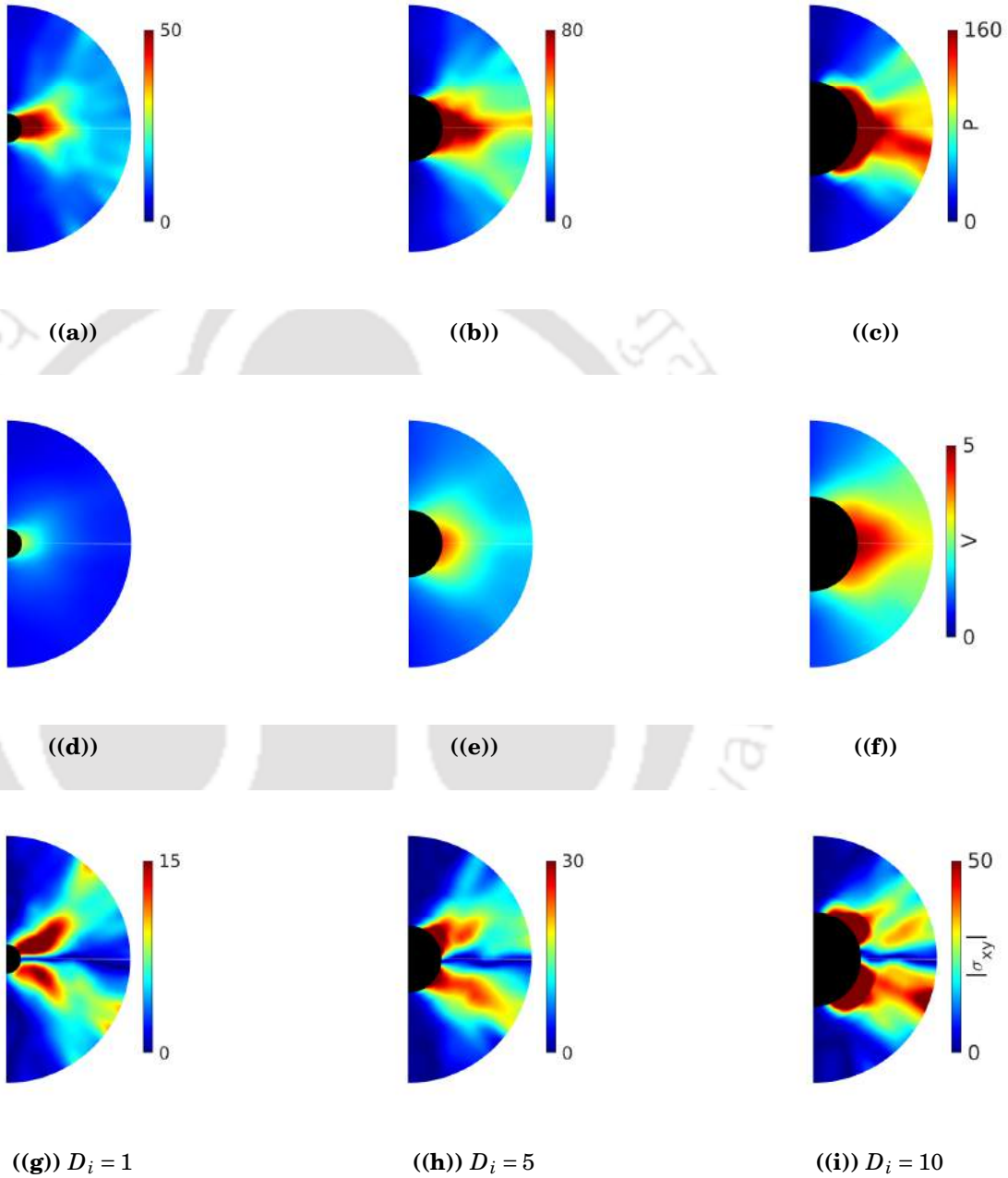

Figure 4.15: The time-averaged flow fields for depicting pressure $P(dyne/cm^2)$, velocity $V(cm/s)$ and shear stress $|\sigma_{xy}|(dyne/cm^2)$ infront of the intruder for different intruder diameter (D_i): (a), (d), (g) 1cm, (b) (e), (h) 5cm and (c), (f), (i) 10cm. The velocity of the intruder is $V_i = 5cm/s$, $\mu = 0.5$, $\phi = 0.77$, and the fraction of dumbbell (db_{frac}) in the system is 0.5.

$$\mathcal{W}(\boldsymbol{r}) = \frac{1}{\pi w^2} e^{-\boldsymbol{r}^2/w^2} \tag{4.6}$$

Here, $\mathcal{W}(\boldsymbol{r})$ is the coarse-graining function, ρ, d_i and $\boldsymbol{r_i(t)}$ are the density, diameter and the position vector of the particle i. $\boldsymbol{F^{ij}}$ is the force on the particle i due to particle j and $\boldsymbol{r_{ij}}$ is a vector in the direction of line joining the centres of two particles i and j. Moreover, $w = 1.0$ and $\mathcal{W}(\boldsymbol{r_p - r_i}) = 0$ if $|\boldsymbol{r_p - r_i}| > 3w$ and $\phi, \boldsymbol{v}$ and P are the time-averaged area fraction, velocity and pressure. The flow fields displayed in the results have been constructed by averaging particles within $15cm$($15 \times d$) from the centre of the intruder over 10000 frames (d being the average particle size). The system size, however, is much bigger than this region considered. Changes in the granular particles induced by the motion of the intruder occur locally within this distance, and these results are shown to highlight the changes that occur locally near the intruder. The system size is large enough that the parameters are independent of the system size considered, and are also independent of any wall/periodic boundary effect. The reason for displaying only the region in front of the intruder is because a wake is developed behind the intruder and it remains as it is until the end of simulation since our system is a gravityless one.

Figure 4.13 a, b and c illustrates the time-averaged pressure fields at the fraction of dumbbells db_{frac}= 0.0, 0.5 and 1.0. At all the fractions of dumbbells, the pressure is maximum near the front surface of the intruder. Moreover, a high-stress zone (the regions of red colour) is noticed infront of the intruder due to the formation of a cluster of particles as we have explained earlier. The pressure decreases as the distance from the intruder's front surface increases. The reason for this behaviour is the particles contacting the cluster slips away instead of sticking to it at larger distances from the intruder. Figure 4.13 d, e and f shows the velocity V fields for db_{frac} = 0.0, 0.5 and 1.0. The zones of red colour infront of the intruder are noticed in velocity fields as well which further confirms the presence of the cluster. Moreover, the velocities of particles infront of the intruder increases with an increase in the fraction of dumbbells. This can be attributed to an increase in the interlocking type of phenomena where a certain type of particle contacts (figure 4.6) in dumbbells resist their relative motion. Figure 4.13 (g) to (i) display the mean flow fields of shear stress $|\sigma_{xy}|$ for different fractions of dumbbells. Here $|\sigma_{xy}|$ is the magnitude of shear stress. The particles whose y position is almost equal to that of the intruder's y position does not detour around it, instead, they move ahead along with it. This results in the absence of shear stress at $y = 0.0$. Due to

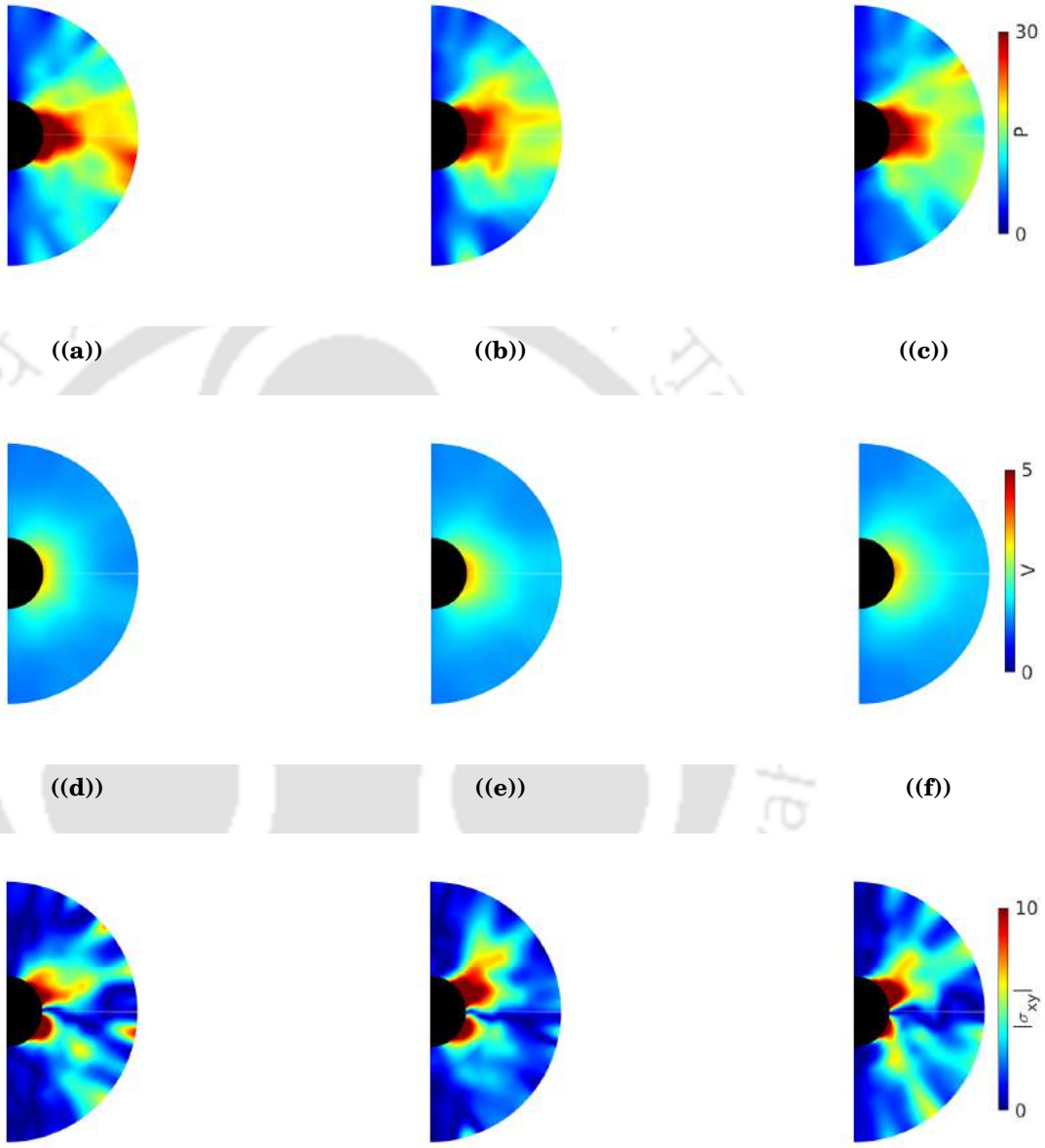

Figure 4.16: The time-averaged flow fields for depicting pressure $P(dyne/cm^2)$, velocity $V(cm/s)$ and shear stress $|\sigma_{xy}|(dyne/cm^2)$ infront of the intruder for different fractions of dumbbells(db_frac): (a), (d), (g) 0.0, (b) (e), (h) 0.5 and (c), (f), (i) 1.0. The modulus of σ_{xy} is basically the positive value (or absolute value) of shear stress. The velocity of the intruder is $V_i = 5\ cm/s$, the coefficcient of friction $\mu = 0.0$, and the area fraction (a_{frac}) of the system is 0.82.

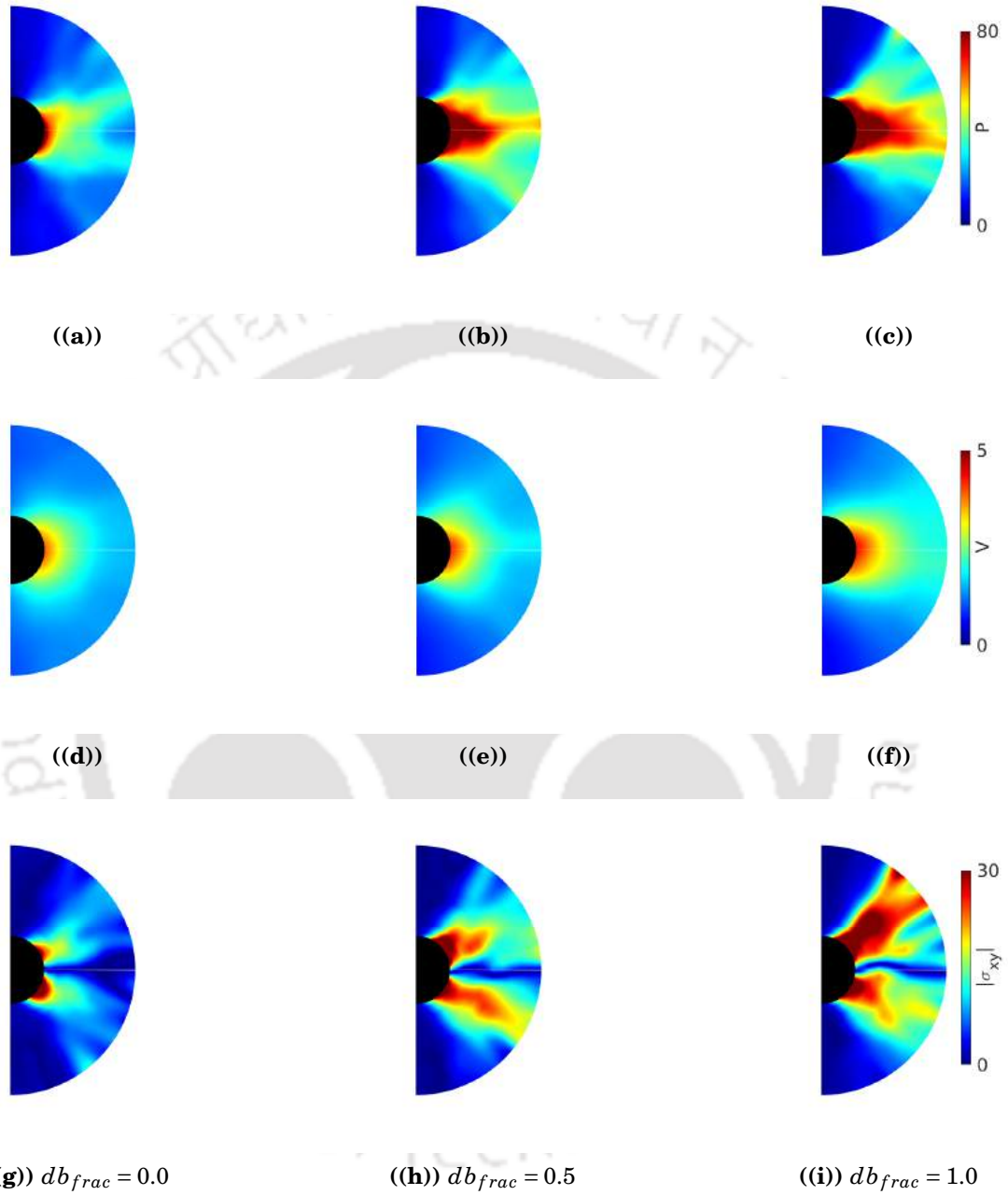

Figure 4.17: The time-averaged flow fields for depicting pressure $P(dyne/cm^2)$, velocity $V(cm/s)$ and shear stress $|\sigma_{xy}|(dyne/cm^2)$ infront of the intruder ($D_i = 5cm$) for different fractions of dumbbells (db_{frac}): (a), (d), (g) 0.0, (b) (e), (h) 0.5 and (c), (f), (i) 1.0. The velocity of the intruder is $V_i = 5\ cm/s$, $\mu = 0.5$ and the area fraction (ϕ) of the system is 0.77.

the movement of the intruder, the particles near the front surface of it, other than the ones mentioned above, are impelled to detour around it. This creates a relative motion

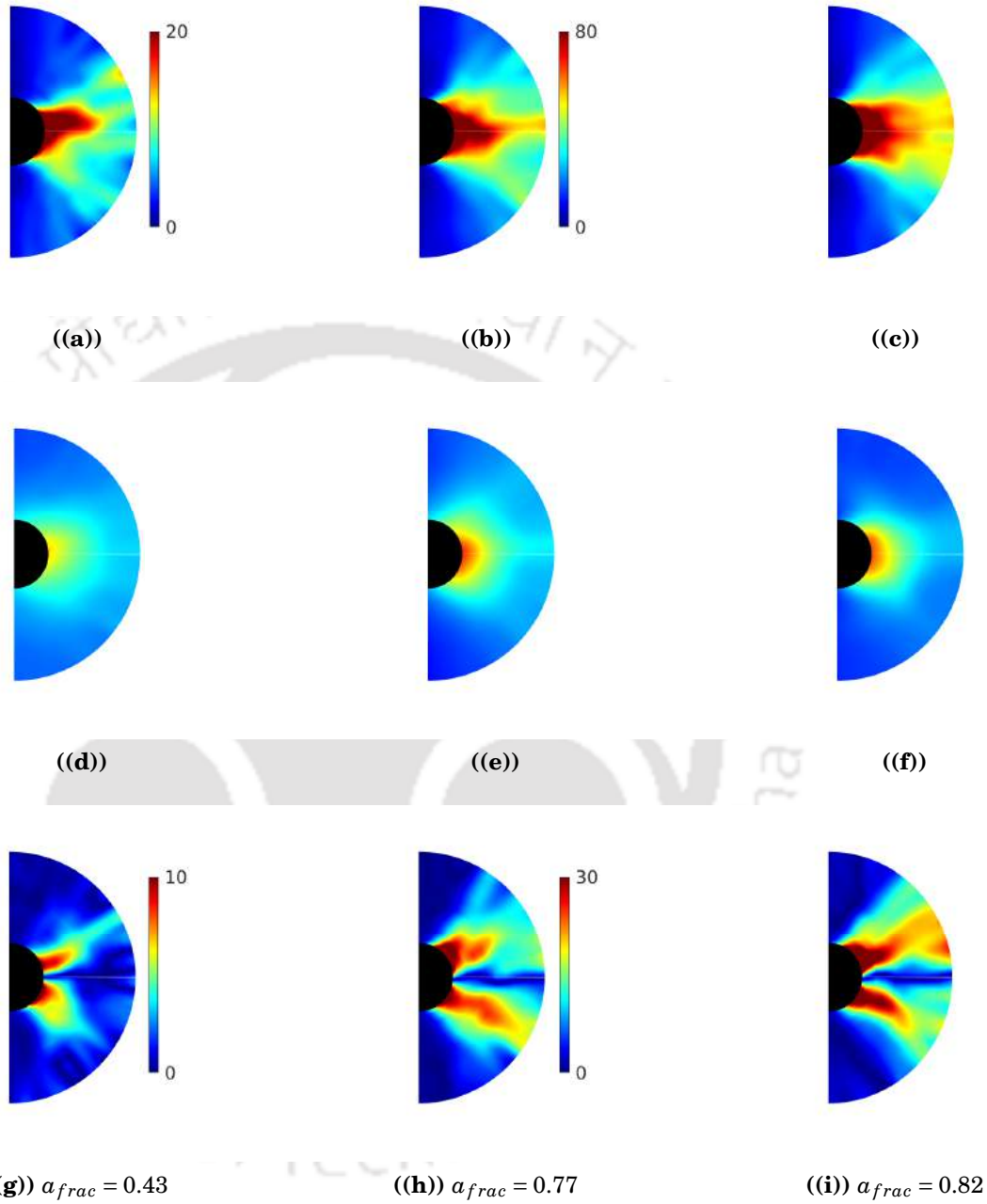

((a)) ((b)) ((c))

((d)) ((e)) ((f))

((g)) $a_{frac} = 0.43$ ((h)) $a_{frac} = 0.77$ ((i)) $a_{frac} = 0.82$

Figure 4.18: The time-averaged flow fields for depicting pressure $P(dyne/cm^2)$, velocity $V(cm/s)$ and shear stress $|\sigma_{xy}|(dyne/cm^2)$ infront of the intruder ($D_i = 5cm$) for different area fractions (a_{frac}): (a), (d), (g) 0.43, (b) (e), (h) 0.77 and (c), (f), (i) 0.83. The velocity of the intruder is $V_i = 5$ cm/s, $\mu = 0.5$ and the dumbbell fraction (db_{frac}) of the system is 0.5.

between the contacting particles around the surface of the intruder. Consequently, high shear stress is experienced by these particles which correspond to the regions of deep red.

However, this phenomena is not significant at positions far away from the intruder as there is hardly any relative motion between the particles. Shear stress is almost zero in the regions above and below the intruder as the particles in those regions are unaffected by its movement because our system is a gravityless one.

Figure 4.14 a, b and c shows the mean pressure fields at the diameters of the intruder D_i = 1cm, 5cm and 10cm respectively for $db_{frac} = 0.5$. As the intruder diameter increases, the high-stress zone expands infront of it. This is because the larger the intruder surface available, the larger the size of the cluster it can hold infront of it, particularly in the y direction. The regions of red colour in the velocity fields increases with an increase in D_i (figure 4.14 d, e and f). This result supports our claim that the size of the cluster increases with an increase in the intruder's diameter. The velocities of the particles on the front surface of the intruder experience the same velocity as that of the intruder. The velocity reduces gradually as the distance from the intruder increases due to a decrease in the stress transmission as noticed in figure 4.14 a. As the diameter of the moving intruder increases, more layers of particles infront of it are forced to detour around a larger distance and then gets detached from it. This yields a relative motion among the particles at different radial distances from the intruder's centre. Consequently, the shear stress increases with an increase in the diameter of the intruder (see figure 4.14 g, h and i). We have also shown the flow fields of $\phi = 0.82$ with $\mu = 0.0$ for different dumbbell fraction (shown in figure 4.15), figure 4.16 shows the flow fields for $\phi = 0.77$, $\mu = 0.5$ and figure 4.17 for $db_{frac} = 0.5$, $\mu = 0.5$ at different area fraction.

4.4 Conclusions

In this work, we studied the dynamics of a moving intruder and its effect on a mixture of dumbbells and discs in the absence of gravity. To this end, we studied the effect of parameters such as the fraction of dumbbells, the area fraction, the intruder's diameter and its velocity. The drag force on the intruder moving through granular media increases with an increase in the fraction of dumbbells at constant area fraction. This is due to an additional resistance offered by the dumbbells apart from the inter-particle friction. Surprisingly, the so-called additional resistance seems to be insignificant in the absence of inter-particle friction. In the sense, the drag force is independent of the fraction of dumbbells in a frictionless system. Another interesting result is the drag force on an intruder scales as the square of its velocity irrespective of the fraction of dumbbells(V_i

is in the range of 0.1cm/s to 25cm/s), the area fraction of the system or the intruder's diameter. Furthermore, we presented the mean flow fields to show the response of the granular media to a moving intruder. They revealed that the stress experienced by the particles infront of the intruder increases with an increase in the intruder's diameter. This is due to an increase in the size of the cluster of particles formed infront of it resulting from an increase in the intruder's surface. Moreover, as the diameter of the intruder increases, it forces the larger number of particles infront of it to detour around it. This results in greater shear stress experienced by the particles infront of the intruder.

BIBLIOGRAPHY

[1] Manish Dhiman, Sonu Kumar, K. Anki Reddy, and Raghvendra Gupta. Origin of the long-ranged attraction or repulsion between intruders in a confined granular medium. *Journal of Fluid Mechanics*, 886:A23, 2020.

[2] Takatsune Furuta, Sonu Kumar, Katha Anki Reddy, Hirofumi Niiya, and Hiroaki Katsuragi. Packing-dependent granular friction exerted on a rod withdrawn from a granular layer: the role of shear jamming. *New Journal of Physics*, 21(2):023001, feb 2019.

[3] Fabricio Q. Potiguar and Yang Ding. Lift and drag in intruders moving through hydrostatic granular media at high speeds. *Phys. Rev. E*, 88:012204, Jul 2013.

[4] R. Albert, M. A. Pfeifer, A.-L. Barabási, and P. Schiffer. Slow drag in a granular medium. *Phys. Rev. Lett.*, 82:205–208, Jan 1999.

[5] Chuanping Liu, Hongmei Wan, and Li Wang. Effect of movement direction on resistance force in granular media. *Powder Technology*, 344:545–550, 2019.

[6] I. Albert, J. G. Sample, A. J. Morss, S. Rajagopalan, A.-L. Barabási, and P. Schiffer. Granular drag on a discrete object: Shape effects on jamming. *Phys. Rev. E*, 64:061303, Nov 2001.

[7] Ali Abbas Zaidi and Christoph Müller. Vertical drag force acting on intruders of different shapes in granular media. In *EPJ Web of Conferences*, volume 140, page 02011. EDP Sciences, 2017.

[8] Dengming Wang, Yahui Yang, and Wei Du. The drag on a vibrated intruder moving in the confined granular media. *Powder Technology*, 286:385–391, 2015.

[9] Fuping Zhou, Suresh G Advani, and Eric D Wetzel. Slow drag in polydisperse granular mixtures under high pressure. *Physical Review E*, 71(6):061304, 2005.

[10] Fuping Zhou, Suresh G Advani, and Eric D Wetzel. Simulation of slowly dragging a cylinder through a confined pressurized bed of granular materials using the discrete element method. *Physics of Fluids*, 19(1):013301, 2007.

[11] Fuping Zhou, Suresh G Advani, and Eric D Wetzel. Simulation of the slow drag of a cylinder through a confined pressurized bed of dumbbell and elliptically cylindrical granules using the discrete element method. *Computer Modeling in Engineering and Sciences (CMES)*, 39(1):49, 2009.

[12] F Zhou, SG Advani, and ED Wetzel. Characterization of the viscous behavior of compacted ceramic particles under shear and pressure loads. *International Journal of Applied Mechanics and Engineering*, 10(3):505–514, 2005.

[13] D. J. Costantino, J. Bartell, K. Scheidler, and P. Schiffer. Low-velocity granular drag in reduced gravity. *Phys. Rev. E*, 83:011305, Jan 2011.

[14] A. Seguin, A. Lefebvre-Lepot, S. Faure, and P. Gondret. Clustering and flow around a sphere moving

into a grain cloud. *The European Physical Journal E*, 39(6):63, Jun 2016.

[15] A. Vamsi Krishna Reddy, Sonu Kumar, K. Anki Reddy, and Julian Talbot. Granular silo flow of inelastic dumbbells: Clogging and its reduction. *Phys. Rev. E*, 98:022904, Aug 2018.

[16] H Kruggel-Emden, S Rickelt, S Wirtz, and V Scherer. A study on the validity of the multi-sphere discrete element method. *Powder Technology*, 188(2):153–165, 2008.

[17] Hamzeh Pourtavakoli, Eric JR Parteli, and Thorsten Pöschel. Granular dampers: does particle shape matter? *New Journal of Physics*, 18(7):073049, 2016.

[18] A. Vamsi Krishna Reddy, Sonu Kumar, and K. Anki Reddy. Granular particle-shape heterogeneous mixtures discharging through a silo. *Journal of Fluid Mechanics*, 912:A22, 2021.

[19] Sandip Mandal and D. V. Khakhar. Dense granular flow of mixtures of spheres and dumbbells down a rough inclined plane: Segregation and rheology. *Physics of Fluids*, 31(2):023304, 2019.

[20] P. A. Cundall and O. D. L. Strack. A discrete numerical model for granular assemblies. *Géotechnique*, 29(1):47–65, 1979.

[21] Steve Plimpton, Paul Crozier, and Aidan Thompson. Lammps-large-scale atomic/molecular massively parallel simulator. *Sandia National Laboratories*, 18, 2007.

[22] William Humphrey, Andrew Dalke, and Klaus Schulten. VMD – Visual Molecular Dynamics. *Journal of Molecular Graphics*, 14:33–38, 1996.

[23] C. R. Wassgren, J. A. Cordova, R. Zenit, and A. Karion. Dilute granular flow around an immersed cylinder. *Physics of Fluids*, 15(11):3318–3330, 2003.

[24] J. E. Hilton and A. Tordesillas. Drag force on a spherical intruder in a granular bed at low froude number. *Phys. Rev. E*, 88:062203, Dec 2013.

[25] Sonu Kumar, Manish Dhiman, and K. Anki Reddy. Magnus effect in granular media. *Phys. Rev. E*, 99:012902, Jan 2019.

[26] Fabricio Q Potiguar and Yang Ding. Lift and drag in intruders moving through hydrostatic granular media at high speeds. *Physical Review E*, 88(1):012204, 2013.

[27] Daniel Barreto and Catherine O'Sullivan. The influence of inter-particle friction and the intermediate stress ratio on soil response under generalised stress conditions. *Granular Matter*, 14(4):505–521, 2012.

[28] L Kondic, A Goullet, CS O'Hern, M Kramar, Konstantin Mischaikow, and RP Behringer. Topology of force networks in compressed granular media. *EPL (Europhysics Letters)*, 97(5):54001, 2012.

[29] Peijun Guo. Critical length of force chains and shear band thickness in dense granular materials. *Acta Geotechnica*, 7(1):41–55, 2012.

[30] Miroslav Kramár, Arnaud Goullet, Lou Kondic, and Konstantin Mischaikow. Persistence of force networks in compressed granular media. *Physical Review E*, 87(4):042207, 2013.

[31] Andreea Panaitescu, Xavier Clotet, and Arshad Kudrolli. Drag law for an intruder in granular sediments. *Physical Review E*, 95(3):032901, 2017.

[32] BJ Glasser and I Goldhirsch. Scale dependence, correlations, and fluctuations of stresses in rapid granular flows. *Physics of Fluids*, 13(2):407–420, 2001.

CHAPTER 5

SHAPE DEPENDENCE ON THE RISE AND SINK OF A WIGGLING INTRUDER

5.1 Introduction.

Animals native to deserts have an extreme shortage of food and water, making any wastage of energy very detrimental to them. As such, their bodies have undergone evolutionary changes to have the optimal shape required to walk on the surface or even exhibit subsurface motion with minimum loss of energy. For example, sand lizards and sidewinder snakes employ a wiggling motion to move in the sand. A comprehensive understanding of this kind of motion has various applications. It can help design robots that can swim through sand or snow during rescue operations or while exploring new terrains. Apart from that, it can also be applied in mining or related operations.

The subsurface motion of animals has garnered interest in the fields of earth-sciences [1, 2], biology [3], and engineering [4] owing to its interesting dynamics. To understand the mechanism behind their movement through the granular medium, researchers [3, 5, 6] conducted laboratory experiments on the creatures. Maladen *et al.* [3] studied how a sand lizard moves within the granular media with the help of high-speed x-ray imaging. Surprisingly, they noticed that the lizard does not use its limbs for propulsion, but it generates thrust by propagating a wavy motion of its body once it is under the

surface. Sharpe *et al.* [6] investigated the neuromechanical movement of sandfish lizard during its walking above the surface or sand swimming under the surface of a granular medium with the help of visible light imaging using electromyogram (EMG). The authors reported that the frictional forces play a prominent role in resisting the intrusion of the creatures. Moreover, they observed that the resistance to the undulatory motion of the creatures increases with the depth. Despite the resistance, the sand-dwelling creatures have adopted certain mechanisms to move within the bed of granular particles. Maladen *et al* [7, 8] have tried to comprehend this phenomenon by developing sand swimming robots . The ratio of forwarding speed to the wave speed of a robot was noticed [7] to increase with an increase in the particle-particle friction but decrease with an increase in the particle-robot friction. In addition, Maladen *et al.* [8] investigated various head shapes of the robot and their influence on the drag-induced lift. The authors noticed that for certain wedge shapes of the robot, it reaches the free surface whereas, for other ones, it sinks to the bottom, indicating the importance of the robot's shape on rise/sink dynamics. Apart from these studies, to gain a better insight into the creatures movement within granular media, they have been modeled as self-energized objects.

Few recent studies focused on understanding the dynamics of a self-energized object oscillating horizontally in both two [9] and three-dimensional systems [5, 10]. Huang *et al.* [9] have tried to explain the mechanism behind the rise and sink of a horizontally oscillating circular intruder in a two-dimensional system with the help of a mathematical model. They stated that the amplitude and frequency at which the intruder object oscillates mainly contribute to its rise or sink within the media. They have also reported a minimum oscillation amplitude (A_{min}) below which the intruder does not sink irrespective of its frequency. Ping *et al.* [10] noticed that the intruder rises at low amplitude rates and sinks at high amplitude rates. They also found that an intruder might either rise or sink or remain at the same initial vertical position depending on its oscillating frequency and amplitude in a three-dimensional system. Further, the authors explained the driving mechanisms such as fluidization or cavity formation behind the intruder's vertical dynamics.

The previous studies were primarily concerned with the sole effect of the intruder's horizontal wiggling motion on its vertical dynamics. However, a coupled effect of wiggling motion along with other properties of the intruder can enhance the rise/sink dynamics. To this extent, Liu *et al.* [5] studied the combined effect of rotation and oscillation of a spherical intruder on its rise/sink dependence within a three-dimensional granular

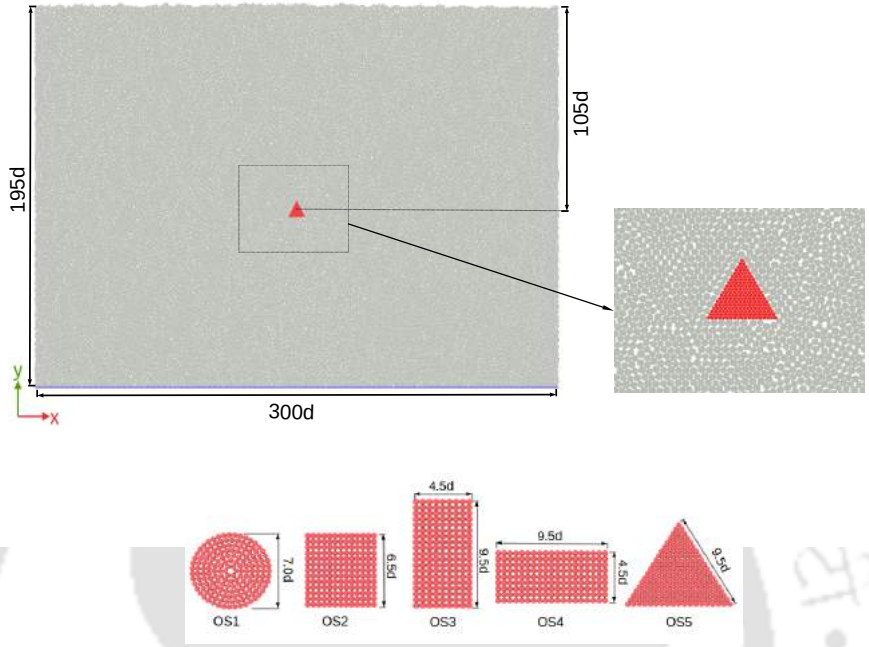

Figure 5.1: Initial configuration with one of the shapes (triangle) kept at a depth $h = 105d$ from the free surface. The base is made of particles of size $1d$(blue particles) at $y = 0$ while the top surface is free to move and periodic boundary conditions are applied in x direction.The intruder shapes that are considered in our study are disc $OS1$, square $OS2$, rectangle with its longer dimension along the y-axis $OS3$, rectangle with its longer dimension along the x-axis $OS4$, and equilateral triangle $OS5$.

media. The effect of intruder's shape, coupled with its wiggling motion has not been studied to the best of our knowledge. In this regard, we numerically investigated how the shape of the intruder affects its vertical motion induced by horizontal wiggling. To this end, we considered five different intruder shapes: a disc, a square, a rectangle with a small base, a rectangle with a large base, and an equilateral triangle. We studied how the oscillation parameters affect their vertical dynamics for each of these shapes. Further, we probed the influence of the properties of the granular medium, such as the coefficient of friction on the intruder's vertical motion. Finally, we proposed a mathematical model that predicts the intruder's rise/sink dynamics depending on its shape and the oscillation parameters.

Simulation parameters	Values
K_n	$2.00 \times 10^6 \rho d g$
K_t	$2.46 \times 10^6 \rho d g$
γ_n	$2500\sqrt{g/d^3}$
γ_t	$2500\sqrt{g/d^3}$
$timestep$	$10^{-4}\sqrt{d/g}$
μ	0.1

Table 5.1: The parameters and its values used in our numerical simulations

5.2 Simulation methodology

To study the dynamics of a horizontally oscillating intruder object within a two-dimensional granular medium, we used the discrete element method (DEM) introduced by [11]). Figure 5.1 shows the initial configuration of our system having dimensions of $300d \times 195d$ along the x and y-axis, where d is the mean particle diameter. The intruder is placed at a depth of $105d$ from the free surface and at the centre of the simulation system. A set of particles are introduced uniformly at the top of the system which gets settled at the bottom due to gravity while keeping the intruder stationary. Then, another set of particles are introduced and so on until the height of the granular bed reaches $195d$. The total number of particles comprising the system at the end is $N_t = 63000$. The diameter of the particles range from $0.9d$ to $1.1d$ to avoid crystalization and while pouring and settling, we ensured that there are no overlaps among the particles. We further continued the simulation until the total kinetic energy of all the particles in the system have reached almost zero. At time $t = 0$, the intruder is oscillated horizontally with a velocity $V_x = A\ sin(t \times 2\pi/T)$ where A, T represents the amplitude and the time period of oscillation and t is the time elapsed. In our work, we have considered five different shaped intruders, which are pictorially represented in figure 1. Each of the individual intruder shapes is created by gluing a set of spherical particles having a diameter of $0.5d$ in such a way that their entire mass is the same for all the shapes. The DEM technique is explained in chapter 2. Table 6.1 lists the parameters that is used in the simulations.

Each of the simulations was performed for a run time of $10^7 \Delta t$ to maintain parity among all the calculated results. The simulations are performed using dimensionless units, by considering acceleration due to gravity g, mean particle diameter d, and density ρ as the basic units. The values of d, ρ, and g are set to 1.0 without loss of generality. All

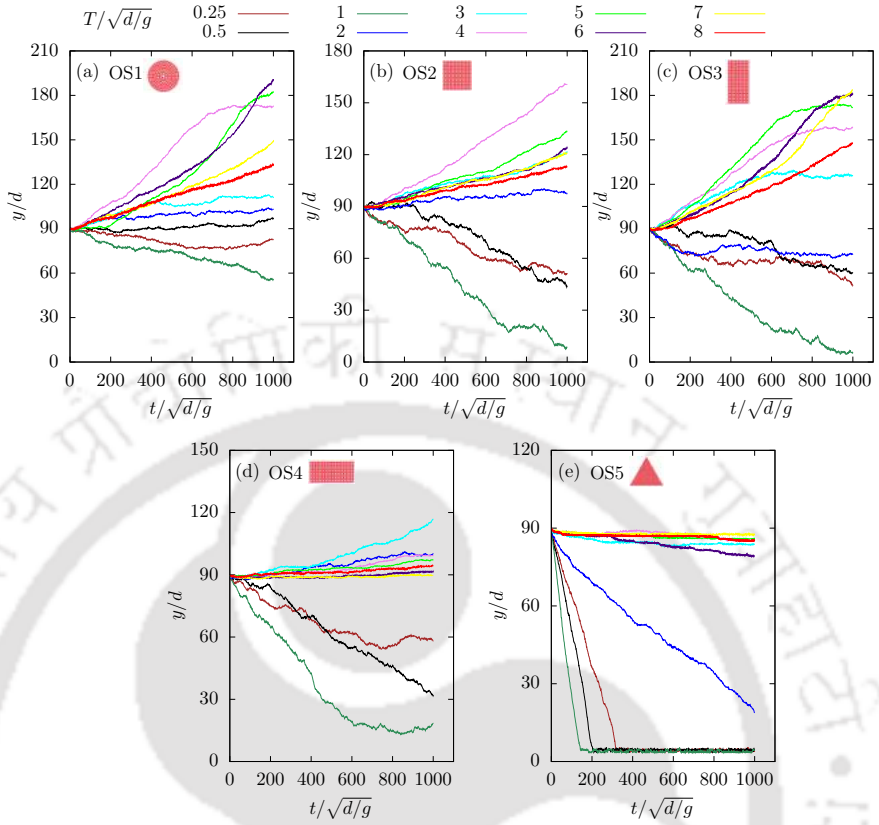

Figure 5.2: The vertical displacement of the intruder (a) disc (b) square, (c) narrow-rectangle (d) wide-rectangle, and (e) triangle shapes as a function of simulation time(t) for an oscillation amplitude A/d= 3 and at different time-period($T/\sqrt{d/g}$). The settling level at the top and bottom of the graphs depicts the IO reaching the top and bottom surface of the medium.

the simulations are carried out using the Large Atomic Molecular Massively Parallel Simulator (LAMMPS) ([14]), and for the visualization OVITO package ([15]) has been utilized.

5.3 Results and Discussion

In this section, we presented the numerical results obtained for five different intruder shapes subjected to different oscillation parameters. We horizontally oscillated each of the intruders at different constant amplitudes A/d = 0.5, 1, 3, 5 and at various constant time periods $T/\sqrt{d/g}$ ranging from 0.25 to 8. This section is organised as follows: Subsection 5.3.1 demonstrates the vertical displacement of each of the intruders as a function of time at various time periods $T/\sqrt{d/g}$ and for an amplitude A/d = 3. The average rate of

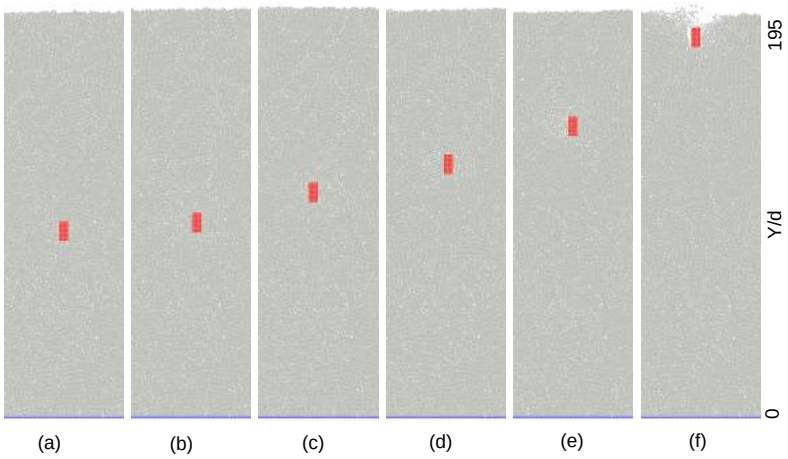

Figure 5.3: A pictorial representation depicting the position of the narrow-rectangle $OS3$ for A/d=3 and $T/\sqrt{d/g}$=7 at different simulation time $t/\sqrt{d/g}$: (a) 0 (b) 100 (c) 300 (d) 500 (e) 700 and (f) 1000.

vertical displacement V_y dependence on the intruder's shape at different A/d, T and μ is discussed in subsection 5.3.2. In subsection 5.3.3, we showed the average rate of vertical displacement of the intruder as a function of the oscillating phase-angle ϕ. In the next subsection 5.3.4, we have shown the drag force F_d experienced by the oscillating intruder as a function of ϕ. In subsection 5.3.5, we elucidated the mean flow fields around the intruder. Lastly, in subsection 5.3.6, we have compared our results with the proposed mathematical model and explained the physical phenomenon leading to the rise and sink of the intruder for different parameters considered in the study.

5.3.1 Vertical displacement of oscillating intruder

In this subsection, we showed the vertical displacement of the intruders as a function of the simulation time t for an amplitude of $A/d = 3$ at different time-periods $T/\sqrt{d/g}$. Figure 5.2 a shows the vertical displacement of a disc-shaped intruder OS1 oscillated at different T. At time periods of oscillation $T \geq 2$, a wake is formed either to the left side of the intruder or to the right side, depending on its direction of motion. In this sense, when the intruder moves from left to right, the wake is developed to the left side of the intruder. When the intruder changes its direction of oscillation and starts to move from right to left, it interacts with the wake that is on its left side. When the intruder

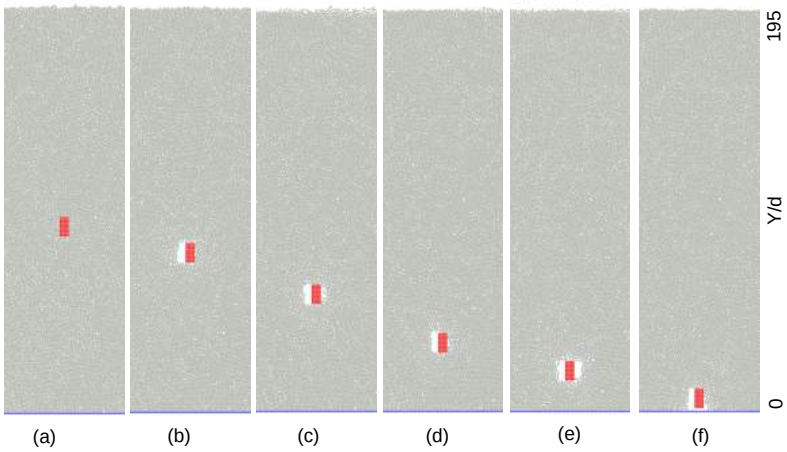

Figure 5.4: A pictorial representation depicting the position of the narrow-rectangle $OS3$ for A/d=3 and $T/\sqrt{d/g}$=1 at different simulation time $t/\sqrt{d/g}$: (a) 0 (b) 100 (c) 300 (d) 500 (e) 700 and (f) 1000.

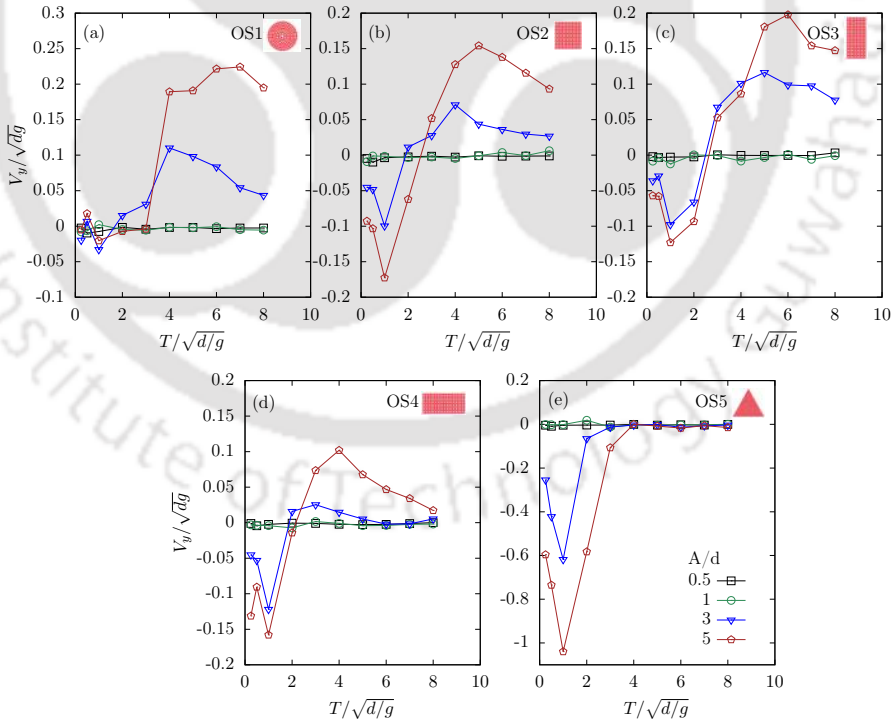

Figure 5.5: The rise rate(V_y) of the horizontally oscillating intruder as a function of its time-period(T) for different amplitude A. Here, each plot corresponds to a different intruder shape: (a) disc, (b) square, (c) narrow-rectangle, (d) wide-rectangle, and (e) triangle .

reaches the middle point of oscillation, the wake to its left vanishes, and simultaneously another wake evolves to the intruder's right side. When the intruder is traversing the granular medium, the particles above the wake region tries to fill the wake due to the action of gravity. In the process, a bed of particles is created on the edges of the wake region. When the intruder changes its direction of motion, it has to limb the bed of particles to move ahead, and thus a vertical displacement of the intruder takes place. This is the reason behind the rise of the disc-shaped intruder at longer time periods. Interestingly, the intruder neither sinks nor rises at certain intermediate time-periods $T = 2$. At time periods T ranging from 0.25 to 1, the wake is formed not only beside the intruder but also above and below it. This is due to its high oscillation frequency and, consequently, a greater momentum transfer to the surrounding particles. The presence of the wake below the intruder propels it to sink due to the gravity acting on it. Thus, the disc-shaped intruder sinks at shorter time periods or larger frequencies of oscillation. Similar behavior has been observed in both 2D [9] and 3D [10] granular systems, where the disc (2D) and the spherical (3D) shaped intruders rise at lower frequencies and sink at higher frequencies of oscillation.

The square-shaped intruder shows similar behavior (figure 5.2 b) to that of disc one. However, the square-shaped intruder is noticed to move to a lower vertical distances than the disc one for longer time periods. This is due to the larger stress experienced by the square one ($OS2$) as compared to that of the disc one ($OS1$) from the particles above. The reason for it is due to the presence of a flat surface at the top of the square intruder and a curved one for the disc one. Figure 5.2 c shows the vertical displacement of a rectangle with a small base ($OS3$) whose behavior is similar to that of the disc and the square shapes. Though rectangle and square-shaped intruders have flat top surfaces, the former moves to a higher vertical distance than the latter one. The reason for this behavior is that the rectangle intruder ($OS3$) has a smaller top surface than the square one and hence a smaller stress from the particles above it. A pictorial representation of the rectangle intruder ($OS3$) is shown to depict this rise and sink phenomena at different simulation times $t/\sqrt{d/g}$ when oscillated at a higher time period ($T/\sqrt{d/g} = 7$) (figure 5.3) and at a lower one ($T/\sqrt{d/g} = 1$) (figure 5.4) for a given amplitude $A/d = 3$. Further, the rectangle with a larger base/top surface ($OS4$) moves upwards at a slower rate than (figure 5.2 d) that of the square one and the rectangle one with a smaller base ($OS3$). This is due to a larger top surface and consequently a higher stress from the particles above it. Interestingly, the sinking behavior is observed to be independent

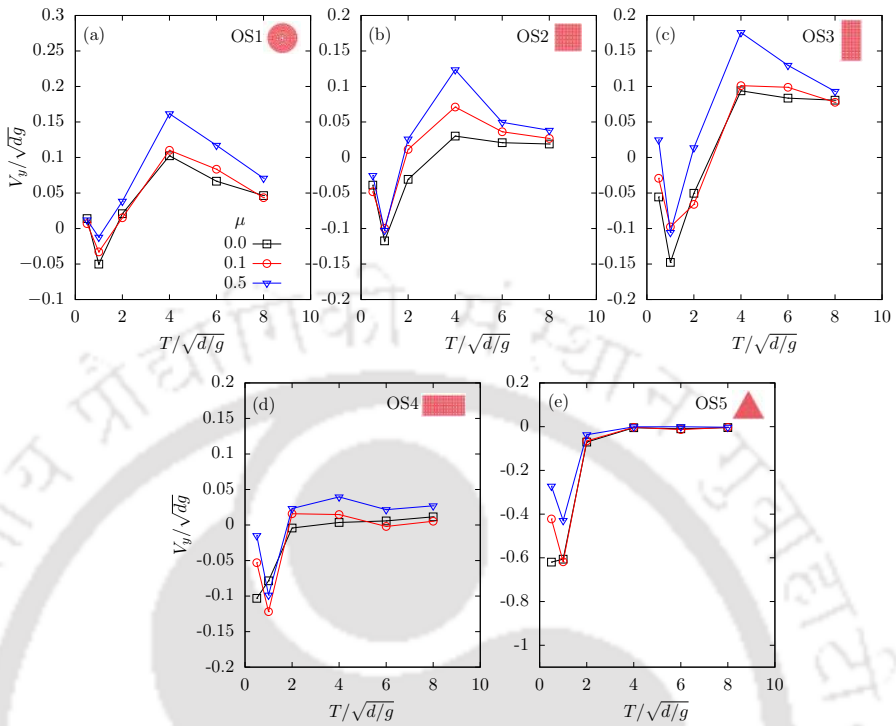

Figure 5.6: The rise rate (V_y) of the horizontally oscillating intruder as a function of its time-period (T) for different friction coeficient μ and amplitude $A/d = 3$. Here, each plot corresponds to a different intruder shape: (a) disc, (b) square, (c) narrow-rectangle, (d) wide-rectangle, and (e) triangle.

of the base length of the quadrilaterals ($OS2, OS3$ and $OS4$) considered in our study. The triangular intruder behaved differently as compared to all the other shapes. In this sense, the triangular intruder is noticed to sink always irrespective of the time periods (figure 5.2 e). In this case, a bed of particles is not created near the edges of the wake owing to the intruder's inclined sides and sharp edges. An intriguing observation is that the maximum vertical distance traversed by the intruder varies non-monotonically with the time period. Apart from the maximum vertical displacement traveled by an intruder, how quickly an intruder can rise or sink is equally important. This aspect of the intruder is discussed in the next subsection.

5.3.2 Rate of rise of intruder with time-period

In this subsection, we explain how the vertical displacement rate of an intruder varies with its shape and oscillation parameters. The rate of change of vertical displacement

is defined as $V_y = (y_f - y_i)/(t_f - t_i)$. Here, y_i and y_f are the initial and final vertical positions of the intruder at times t_i and t_f. Note that t_i is considered at $1/10^{th}$ of the total simulation time ($1000\sqrt{d/g}$). For some cases, we noticed the intruder reaches its final vertical position before the end of the simulation (1000 $\sqrt{d/g}$). An example of such behaviour can be seen in figure 5.2 a for a circular intruder at time period $T = 4$ for which $t_f = 650$. For these type of cases, we have taken t_f as the time at which the intruder is about to reach its final vertical position. Henceforth, the positive value of V_y implies the intruder is rising and the negative value of V_y corresponds to sinking. Figure 5.5 shows the intruder's rate of rise/sink as a function of time-period (T) and for amplitudes, A/d = 0.5, 1, 3, and 5. The rate of rise/sink is negligible at all time periods for the amplitudes (A) of 0.5 and 1 for all the intruder shapes. Similar behavior has been reported for a oscillating disc in a previous work by [9], where the authors reported that to facilitate the vertical motion of the intruder, a minimum amplitude of oscillation is necessary.

Figure 5.5 a shows a slightly negative V_y for $A/d = 3$ and at $T \leq 1$ for a disk-shaped intruder. This result is consistent with the negative vertical displacement observed in figure 5.2 a for $T \leq 1$. At $T \geq 2$, we observed a positive V_y for the range of time periods considered in our study. Surprisingly, as the time-period increases, the rise rate first increases, reaches a maxima and then decreases. When the intruder changes its direction of motion, it is impelled to climb over a bed of particles leading to its rise at large time periods. Suppose, if the intruder is moving from left to right, then the above-mentioned bed of particles corresponds to the ones that are trying to fill the wake which is formed just to the right of the intruder. These particles could be the ones that fall from above the intruder or the ones that are adjacent to the wake. As the time period increases, more particles get piled up, and consequently, the intruder has to climb over a larger set of particles. This leads to an increase in its vertical position and its rise rate. As time period increases, we noticed a maxima and then a decrease in the rise rate. The reason for this is at larger time periods, greater number of particles gets piled up which dampens the upward motion of the intruder. In summary, the group of particles falling behind the intruder, or in other words, the size of the bed of particles behind it, is responsible for the non-monotonic behavior of the intruder's rise rate. Even at amplitude $A/d = 5$, the non-monotonic behavior in the rise rate is noticed. Moreover, the rise rate increases with an increase in the amplitude.

The rate of rise/sink of a square intruder ($OS2$) as a function of the time period is shown in figure 5.5 b. At time periods $T \leq 2$, amplitude $A/d = 3$, the square intruder has

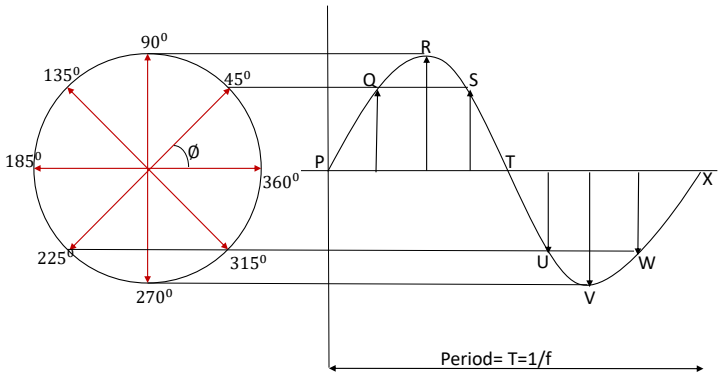

Figure 5.7: Oscillatory motion of the intruder as sine wave function representing the phase angle(ϕ)

a negative rate of vertical displacement or sink rate. Interestingly, as the T increases, the sink rate gradually increases reaching a maxima and then decreases. At $T < 2$, a wake is formed not only on either sides of the intruder but also above and below it as a result of a high frequency of oscillation. The action of gravity on the intruder coupled with a low area fraction of particles below it results in its sinking. As the time period increases, the size of the wake above the intruder decreases, and consequently, the number of particles interacting, or in other words, the stress exerted on the top surface of the intruder increases. This results in an increase in the sink rate. With a further increase in the time period, the wake size below the intruder decreases, resulting in the resistance to the downward motion of the intruder. In summary, the wake dynamics above and below the intruder are responsible for the sink rate's non-monotonic behavior. At time periods $T \geq 2$, the square intruder experiences mostly a positive rate of vertical displacement. The square-shaped intruder shows a non-monotonic rise rate as a function of time period at $T \geq 2$, similar to that of the disk-shaped intruder. However, the square-shaped intruder has lower rise rates than that of the disk-shaped intruder. This is because the curved base of the disk-shaped intruder enables it to ascend the bed of particles more quickly than that of square one. Figure 5.5 c displays the rise/sink rate of a rectangle-shaped ($OS3$) intruder as a function of time period. The rectangle-shaped intruder has a smaller base and a larger height. The rectangle-shaped intruder shows qualitatively similar behavior to that of the square-shaped one. However, at $T \leq 2$, the

sink rate is smaller for the rectangle-shaped intruder ($OS3$) as compared to that of the square-shaped intruder($OS2$). This is due to a smaller top surface of the rectangle-shaped intruder ($4.5d$) than that of the square-shaped one ($6.5d$), which yields in smaller stress experienced by the top surface of $OS3$ than that of $OS2$. Due to a small base, $OS3$ can climb the bed of particles more easily than that of $OS2$. This results in slightly higher rise rates for the $OS3$ shape than the $OS2$ one. For the rectangle-shaped intruder with a larger base and a smaller height ($OS4$), an opposite behavior is witnessed (figure 5.5 d). In this sense, the rise rate is smaller for $OS4$ as compared to that of $OS3$ and $OS2$. Moreover, the magnitude of the sink rate is greater for $OS4$ than that of $OS2$ and $OS3$ owing to the larger top surface of $OS4$. The rate of vertical displacement of the equilateral-triangle-shaped intruder ($OS5$) is shown in figure 5.5 e. The triangle-shaped intruder shows a mostly negative rate of vertical displacement because the V-shaped structure formed by its two edges at the vertices disables it to climb over the bed of particles. The intruder displayed a non-monotonic sink rate dependence on the time period. However, the magnitude of the sink rate is significantly higher than the other shapes considered in our study. The reason for it is due to an almost continual downward stress exerted by the particles on the triangle's slant edges. We have also found that there is an increase in the rate of rise of the intruder with the increase in the intergranular friction of $\mu = 0.0$ to 0.5 (figure 5.6). The same kind of trend has also been reported by [5] for a 3D system with a circular intruder and also stated that there is a saturation of rise rate when $\mu \geq 0.5$.

Moreover, due to its unique geometry, each shape has a different angle of contact around its surface with the surrounding particles when oscillating horizontally. With square and rectangle shapes having a flat outer surface, triangular shape with an inclined angle, and disc with a smooth curvature. If we compare the positive V_y value which correspond to the rise of the intruder for the different shapes at $A/d = 3$ and 5, than it is in the order of : $V_y;OS1 > V_y;OS3 > V_y;OS2 > V_y;OS4 > V_y;OS5$. Thus confirming that the geometric shape and orientation also affect the intruder's movement and its rate of rise in the system when oscillated horizontally.

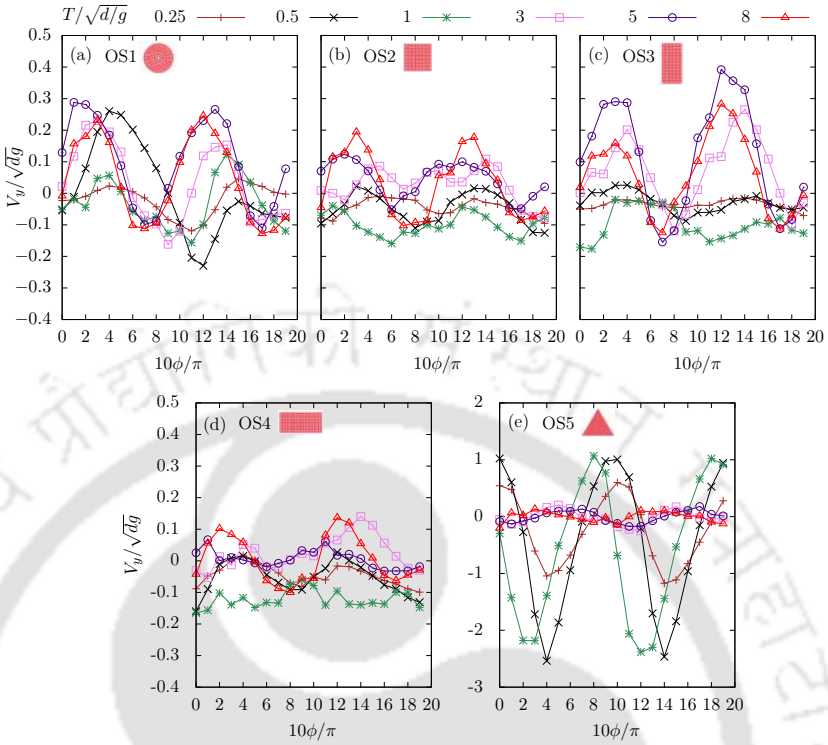

Figure 5.8: The rise rate(Vy) of the intruder vs the phase angle at $A/d = 3$ and different $T/\sqrt{d/g}$ for (a)disc, (b)square, (c)narrow-rectangle, (d)wide-rectangle, and (e)triangle shaped intruder object.

5.3.3 Average rate of vertical displacement of an intruder with phase angle

In this subsection, we elucidate how the average rate of vertical displacement of the intruder varies with different positions of the oscillation cycle. One oscillation cycle involves the intruder travelling a distance of "A" from the centre to the right, then a distance of "$2A$" from right to the left, followed by a distance of "A" from left to the centre, where "A" is the amplitude. If we consider one oscillation cycle as a sine wave function, then each phase angle (ϕ) represents different horizontal positions of the intruder as shown in figure 5.7. Here, the phase angle $\phi = 0$ or $10\phi/\pi = 0$ represents the centre point of oscillation when the intruder is moving from left to right, $\phi = \pi/2$ or $10\phi/\pi = 5$ indicates the rightmost point of oscillation. In the same way, $\phi = \pi$ or $10\phi/\pi = 10$ denotes the centre point of oscillation when the intruder is moving from right to left, $\phi = 3\pi/2$ or $10\phi/\pi = 15$ indicates the leftmost point of oscillation and $\phi = 2\pi$ or $10\phi/\pi = 20$ represents

the centre point. Figure 5.8 a displays the average rate of vertical displacement (V_y) of the disc-shaped intruder as a function of its phase angle at different time periods and for an amplitude of $A/d = 3$. Here, V_y increases with ϕ from $10\phi/\pi = 0$ to $10\phi/\pi \approx 5$ where the intruder gradually climbs over the particles. When the intruder changes its direction of motion ($10\phi/\pi = 5$) and moves from right to left, the wake to the left of the intruder gradually decreases. This is associated with an increase in the number of particles interacting with the intruder increasing the resistance to the vertical motion of the intruder. Therefore, V_y decreases from $10\phi/\pi \approx 5$ to $10\phi/\pi \approx 10$. However, from $10\phi/\pi \approx 10$ to $10\phi/\pi \approx 15$ the intruder again climbs over the particles yielding an increase in the average rate of vertical displacement V_y. When the intruder moves from left to right, another wake evolves to the right of it. At $10\phi/\pi = 15$, the intruder changes its direction of motion and moves from right to left which results in a decrease in V_y due to the presence of wake to the right of the intruder. Interestingly, we witnessed both the positive and negative rates of vertical displacement in a single oscillation cycle at all timeperiods and for $A/d = 3$ for the disc-shaped intruder. At smaller timeperiods of oscillation, lower V_y is evidenced whereas, at larger timeperiods, greater V_y is noticed. This result is consistent with V_y as a function of time period (figure 5.8 a).

The square-shaped intruder (figure 5.8 b) shows qualitatively similar trends to that of the disc-shaped one. The magnitude of V_y is greater for the disc-shaped intruder ($OS1$) as compared to that of a square-shaped one ($OS2$) although the diameter of $OS1$ ($6.5d$) and the side of $OS2$ ($7.0d$) are almost of the same length. The disc has a curved surface at the top whereas the square has a flat top surface and hence square-shaped intruder experiences greater stress from the particles above it than the disc-shaped one. This results in a smaller V_y for a square-shaped intruder as compared to that of a disc-shaped one. However, for a rectangle-shaped intruder having a shorter top surface ($4.5d$), a greater V_y is evidenced (figure 5.8 c) as compared to the square one, due to smaller stress experienced from the particles above it. For a rectangle-shaped intruder with a larger base ($9.5d$), we noticed a smaller V_y due to greater stress experienced by the intruder from the particles above it (figure 5.8 d). For a triangle-shaped intruder, we evidenced a negative rate of vertical displacement V_y for most of the phase angles. This could be due to its asymmetric geometry and either of the two inclining side walls experiencing stress from the particles above it throughout the oscillation cycle.

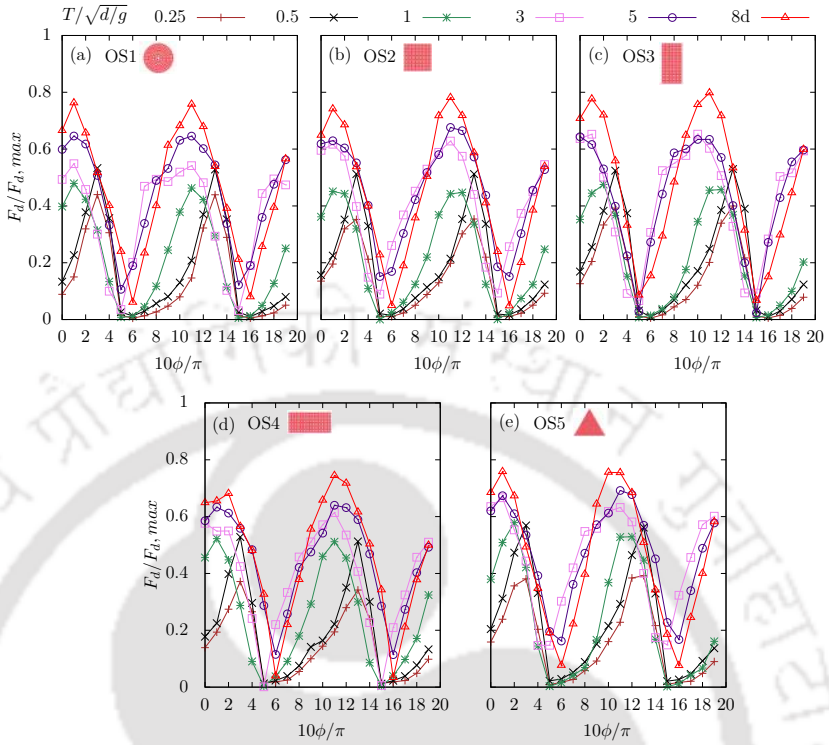

Figure 5.9: The figure shows the drag experienced at various phase angle with varying T for (a)disc, (b)square, (c)narrow-rectangle, (d)wide-rectangle, and (e)triangle shaped intruder object

5.3.4 Drag force on oscillating intruder

In this subsection, the study shows the average drag force F_d normalized by the maximum drag $F_{d,max}$ experienced by the intruder object at different phase angles during its oscillation cycle. Drag is a force acting opposite to the direction of motion of an object. As for the intruder object, to complete an oscillation cycle moves back and forth from a designated position and has to push particles in its way. So when the intruder starts oscillating from its initial position (center), it first moves towards its right side. As the intruder moves, the particles in front of it offer resistance. The drag force then gradually increases until it reaches the endpoint of its oscillation amplitude on the right side. After that, the intruder shifts its direction from right to left, and since there is wake formation during the first half of the oscillation, fewer number of particles will be in the path resulting in less drag on the intruder. Again the oscillation cycle continues with the intruder now moving from the center to the left side, resulting in a gradual increase in drag and will be maximum in the leftmost position. The same thing happens

here with the wake formation and fewer particles in contact with the intruder as it moves back from the left to the center position. In figure 5.9 a for the shape $OS1$, the average drag force increases from $\phi = 0°$ and reaches a maximum value and after that, there is a gradual decline like a sine wave and the same is also observed for the other shapes. It is also observed that at a high time period (low frequency), the particle will be uniformly distributed around the intruder even during its oscillation. But at a low time period (high frequency), the intruder hits the particles at high velocity, and while it changes its direction of motion to complete its full oscillation cycle, there will be fewer particles resisting it, due to which we can see the anomaly in drag force, and there is no uniform increase or decrease of drag force. The trend of the drag force experienced at the individual $T/\sqrt{t/g}$ for all the considered intruder shapes are observed to be similar, besides small difference in the magnitude of the dragforce. So from the results, it can be stated that the drag force experienced by the intruders during its oscillation is not dependent on the geometric shape and its orientation. The magnitude of drag force is more or less the same for all the intruder's shapes during its oscillation cycle.

5.3.5 Mean flow fields

In this subsection, we have presented the mean flow fields of parameters such as area fraction, velocity and pressure at different phase angles. To generate these flow fields, we have used the coarse-graining technique, which has been already explained in chapter 4. The flow fields demonstrated corresponds to a square region of size $30d$ around the intruder and these are obtained by averaging over a minimum of 5000 frames. Figure 5.10 a displays the mean flow field of area fraction when the intruder is at the centre point of oscillation ($10\phi/\pi = 0$) while it is moving from left to right. The area fraction is minimum in a small region on the left side of the intruder due to the development of wake. However, in a small region to the right side of the intruder, the area fraction is witnessed to be slightly lower than that of the bulk. In the above and below the regions of the intruder, the area fraction is almost the same as that of the bulk as the intruder can affect only those particles that are close to it. Figure 5.10 b shows the area fraction at the rightmost point of oscillation ($10\phi/\pi = 5$) when the intruder has changed its direction of motion and has just started to move from right to left. A larger wake is witnessed to the left side of the intruder in this case as compared to that of the one in figure 5.10 a. However, this wake gradually disappears as the intruder moves from right to left as the

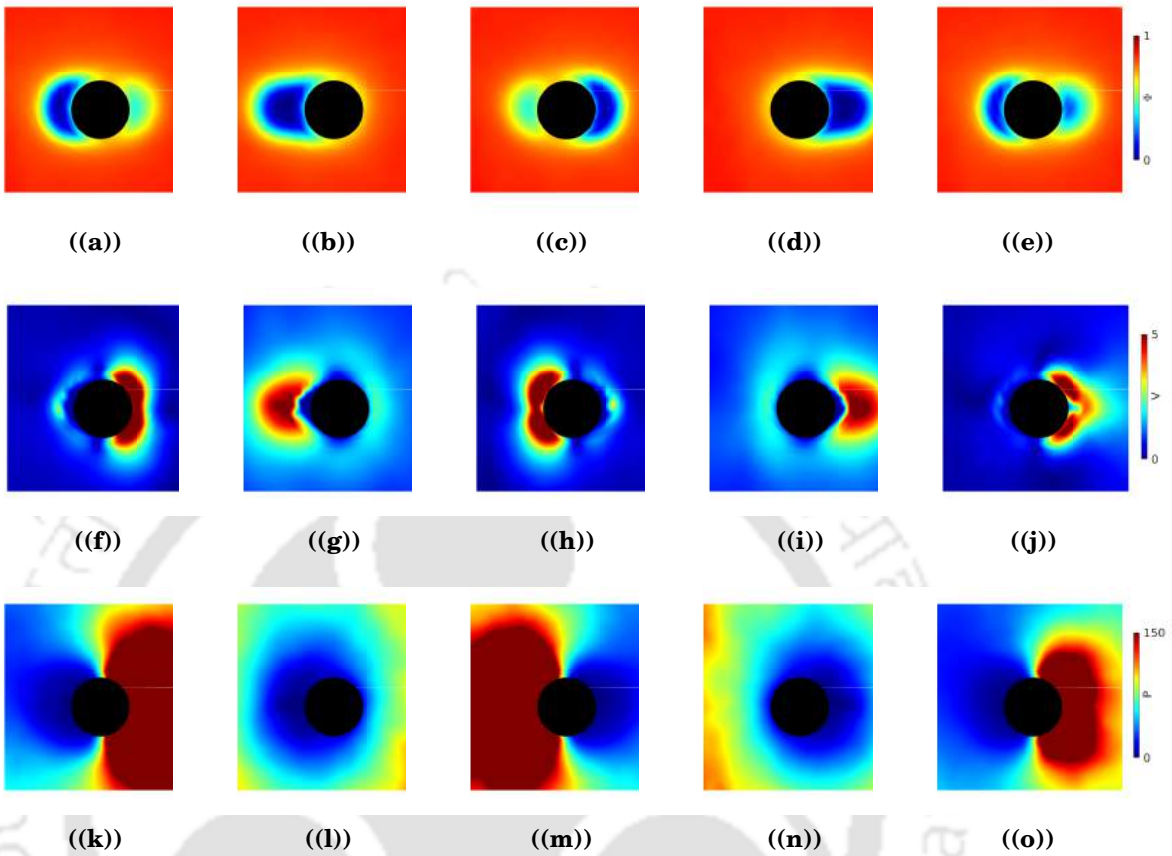

Figure 5.10: The time-averaged flow fields for depicting velocity V, pressure P, and area fraction Φ around the intruder $OS1$ (disc) for $T/\sqrt{d/g} = 1$ and different phase angle ϕ : (a), (f), (k) 0.0, (b) (g), (l) 5.0, and (c), (h), (m) 10.0, (d), (i), (n) 15.0 and (e), (j), (o) 19.0. The oscillating amplitude of the intruder is $A/d = 3$.

particles surrounding the wake try to fill it due to the action of gravity. Consequently, by the time the intruder reaches the centre point of oscillation ($10\phi/\pi = 10$), this wake is replaced by a mildly fluidized set of particles or in other words, a slightly smaller area fraction to the left of the intruder (figure 5.10 b). Moreover, another wake begins to develop to the right side of the intruder during this time. As the intruder reaches the rightmost point of oscillation ($10\phi/\pi = 15$), a large trailing wake is evidenced to the right side of the intruder (figure 5.10 d). Moreover, the mildly fluidized bed to the left side of the intruder is filled by particles above it and hence the area fraction becomes close to that of the bulk. Again as the intruder moves from right to left and reaches close ($10\phi/\pi = 19$) to the centre point of oscillation, the wake to its right is slightly filled by particles and generating a fluidized bed (figure 5.10 e). A small region of dark blue to the

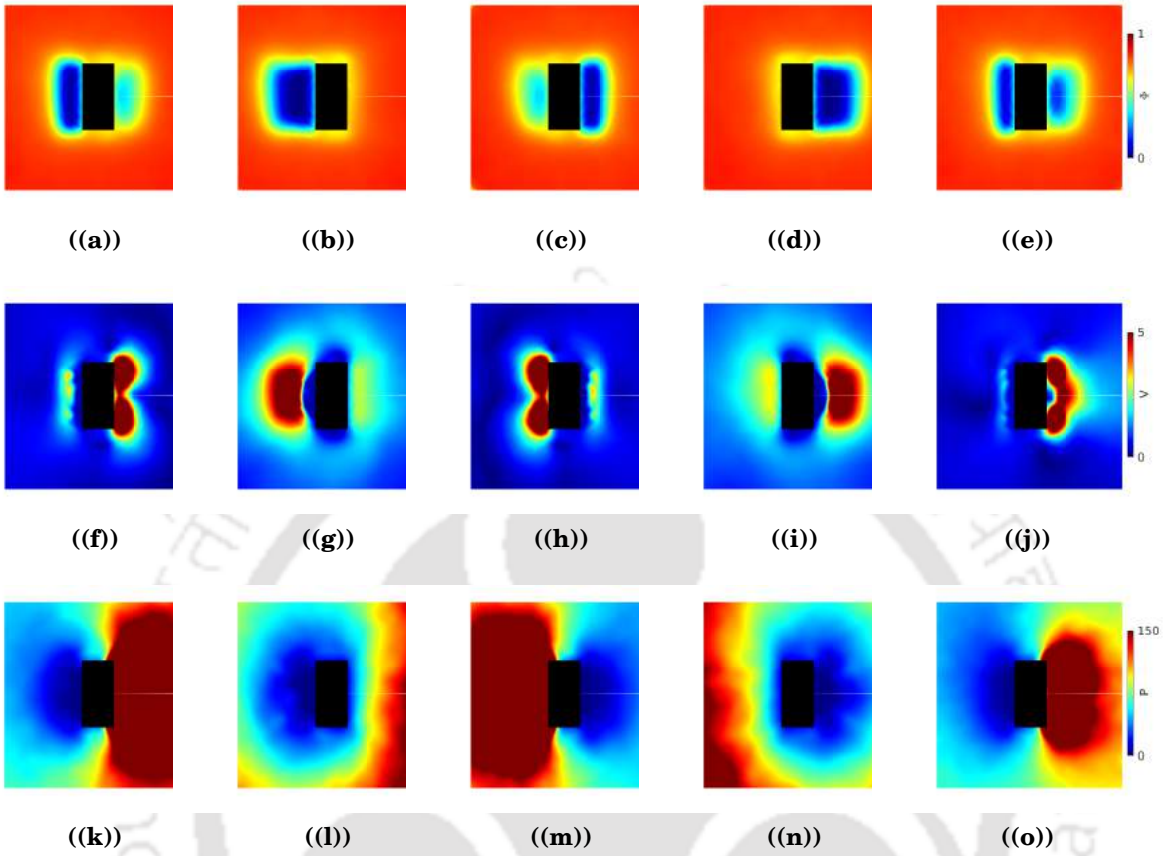

Figure 5.11: The time-averaged flow fields for depicting velocity V, pressure P, and area fraction Φ around the intruder $OS3$ (rectangle with its longer dimension along the y-axis) for $T/\sqrt{d/g} = 1$ and different phase angle ϕ : (a), (f), (k) 0.0, (b) (g), (l) 5.0, and (c), (h), (m) 10.0, (d), (i), (n) 15.0 and (e), (j), (o) 19.0. The oscillating amplitude of the intruder is $A/d = 3$.

left side of the intruder signifies the presence of another wake.

Figure 5.10 f illustrates velocity (V) fields when the intruder is at the centre point of oscillation ($10\phi/\pi = 0$). The velocity is maximum on the right side of the intruder as the particles move along with the intruder while it is moving from left to right. The velocity is minimum in the regions above and below the intruder as the particles in this region are negligibly affected by the intruder's movement. The velocity of the particles on the left side of the intruder is significantly less than that on the right side. The reason for this might be due to a mildly fluidized bed of particles as noticed in figure 5.10 a. As the intruder moves from the centre point of oscillation ($10\phi/\pi = 0$) to the rightmost ($10\phi/\pi = 15$), a large wake is developed to the left side of the intruder as shown in figure 5.10 b. The particles surrounding the wake try to fill it with larger velocities which

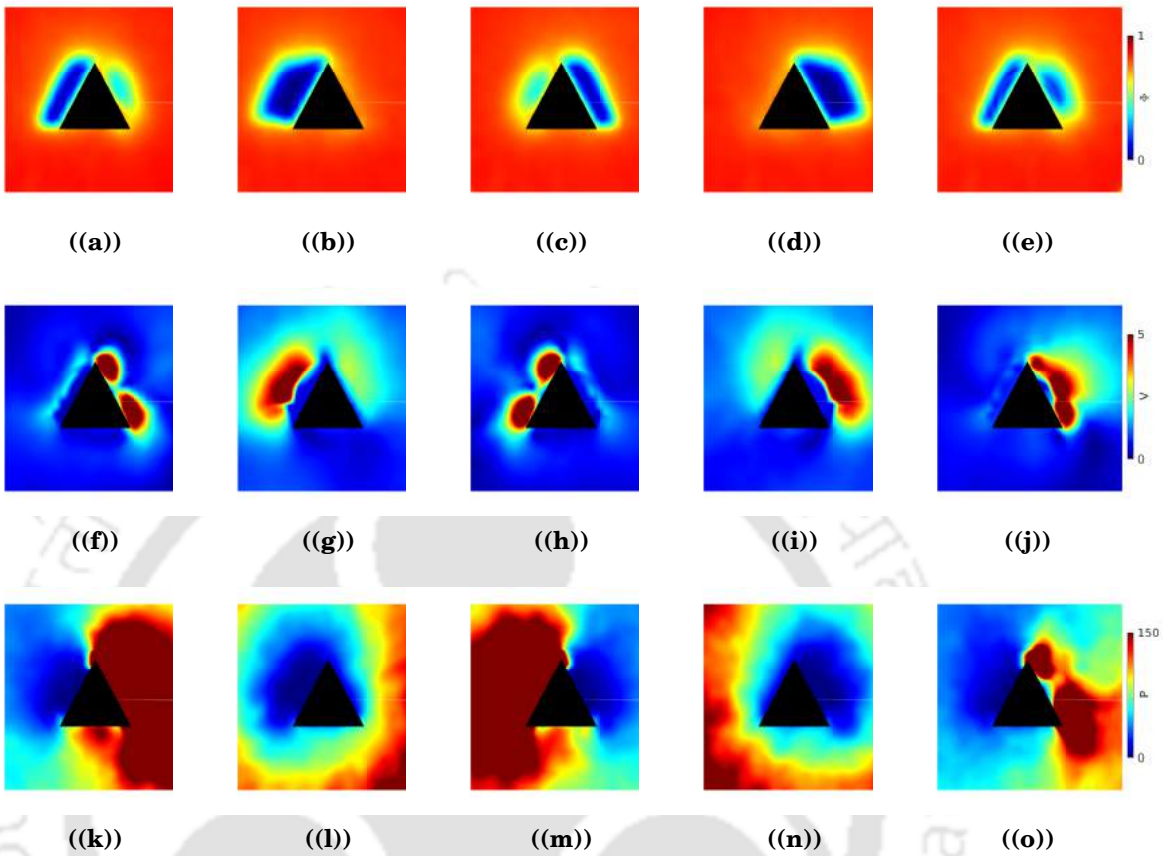

Figure 5.12: The time-averaged flow fields for depicting velocity V, pressure P, and area fraction Φ around the intruder $OS5$ (triangle) for $T/\sqrt{d/g} = 1$ and different phase angle ϕ : (a), (f), (k) 0.0, (b) (g), (l) 5.0, and (c), (h), (m) 10.0, (d), (i), (n) 15.0 and (e), (j), (o) 19.0. The oscillating amplitude of the intruder is $A/d = 3$.

are represented by a region of red to the left of the intruder(figure 5.10 g). When the intruder moves from right to left, it pushes the particles to move along with it. This can be evidenced in figure 5.10 h: the zones of red colour to the left of the intruder. Figure 5.10 i shows the velocity field when the intruder is at the leftmost point of oscillation. The particle velocities on the left side of the intruder are slightly lower because the intruder has started to move towards the right. The regions of red colour at a certain distance from the right surface of the intruder represents the particles that are trying to fill the wake that is formed between them and the intruder. As the intruder moves from left to right, the intruder pushes the particles lying to its left and hence a region of red colour is seen in figure 5.10 j ($10\phi/\pi = 19$).

Figure 5.10 k shows the pressure fields around the intruder when it is at the centre

position of oscillation ($10\phi/\pi = 0$). As the intruder is moving towards its right, greater pressure is noticed on the particles to the right. The zones of blue colour to the left of the intruder denotes the presence of wake. As the intruder starts to move towards its left after reaching the rightmost point ($10\phi/\pi = 5$) of oscillation, the pressure on the particles to its right is small (figure 5.10 l). To the left of the intruder, pressure is very less due to the presence of wake as noticed in figure 5.10 b. When the intruder reaches the centre position ($10\phi/\pi = 10$) from the right, the pressure is more to the left of the intruder (figure 5.10 m) as the intruder pushes the particles to its left while it is traversing. Figure 5.10 n shows the pressure when the intruder is at the leftmost point of oscillation. Very low pressure to the right of the intruder further confirms the presence of wake. Figure 5.10 o shows a greater pressure to the right of it as the intruder is moving towards its right.

Figure 5.11 shows the mean flow fields around a rectangle-shaped intruder with a small base length ($4.5d$) at different positions of oscillation. The wake region behind the rectangle-shaped intruder (figure 5.11 b and d) is larger than the disc-one (figure 5.10 b and d). The reason for this is the rectangle has a flat surface that pushes more particles while it is oscillating horizontally whereas, the disc with a curved surface can push fewer particles. Moreover, the y dimension length of the rectangle ($9.5d$) is larger than the diameter of the disc (7.0d). Due to the above-mentioned reasons, the regions of high velocities beside the wake are wider for the rectangle-shaped one (figures 5.11 g and i). The pressure fields are observed to be almost the same for both the disc-shaped and the rectangle-shaped intruders.

Figure 5.12 shows the mean flow fields of area fraction, velocity and pressure around an equilateral triangle-shaped intruder at different positions of oscillation. The pressure fields answer the question: why the triangle-shaped intruder has mostly a negative vertical displacement. Either of the two slant faces of the intruder experience a vertical component of stress pointing downwards during its entire oscillation except when it changes its direction of motion. This can be witnessed in figures 5.12 k, 5.12 m and 5.12 o.

5.3.6 Theoretical model

In a granular medium, a horizontal oscillation of an intruder might result in its vertical motion. Interestingly, this phenomenon has been utilized by a variety of organisms in nature to navigate through sand [3, 6]. However, this unique phenomenon has been

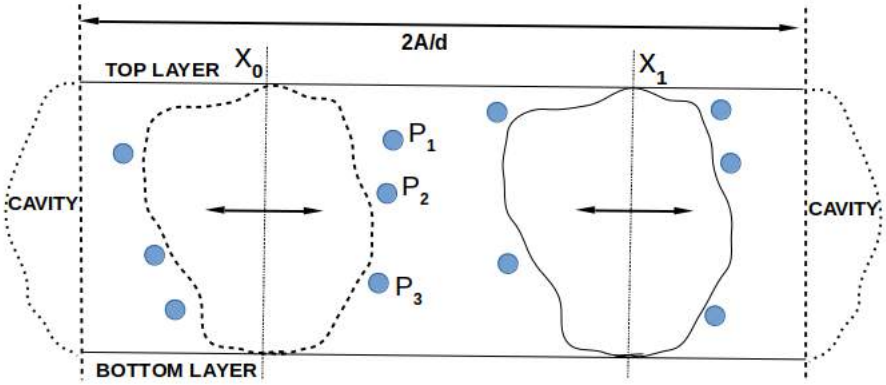

Figure 5.13: A general shape ocillating horizontally with granular particles around it.

poorly understood due to the granular media's complex behavior. Here, we propose a simple model to explain this phenomenon by horizontally oscillating an object in the granular medium. In this sense, our model explains both the intruder's rising and sinking behaviour at different oscillation parameters. A different mechanism governs the rising behaviour of the intruder as compared to that of its sinking behaviour. In this sense, the intruder's rising behaviour or upward movement presumably occurs as the intruder climbs up over a bed of particles that form at its bottom. Whereas the sinking behaviour happens due to the fluidization of the bed of particles below the intruder.

Firstly, we modeled the rising behaviour of the intruder by considering an arbitrary shape of the intruder and $(x, y) \in$ (collection of points on the surface). In the granular medium, its position in the x direction is defined as $x_{\text{cetre of mass}} = A\ sin(\omega t)$ (figure 5.13) owing to its horizontal oscillation. Now, if the orientation of an object is considered (with no rotational motion), then we can assign the axis such that $g = -|g|\hat{y}$ where $|g|$ is the magnitude of gravity. For the intruder to rise, we presume that an additional bed of particles has to form in front of the intruder at its bottom so that it climbs over it during its oscillation. To form this additional bed, the particles surrounding the intruder have to drop below a certain point as compared to the intruder's y position. This is termed a "point of no return" (y_{nr}), in a sense, if the particle's y position is below y_{nr}, it becomes the part of the additional bed of particles. Suppose, if the intruder is moving from X_0 to X_1 position and it is interacting with P_1, P_2 and P_3 particles (figure 5.13). As the intruder moves from X_0 to X_1 position, we can say that the particle P_3 will move down, whereas the particles P_1 and P_2 move upwards due to the intruder's shape. So, we can say that the "point of no return" is somewhere in between the P_2 and P_3 position. This

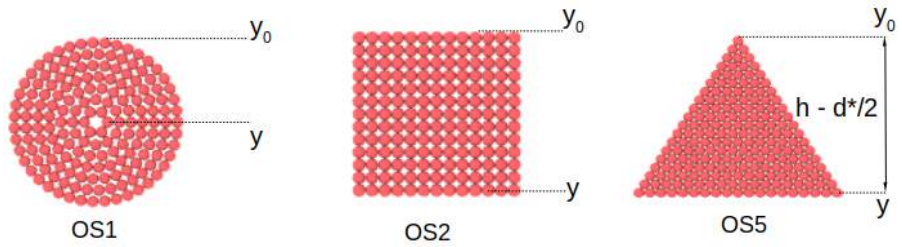

Figure 5.14: The shapes $OS1$, $OS2$ and $OS5$ with the points y and y^0 where the particles coving this distance of $(y - y^0)$ will fall beneath the base of the intruder.

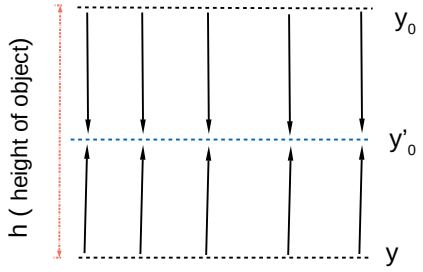

Figure 5.15: The height of the intruder object.

can be defined as

$$(x,y)_{\text{point of no return}} \in (x,y), \text{such that}: \frac{dy}{dx} = \infty \tag{5.1}$$

Therefore, any granular particle whose y coordinate is greater than the $y_{nr} = min(y_{\text{point of no return}})$ will eventually settle to the bottom of the intruder surface. Let us also consider, the vertical position of the top surface of the intruder as $y_0 = max(y_{such that \frac{dy}{dx}=0})$. Then, a particle situated above the intruder has to move at least $(y_{nr} - y_0 + \frac{d}{2})$ in one time period 'T' of oscillation to be a part of the additional bed at the bottom. If one were to focus on the one-half oscillations such that at $t = 0$, it exists at one end of the cavity, and at $t = T/2$, it exists on the other. The net-free fall into the cavity begins at t when the intruder has traveled time t forward, leading to a net free-fall time of 2t or a free-fall distance of $2gt^2$.

Net motion of particles that cross the point of no return when the intruder is at time t for a small-time dt,

$$dn = \frac{(2gt^2 - l - \frac{d}{2})4\phi}{\pi d^2} dx; \tag{5.2}$$

$$dn = \frac{(2gt^2 - l - \frac{d}{2})4\phi}{\pi d^2} \frac{2\pi A}{T} sin(\frac{2\pi t}{T}) dt; \tag{5.3}$$

Here, in equation (5.3), $l = y_{nr} - y_0$. Therefore, total particles reaching the bottom in one-half oscillation,

$$\int_0^N dn = \int_{\sqrt{\frac{l+\frac{d}{2}}{2g}}}^{T} \frac{(2gt^2 - l - \frac{d}{2})4\phi}{\pi d^2} \frac{2\pi A}{T} sin(\frac{2\pi t}{T}) dt; \tag{5.4}$$

$$N = \frac{4\phi 2\pi A}{\pi d^2 T} \int_{\sqrt{\frac{l+\frac{d}{2}}{2g}}}^{T} (2gt^2 - l - \frac{d}{2}) sin(\frac{2\pi t}{T}) dt; \tag{5.5}$$

$$N = \frac{4\phi 2\pi A}{\pi d^2 T} \int_{\sqrt{\frac{l+\frac{d}{2}}{2g}}}^{T} (2gt^2 - l - \frac{d}{2}) sin(\frac{2\pi t}{T}) dt; \tag{5.6}$$

Assuming $l' = l + \frac{d}{2}$,

$$N = \frac{T^2(g(1-\frac{2}{\pi^2})T - \frac{2l'}{T} - \frac{2}{\pi^2} gTcos[\frac{2\pi}{T}\sqrt{\frac{l'}{2g}}] - \frac{4g}{\pi}\sqrt{\frac{l'}{2g}} sin[\frac{2\pi}{T}\sqrt{\frac{l'}{2g}}])}{4\pi} \tag{5.7}$$

Therefore the rate of rise V_y can be given as:

$$V_y = \frac{4\phi 2\pi A}{\pi d^2 T} \frac{\pi d^2}{\frac{\phi 2AT}{2}} N; \tag{5.8}$$

$$V_y = \frac{8\pi}{T^2} N; \tag{5.9}$$

$$V_y = 2(g(1-\frac{2}{\pi^2})T - \frac{2l'}{T} - \frac{2}{\pi^2} gTcos[\frac{2\pi}{T}\sqrt{\frac{l'}{2g}}] - \frac{4g}{\pi}\sqrt{\frac{l'}{2g}} sin[\frac{2\pi}{T}\sqrt{\frac{l'}{2g}}]) \tag{5.10}$$

$$V_y = 2(0.7974T - \frac{2l'}{T} - 0.2026Tcos[\frac{2\pi}{T}\sqrt{\frac{l'}{2g}}] - 1.2732\sqrt{\frac{l'}{2g}} sin[\frac{2\pi}{T}\sqrt{\frac{l'}{2g}}]) \tag{5.11}$$

Shape	l or $(l^{'} - d/2)$	$T_{rising}(cavitymodel)$	$T_{rising}(observed)$
OS1	3.50	2.82	2.5-3.0
OS2	6.50	3.74	3.0-4.0
OS3	9.50	4.47	3.0-4.0
OS4	4.50	3.16	2.0-3.0
OS5	8.22	4.17	4.0-5.0

Table 5.2: Comparison between value of T_{rising} from theoretical estimate and the numerical simulations.

This equation describes V_y with respect to T for a given shape(fixed $l^{'}$). For $V_y > 0$, we get

$$T_{rise} = \sqrt{2l^{'}/g} \tag{5.12}$$

Additionally, V_y cannot increase indefinitely with T due to cavity filling up. At some $T_{rise} \approx \frac{(h-l)^2}{2g}$, it will start to decrease with

$$V_y \approx \frac{h-l}{T} \tag{5.13}$$

showing an inverse relationship with timeperiod (T) at higher T as observed in all the cases.

From Equa. 5.12 we can say that all the intruder oscillating above its critical timeperiod there is no sinking from its initial position. While for the rise of the intruder first of all a layer of particles should get accumulated beneath it. This is possible only when there is cavity formation due to the intruder oscillation. For this the intruder velocity should be such that the particles filling the cavity have enough time to fall down and settle. Thus creating a layer of particles that will help the intruder to climb up and lead to its rise. The maximum distance covered by the intruder during its oscillation is defined by its amplitude A and can be written as:

$$A \geqslant A_{min} \approx \alpha \frac{l}{\sqrt{2l/g}} = \alpha\sqrt{lg/2} \tag{5.14}$$

Here α is a numerical factor that is equal to 0.3. So, from the above equation it is clear that the intruder object cannot rise for velocity amplitude less than A_{min} even if the frequency is varried. In our simulations we have shown the A_{min} for all the

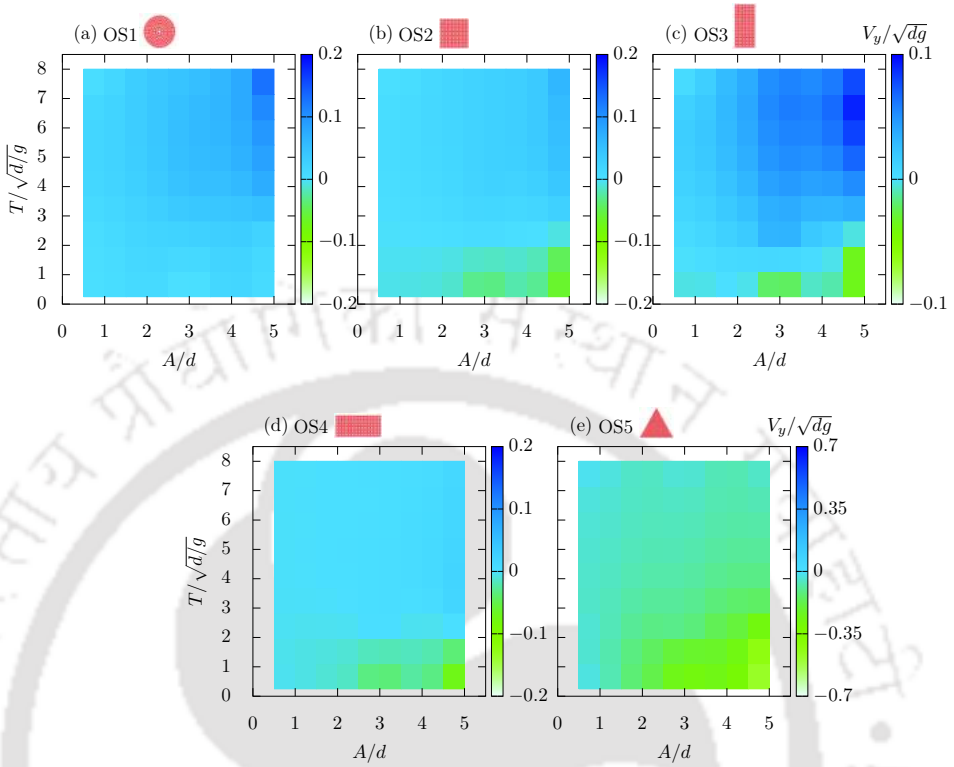

Figure 5.16: The colormap represents the rise rate V_y of the intruder(a) disc (b) square (c) narrow-rectangle and (d) wide-rectangle, and (e) triangle for all the oscillated T and A.

Shape	l or $(l^{'} - d/2)$	A_{min}
OS1	3.50	0.396
OS2	6.50	0.541
OS3	9.50	0.654
OS4	4.50	0.450
OS5	8.22	0.608

Table 5.3: Table showing the theoretical value of A_{min} for all the intruder shapes.

shapes in Table 5.3. This predicted values shown have been close enough with our simulations results. To have a more clear understanding of it we have shown the rise rate by colormaping it as a function of A and T in figure 5.16 for all the intruder shapes. The second mechanism works when the particles beneath the intruder supporting it becomes unstable due its motion and it sinks downward. For the particles to fluidize at the base of the intruder, they must be impacted with a sufficient force. The kinetic

energy the intruder have during its oscillation at a time t is the product of mass(M) amd acceleration $Acos(\omega t)$. So when the frequency of oscillation of the intruder is more it hits the particles surrounding it with higher force and disperse it to larger distance.

5.4 Conclusions

In this work, we analyzed the vertical dynamics of a horizontally oscillating intruder (various shapes considered) via a numerical simulation method. Depending on the oscillation amplitude and time-period, the intruder can rise, sink, or almost remain in its initial position.

5.4.1 Vertical displacement of oscillating intruder

The vertical displacement of the intruder is sensitive to its oscillation parameters. We found that the intruder object rises in the granular medium at a high time period and sinks when oscillated at a low time period for $A/d > 1$. However, the triangular intruder is observed to have a negligible rise even when it is oscillated at a high time period. The final vertical settling position of the intruder changes non-monotonically with the time period of oscillation.

5.4.2 Rate of rise or sink of intruder with time-period

The shape of the intruder has a significant influence on its rate of climb or sink within the granular medium. We observed a maxima and minima for the rate of rise and sink for all the intruder shapes. The rate of sink was found to to be the highest for $T/\sqrt{d/g} = 1$ for all the intruder shapes when oscillated at $A/d = 3$ and 5. Among all the shapes, we found that the disc ($OS1$) has the higher rate of rise, and triangle ($OS5$) has the higher rate of sink.

5.4.3 Average rate of vertical displacement of an intruder with phase angle

The average rate of vertical displacement of the intruder varies with phase angle (Figure 7). The phase angle $\phi = 0$ or $10\phi/\pi = 0$ represents the centre point of oscillation when the intruder is moving from left to right, $\phi = \pi/2$ or $10\phi/\pi = 5$ indicates the rightmost point

of oscillation. The V_y increases with ϕ where the intruder gradually climbs over the particles. While there is a gradual decrease in V_y at certain range of phase angle which can be attributed to more number of particles in the path of oscillating intruders providing a greater resistance and hampering the intruders positive vertical displacement.

5.4.4 Mean flowfields

The mean flow fields are reported for different phase angles around the intruder. The velocity field around the intruder shows that flow velocity is more on one side of the oscillating direction for the different phase angles. The pressure field around each intruder is asymmetric for different phase angles due to the wake formation. The area fraction field is observed to be less on one side and more on the other side due to the wake formation either to the left side of the intruder or to the right side, depending on its direction of motion. At the same time, the area fraction in the regions above and below the intruder is nearly equal to that of the bulk.

5.4.5 Theoretical Model

We developed a theoretical model to explain how intruders rise or sink within the granular medium when oscillated horizontally at a specific amplitude and time period. The model was able to identify a critical time period, below which an oscillating intruder will not rise. For all the intruder shapes, a point of no return was proposed; if the granular particle passes this point, it will reach the cavity's surface layer. These particles settling at the surface of the cavity will help the intruder climb on it and rise.

BIBLIOGRAPHY

[1] Abram H. Clark, Lou Kondic, and Robert P. Behringer. Particle scale dynamics in granular impact. *Phys. Rev. Lett.*, 109:238302, Dec 2012.

[2] Abram H. Clark, Alec J. Petersen, and Robert P. Behringer. Collisional model for granular impact dynamics. *Phys. Rev. E*, 89:012201, Jan 2014.

[3] Ryan D Maladen, Yang Ding, Chen Li, and Daniel I Goldman. Undulatory swimming in sand: subsurface locomotion of the sandfish lizard. *science*, 325(5938):314–318, 2009.

[4] David L. Hu, Jasmine Nirody, Terri Scott, and Michael J. Shelley. The mechanics of slithering locomotion. *Proceedings of the National Academy of Sciences*, 106(25):10081–10085, 2009.

[5] Ping Liu, Xianwen Ran, Qi Cheng, Wenhui Tang, Jingyuan Zhou, and Raphael Blumenfeld. Locomotion of self-excited vibrating and rotating objects in granular environments. *Applied Sciences*, 11(5):2054, 2021.

[6] Sarah S Sharpe, Yang Ding, and Daniel I Goldman. Environmental interaction influences muscle activation strategy during sand-swimming in the sandfish lizard scincus scincus. *Journal of Experimental Biology*, 216(2):260–274, 2013.

[7] Ryan D Maladen, Yang Ding, Paul B Umbanhowar, and Daniel I Goldman. Undulatory swimming in sand: experimental and simulation studies of a robotic sandfish. *The International Journal of Robotics Research*, 30(7):793–805, 2011.

[8] Ryan D Maladen, Paul B Umbanhowar, Yang Ding, Andrew Masse, and Daniel I Goldman. Granular lift forces predict vertical motion of a sand-swimming robot. In *2011 IEEE International Conference on Robotics and Automation*, pages 1398–1403. IEEE, 2011.

[9] Ling Huang, Xianwen Ran, and Raphael Blumenfeld. Vertical dynamics of a horizontally oscillating active object in a two-dimensional granular medium. *Phys. Rev. E*, 94:062906, Dec 2016.

[10] Liu Ping, Xianwen Ran, and Raphael Blumenfeld. Sink-rise dynamics of horizontally oscillating active matter in granular media: Theory. *arXiv preprint arXiv:2006.04160*, 2020.

[11] Peter A Cundall and Otto DL Strack. A discrete numerical model for granular assemblies. *geotechnique*, 29(1):47–65, 1979.

[12] Nikolai V Brilliantov, Frank Spahn, Jan-Martin Hertzsch, and Thorsten Pöschel. Model for collisions in granular gases. *Physical review E*, 53(5):5382, 1996.

[13] Leonardo E Silbert, Deniz Ertaş, Gary S Grest, Thomas C Halsey, Dov Levine, and Steven J Plimpton. Granular flow down an inclined plane: Bagnold scaling and rheology. *Physical Review E*, 64(5):051302, 2001.

[14] Steve Plimpton. Fast parallel algorithms for short-range molecular dynamics. *Journal of Computa-*

tional Physics, 117(1):1 – 19, 1995.

[15] Alexander Stukowski. Visualization and analysis of atomistic simulation data with OVITO-the Open Visualization Tool. *MODELLING AND SIMULATION IN MATERIALS SCIENCE AND ENGINEERING*, 18(1), JAN 2010.

CHAPTER 6

ROLE OF CONSTITUENTS OF A GRANULAR MEDIUM ON THE LIFT FORCE EXPERIENCED BY A TRANSLATING AND ROTATING INTRUDER.

6.1 Introduction.

Granular material is an assembly of discrete solid particles, and their interactions are dissipative [1, 2] in nature. There has been a lot of research on the rheology of spherical and almost spherical particles [3–6]. Food grains, catalyst pellets, and medicinal pills, for example, are generally non-spherical granular materials. Although many elements of the mechanics of non-spherical particles have been investigated in-depth, the rheology of such materials has not. The shape of the particles has an impact on the static and flow characteristics of granular materials. The understanding of flow behavior of shape heterogeneous mixture will be helpful in many industrial and natural processes such as mixing [7, 8], segregation [9, 10], advection and compaction [11, 12].

When a moving ball is spinning through the air, it gets deflected in the direction of spin due to the pressure difference on the opposite sides of the spinning ball. This phenomenon is known as the Magnus effect. It is believed that Newton was the first who gave explanation regarding this phenomenon in 1671 [13] while observing a tennis match in Cambridge college. Later, Benjamin Robins while working on the firing of a musket ball in the early part of 1742 [14] has explained the deviation of this musket ball

after firing in terms of the Magnus effect. After a century, in 1852, Heinrich Magnus gave a detailed explanation of the phenomena [15] and left his name to it.

The Bernoulli principle says that an increase in fluid speed happens concurrently with a drop in pressure for an inviscid flow and vice versa. The traditional Magnus effect on a spinning object has been explained in terms of a delayed separation on the retreating side when the spherical surface moves with the flow since the notion of the boundary layer was proposed by Prandtl in 1904 [16]. The flow separates further downstream on the advancing side (the spherical surface travels against the flow) than on the retreating side when the inverse Magnus effect occurs. Swanson using the boundary layer theory, described the circulation of airflow around the cylinder in his work [17]. He proposed that the top and lower boundary layers separate differently due to differing velocities and that this behavior causes circulation. With this, a friction-aware origin for the Magnus force was postulated, and the force's direction was explained.

It has also been observed that at certain Reynolds number the spinning ball is deflected opposite the direction of the usual Magnus effect [18–20]. Kim *et al.* [19] stated that this capricious behavior arises when the boundary layer flow traveling against the surface of a spinning sphere transition to turbulence, but the flow moving with the revolving surface stays laminar. Turbulence vitalizes the flow, causing the primary separation to occur further downstream, resulting in higher flow velocity and negative lift force. Whereas a circular object rotated in granular media, regardless of the area fraction, the direction of lift is opposite the direction of the general Magnus effect seen in viscous fluid [21]. The primary reasons for this type of lift generation in the granular medium are the tangential forces operating around the rotating intruder and the change in relative motion between the surrounding granules and the intruder due to the spinning.

The present work focuses on elucidating the role of constituent granules in the medium that affects the lift generation on a rotating and translating circular intruder. A mixture of dumbbells and discs is considered as a shape heterogeneous mixture.

6.2 Simulation Methodology

In this work, we employed the discrete element method (DEM) [22] to study the dynamics of a rotating spherical intruder moving through a mixture of dumbbells and discs. The DEM technique is explained in chapter 2. Initially an intruder of diameter D_i is placed at $x, y = 0$ inside a two-dimensional space ($x = \pm 150$ and $y = \pm 300$). The walls that confine

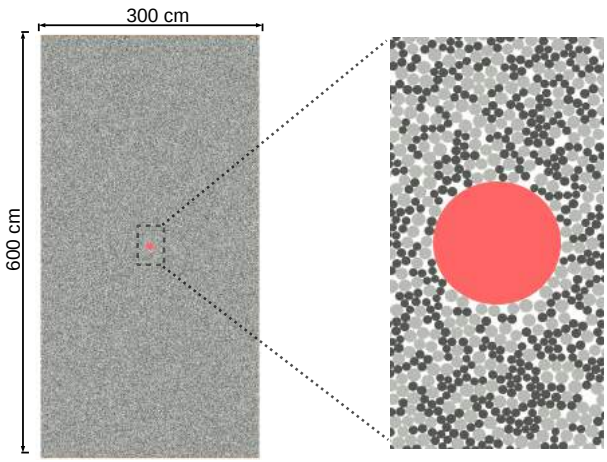

Figure 6.1: Initial configuration of our system with an intruder placed at a depth of $h = 300cm$ from the top wall. The granular mixture is comprised of dumbbells (black) and disc (grey) particles. At $y = \pm 300cm$, the system is confined by walls made of glued particles of size $1cm$ (orange), and periodic boundary conditions are applied in the x direction. The origin is located at the center of the intruder. In the right side of the figure the zoomed in region around the intruder is shown.

the simulation system along both the ends at $y = -300$ and $y = 300$ are made of particles of diameter 1.0cm. Please note that we packed $N_t = 100000$ (disc + dumbbell) to create a system of area fraction ϕ= 0.43. However, for the case of $\phi = 0.82$ ($N_t = 188000$), the confining walls are initially kept far away, such that the system will have a $\phi < 0.5$ with the desired number of randomly created particles. The walls are then moved very slowly towards the origin to make the system compact and attain the designated dimension of $300cm \times 600cm$. The system is further allowed to settle down for a certain time while the walls are kept stationary untill the kinetic energy of the entire system reach to zero. The disk particles has a mean diameter of $1cm$ and the dumbbell particles which are made by fusing two non-overlaping disk particles of mean diameter $0.7cm$. The distance from the top wall to the centre of the intruder is $h = 300cm$. The density is set as $\rho = 2gm/cm^2$. The boundary conditions in the x-direction are periodic. The intruder is moved at a constant velocity V_i along the positive x-direction for a total distance of $600cm$. The spin of the intruder is in the anticlockwise direction for all the simulations. The intruder diameter is kept at $5cm$ unless mentioned otherwise. Fig. 6.2 shows an initial configuration of the simulation system with the spherical intruder placed at the depth of $h = 300cm$ from the top wall. All the simulations were performed for a gravityless system. Table 6.1 lists the values of the parameters that are used in the

Simulation parameters	Values
K_n	$2.00 \times 10^{10} gm/cms^2$
K_t	$2.456 \times 10^{10} gm/cms^2$
γ_n	$80000(cms)^{-1}$
γ_t	$80000(cms)^{-1}$
$timestep$	$2 \times 10^{-6} s$
μ	0.5

Table 6.1: The parameters and its values used in our numerical simulations

simulations.

The simulation's run duration is the time taken by the intruder to travel a distance of $600cm$ at a particular velocity. A dumbbell's location and velocity are determined by its centre of mass position and centre of mass velocity. The sum of the forces and torques on a dumbbell's constituent particles is used to calculate the overall force and torque.

6.3 Results and Discussion

In this section, we will present the numerical results for an intruder rotating and translating through a mixture of dumbbells and discs. We studied five parameters namely: fraction of dumbbells X_{db}, area fraction ϕ, rotational velocity r_v, intruder velocity V_i and coefficient of friction μ.

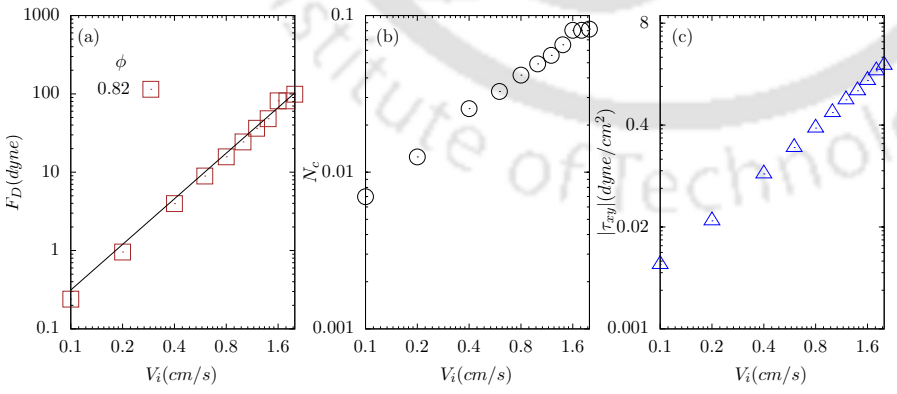

Figure 6.2: (a) Variation of drag force F_D with intruder velocity V_i for area fraction $\phi = 0.82$ on a log-log plot, (b) Variation of averaged particle contact N_c with V_i for $\phi = 0.82$, and (c) Variation of shear stress $|\tau_{xy}|$ with V_i for $\phi = 0.82$.

6.3.1 Translational and Rotational movement of the intruder

6.3.1.1 Dumbbell fraction

In this subsection, we analyzed the characteristics of intruder movement with and without rotational velocity (r_v) at various fractions of the dumbbell. In all our simulations the spin to the intruder is given in an anticlockwise direction. The drag force F_D is the force acting opposite to the direction of motion of the intruder. The intruder experiences drag due to particle contact N_c at its frontal surface in the direction of motion. To this purpose, we calculated the intruder's drag force (F_D), coordination number (N_c), and shear stress ($|\tau_{xy}|$) without no intruder rotational velocity as shown in Figure 6.2. The area fraction of the system is $\phi = 0.82$, the coefficient of friction is $\mu = 0.5$, and the diameter of the intruder is $D_i = 5\ cm$. The F_D and N_c correspond to their time-averaged values in this work. Note that the average does not contain a few values at the start of the simulation to avoid initial intermittencies. The averaged drag force F_D increases quadratically with the increase in intruder velocity at the given area fraction, as shown in figure 6.2(a). Takehera *et al.* [23, 24] in their studies have also found that the drag force has a V^2 dependence at high area fraction. The averaged number of particle contacts shown in figure 6.2(b) increases linearly with the increase in the intruder velocity. As it can be said, the drag force is directly dependent on the number of particle contact, with it increasing with an increase in the N_c. The shear stress on the intruder also linearly increases with the increase in the intruder velocity. The stress tensor σ_{ab} on i^{th} particle due to its N_p pair-wise interactions is calculated as $\sigma_{ab} = \frac{1}{2\times A}\Sigma_{j=1}^{N_p}(r_{i_a}F_{i_b} + r_{j_a}F_{j_b})$ where a and b take on x and y values to produce the components of the stress tensor. Here, r_{i_a} is the relative position of the i^{th} particle to the geometric center of the interacting particles, F is the force due to the pair-wise interaction, and A is the area of the i^{th} particle. The normal stress is calculated as $\sigma = -\frac{1}{2}(\sigma_{xx} + \sigma_{yy})$ and the shear stress is calculated as $\tau_{xy} = \sigma_{xy}$.

The role of a constituent particles in a granular medium on the drag and lift force experienced by rotating the intruder at varying r_v is shown in Fig 6.3. It is found that a symmetric body moving through a granular medium does not experience any net lift [25]. Nevertheless, when a rotational motion is added to the movement, it experiences a net lift force. The constituent particles also greatly enhance this lift generation, as found in our study. So understanding the forces on a simultaneously translating and rotating object can help the mechanisms related to the lift generation other than oscillation of

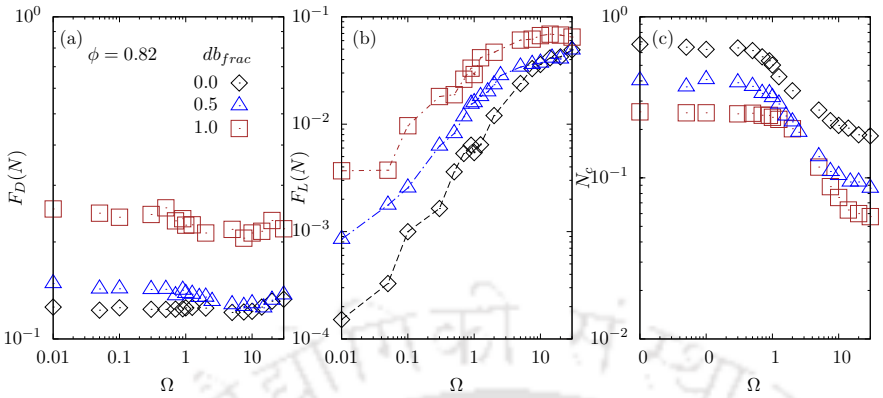

Figure 6.3: (a) Variation of drag force F_D with intruder spin ratio Ω for area fraction $\phi = 0.82$ on a log-log plot, (b) Variation of lift force F_L with Ω for $\phi = 0.82$ and (c) Variation of averaged particle contact N_C with Ω for $\phi = 0.82$.

an object or vibration of a system. When the intruder object in the granular medium has both translating velocity V_i and rotational speed r_v, then the lift is in a direction $-r_v \times V_i$, which is opposite to that in the fluids. We used a parameter that is defined as the spin ratio:

$$\Omega = \frac{r_v R}{V_i} \tag{6.1}$$

given by the ratio of the intruder's surface speed due to the rotation and its translational speed. This parameter is then used to compare results for various intruder velocities. In Fig 6. 3 (a), the mean drag force F_D on the intruder increases with an increase in system dumbbell fraction for different spin ratios Ω at $V_i = 25cm/s$. This is because, with the increase in the fraction of dumbbells, the chances of particle interlocking during contact may also increase, thus creating more resistance to the intruder movement. The lift force also increases with an increase in the fraction of dumbbells (Fig 6.3 (b)), and the intruder is found to experience ten times more lift force at low Ω in the range of 0.01 to 2 for $X_{db} = 1.0$ than $X_{db} = 0.0$, while at high Ω in the range of 10 to 25 the increase in F_L is twice for $X_{db} = 1.0$ than $X_{db} = 0.0$. It clearly shows that the constituent particle within the media with the rotational spin of the intruder help it to generate more lift than generally observed for normally translating and rotating object in disc-shaped granular media. The reason being that the dumbbell particles show better interlocking type of phenomena due to which they offer higher resistance to the spinning intruder. Since the intruder is spining there is a further increase in the frictional force on the intruder due to which an asymmetry is observed in the pressure experience on the intruder surface

which is otherwise not observed for a translating object in the granular medium. So this difference in the pressure between the upper and lower half of the intruder results in the net lift force being experienced by the intruder and has been shown in the pressure field around the intruder in figure 6.13, 6.14, 6.15. The average particle contacts N_c with intruder also increase with the fraction of dumbbell for different intruder spin ratios, as shown in Fig 6.3 (c). Though there is a decrease in the N_c is after a certain spin ratio for all X_{db}.

In figure 6.4(a), the variation of the ratio of mean lift (F_L) to mean drag (F_D) as a function of spin ratio Ω for intruder velocities V_i (a) $1cm/s$, (b) $5cm/s$, (c) $25m/s$ and (d) $100cm/s$ and different X_{db} is shown. It is observed that the F_L/F_D saturates after a certain value of Ω and have almost a constant value in the higher range of the spin ratio. The increase in F_L/F_D is significant after $\Omega \approx 1$ until $\Omega \approx 10$ for high velocities of $25cm/s$ and $1m/s$, and then it gradually saturates. Sonu *et al* [21] in their work have developed a model which states that the $F_L/F_D = \mu$ and follows a linear relationship with μ at low area fraction and deviates at higher area fraction ϕ. We have also compared our results in Figure 6.5 with the suggested model for a system with $X_{db} = 0.5$ and found that the F_L/F_D ratio deviates as the area fraction of the system increases and follows a linear relationship with μ at low ϕ. So it suggests that irrespective of the nature of constituent particles in the granular medium the model works. Figure 6.6 shows the variation of mean drag $F_{D\Omega}$ and the average number of particle contact $N_{C\Omega}$ normalized by the corresponding values at $\Omega = 0$ as a function of Ω. For the intruder velocity $V_i = 0.25m/s$ the $F_{D\Omega}/F_{D\Omega=0}$ is almost constant at low area-fraction with little variation observed for $\phi = 0.82$ at high spin ratio values. The averaged number of particle contact N_C (figure 6.6 (c), (d) and (e)) decreases after a certain Ω for all the intruder velocities and then gets saturated.

The drag on the intruder is the component of the sum of forces acting opposite to its direction of movement due to the particle in contact. So the drag on the intruder is directly proportional to the particle in contact; however, this only applies when the force per contact is the same in all the cases. This will be further elaborated in the study of force distribution on the intruder due to particle contact in Section 6.3.3.

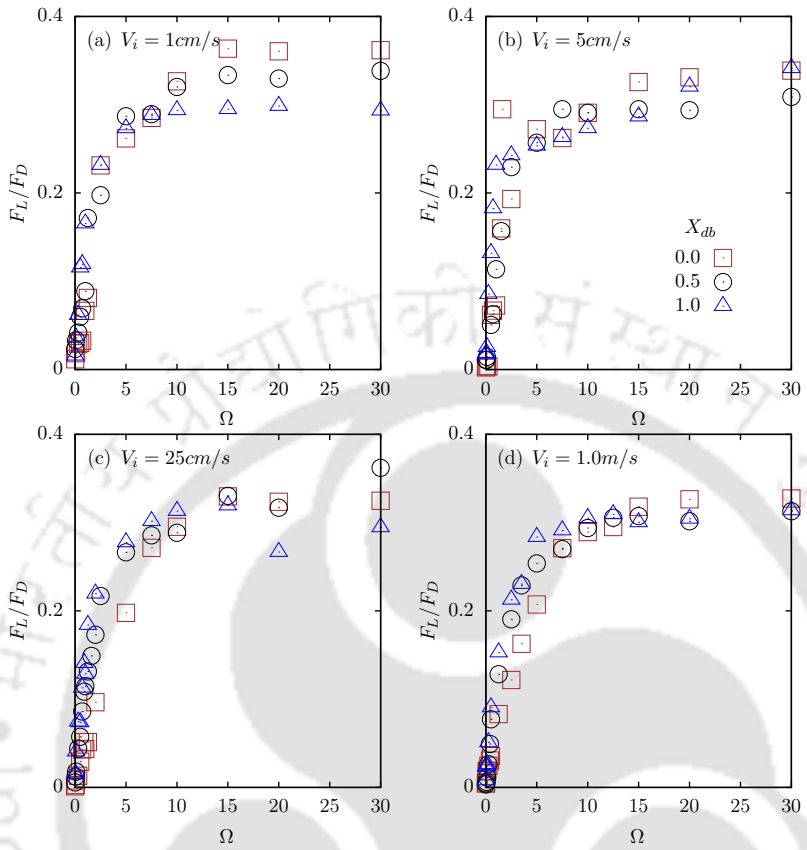

Figure 6.4: The lift to drag force ratio F_L/F_D vs spin ratio ($\Omega = r_o R/V_i$) for different intruder velocities V_i (a)$1cm/s$, (b) $5cm/s$, (c) $25cm/s$ and, (d) $100cm/s$ and three different dumbbell fraction X_{db} of 0.0, 0.5 and 1.0, with system area fraction ϕ=0.82.

6.3.2 Area fraction

In this subsection, we studied the effect of area-fraction ϕ of the system on the dynamics of a rotating and translating intruder at various fractions of dumbells X_{db}. For the analysis, we have considered two area fractions ϕ = 0.43 and 0.82 with particles 100000 and 188000 having the same system dimensions. Figure 6.7 shows the variation on the mean lift and mean drag ratio as a function of Ω for $V_i = 25cm/s$, x_{db} = 0.0, 0.5 and 1.0. The trend for the F_L/F_D ratio is similar for both the dilute ($\phi = 0.43$) and dense ($\phi = 0.82$) systems. When the angular velocity r_v of the intruder is 0, that is $\Omega = 0$ we observe that the F_L/F_D value is almost zero, which is due to the symmetry in the amount of drag force that the intruder experiences at its upper and bottom half in the direction of

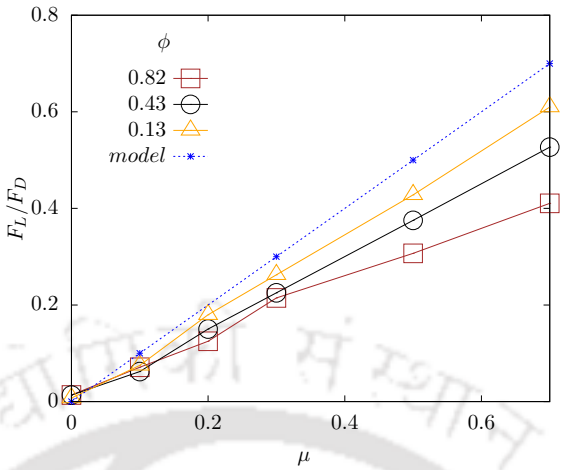

Figure 6.5: F_L/F_D as a function of friction coefficient μ for various ϕ. The more dilute the system is, the closer the value of F_L/F_D to the proposed model.

motion. While at higher Ω, the F_L/F_D saturates, having almost a constant value. This saturation in the F_L/F_D value is due to the particles slipping around the intruder surface at a higher spin ratio. We also observe that the F_L/F_D value increases with X_{db} in the Ω range of 0.5 to 8 for both the $\phi's$. So it can be stated that when the intruder is given a certain rotational velocity, it experiences a lift force even for a low area fraction system.

In Figure 6.8, the drag $F_{D\Omega}$ and the averaged number of particle contacts $N_{c\Omega}$ as a function of Ω normalized by the drag and contact value at $\Omega = 0$ is shown. The drag is observed to be constant at low area fraction$\phi = 0.43$ for the given Ω while there is an increase in drag at a higher value of Ω for $\phi = 0.82$. The number of contact $N_{C\Omega}/N_{C\Omega=0}$ decreases after a certain spin ratio for both the dilute and dense systems. Figure 6.9 shows the mean drag and lift force as a function of μ for $\phi = 0.43$, and 0.82, $V_i = 25cm/s$, $X_{db} = 0.5$ and $\Omega = 20$ respectively. The drag force increases as the system's ϕ and μ increase. This may be rationalized in a dilute and denser environment by considering the concurrent influence of frictional forces and the growth of force chains. Frictional forces are only visible in granular material when the particles are in contact. A dilute system has fewer particle interactions than a denser medium. As the area fraction of the system increase, so do the frictional forces. Furthermore, when the area fraction increases, the possibilities of force chains evolving in the structure of particles in front of the intruder increases. The lift force (Figure 6.9 b) also increases with the increase in the ϕ and μ of the contacting particles.

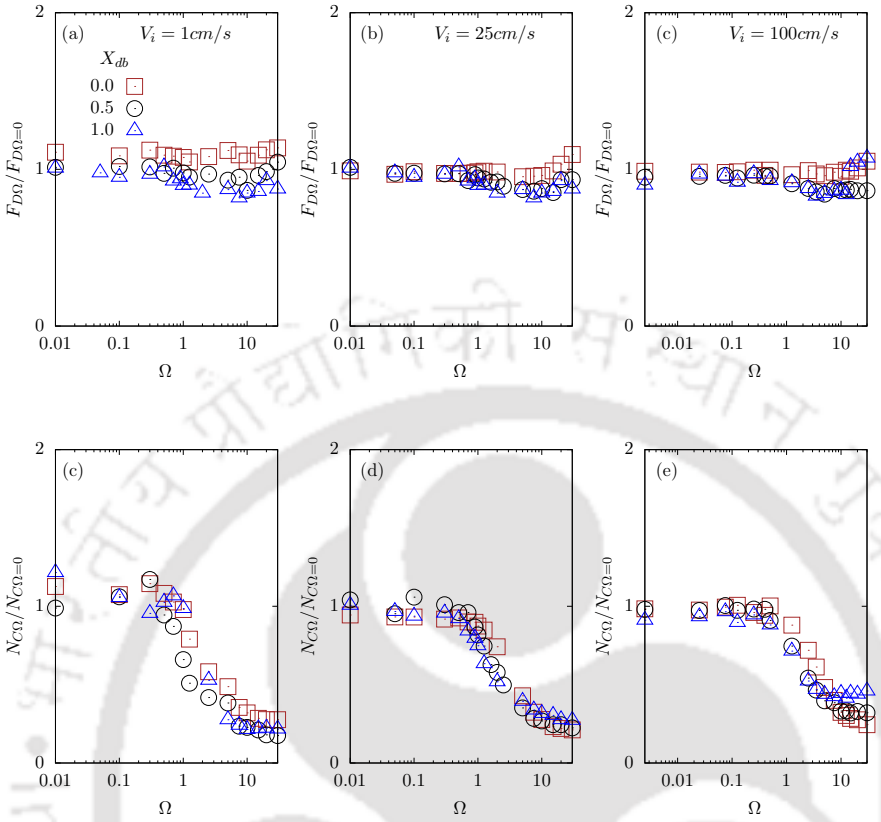

Figure 6.6: The drag force at a certain spin ratio $F_{D\Omega}$ normalized by the drag force at spin ratio of zero $F_{D\Omega=0}$ as a function of Ω for db_{frac} ranging from 0.0 to 1.0 for different intruder velocities U_i (a) $1cm/s$, (b) $25cm/s$, and (c) $100cm/s$. The $N_{C\Omega}/N_{C\Omega=0}$ as a function of Ω for various X_{db} and intruder velocities V_i (a) $1cm/s$, (b) $25cm/s$, and (c) $100cm/s$. The system has an area fraction ϕ of 0.82 and $\mu = 0.5$.

6.3.3 Force distribution around the intruder

In this subsection, we calculated the force distribution as a function of the angle of contact θ, relative to the intruder's center, to better understand the forces operating around the perimeter of the intruder during its rotation and translation within the granular medium. The region around the intruder is divided into two halves, with the top half corresponding to θ 0° to 180° and the bottom half referring to θ 0° to −180°.

Figure 6.10 and 6.11 shows the time-averaged total drag force normalized by the drag force on the intruder with no rotational velocity ($\omega = 0$) i.e $F_{D\Omega=0}$ and the total number of particle contact on the intruder surface normalized by $N_{C\Omega=0}$ for area fraction $\phi = 0.82$, $mu = 0.5$ and X_{db} 0.0 and 1.0. In Fig. 6.10 (a), the drag on the intruder is observed to be maximum at the frontal part for $\theta = \pm 90°$ whereas in the rear side of the intruder

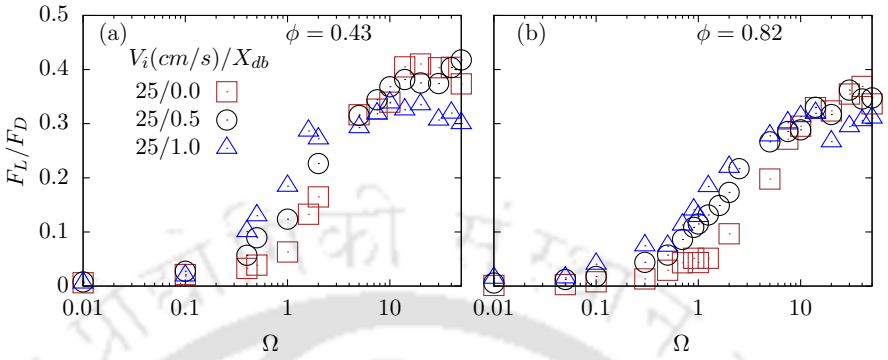

Figure 6.7: The lift to drag force ratio F_L/F_D vs spin ratio ($\Omega = r_o R/V_i$ for $V_i = 25cm/s$ and dumbbell fraction X_{db} 0.0 to 1.0 with system area fraction ϕ= (a)0.43, and (b) 0.82 in a semi-log plot.

with $\theta \geq 90°$ and $\theta \leq \pm 90°$ it is negligible. This is because of the wake formation behind the intruder as it moves within the granular media due to which there is no particle contact at the rear side of the intruder and is also evident with the number of particle contact being zero in that region as shown in Fig. 6.13 (b). The same is observed for the system with $X_{db} = 1.0$ where the drag force is high at $\theta = \pm 90°$ as most of the particle contact is in that region of the intruder surface. Though the magnitude of drag force on the intruder in the system $X_{db} = 1.0$ is higher than that of $X_{db} = 0.0$. This can be due to the reduction in the frequency of force-chain buckling occurrences in the media as the fraction of dumbbell increases. Aside from inter-particle friction, the shape of the particles in front of the intruder also signifcantly contributes to the amount of stress or drag force it experiences [26]. As it has also been explained in chapter 4 that the system with only dumbbell particles may have a higher interlocking capability contributing to the higher amount of drag force experienced by the intruder object.

In Figure 6.12, the time-averaged tangential force acting on the intruder surface as a function of θ is shown. At a higher spin ratio, it can be observed that the $F_{t,\theta}$ has a different direction in comparison to a system having $\Omega = 0$. For $\Omega = 10$, the tangential force is more on the frontal part of the intruder $\theta \approx \pm 90°$, while at high $\Omega = 20$ the $F_{t,\theta}$ is observed at most of the contact region of the intruder surface. This suggests that at a higher value of the spin ratio, there is slipping of particles and also explains the saturation in the lift and drag ratio.

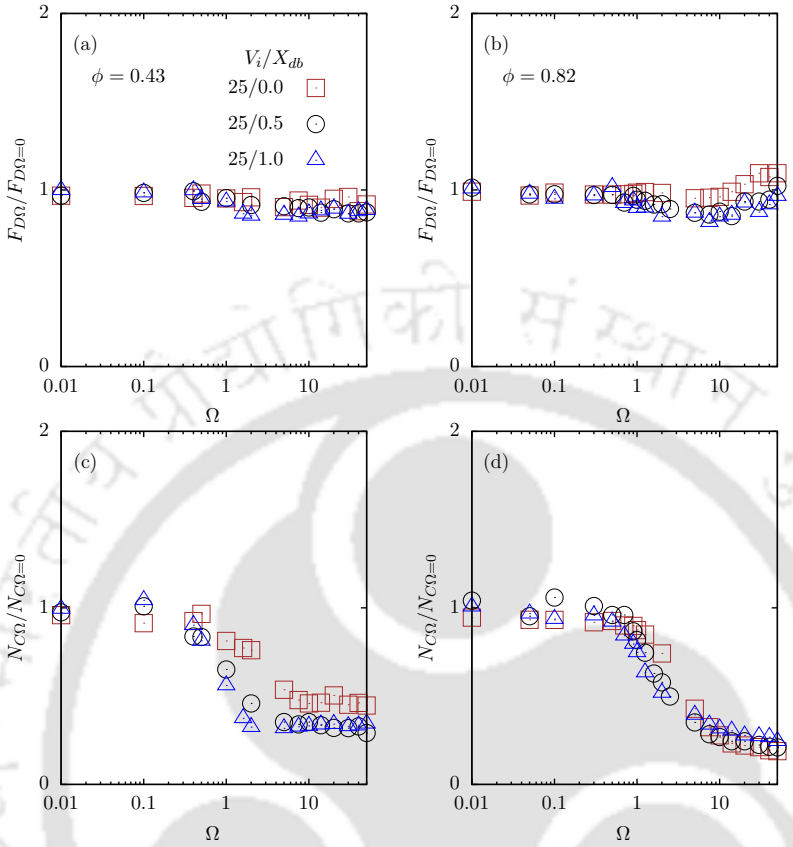

Figure 6.8: The drag force at a certain spin ratio $F_{D\Omega}$ normalized by the drag force at spin ratio of zero $F_{D\Omega=0}$ as a function of Ω for db_{frac} ranging from 0.0 to 1.0 and ϕ = (a) 0.43 and (b) 0.82. The $N_{C\Omega}/N_{C\Omega=0}$ as a function of Ω for various X_{db} and ϕ = (c) 0.43 and (d) 0.82.

6.3.4 Mean flowfields around the intruder

We produced the time-averaged flow fields using discrete microscopic data such as velocities, locations, stress, and other parameters of each particle in a defined area surrounding the intruder. The Gaussian coarse-graining function, as implemented by Glasser and Goldhirsch[27], is used to calculate the parameters at various spatial locations. The area fraction $\phi(t)$, velocity $v(t)$, stress tensor $\boldsymbol{\sigma_{ij(t)}}$, and pressure $P(t)$ are computed at a spatial point p using a position vector $\boldsymbol{r_p}$ and an arbitrary time t as follows:

$$\phi(t) = \left[\sum_{i=1}^{n} \frac{\rho \pi d_i^2}{4} \mathcal{W}(\boldsymbol{r_p} - \boldsymbol{r_i(t)}) \right] / \rho \tag{6.2}$$

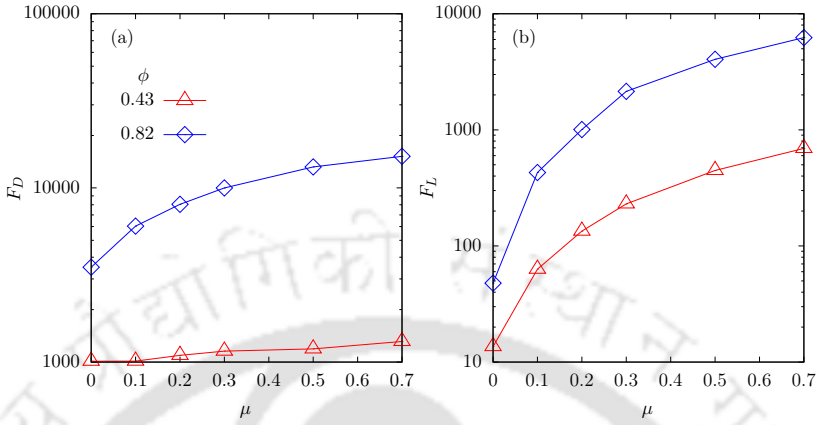

Figure 6.9: The mean (a) drag force F_D and (b) lift force F_L as a function of friction coefficient for $\phi = 0.43$ and 0.82, $V_i = 25cm/s$, $X_{db} = 0.5$ and $\Omega = 20$

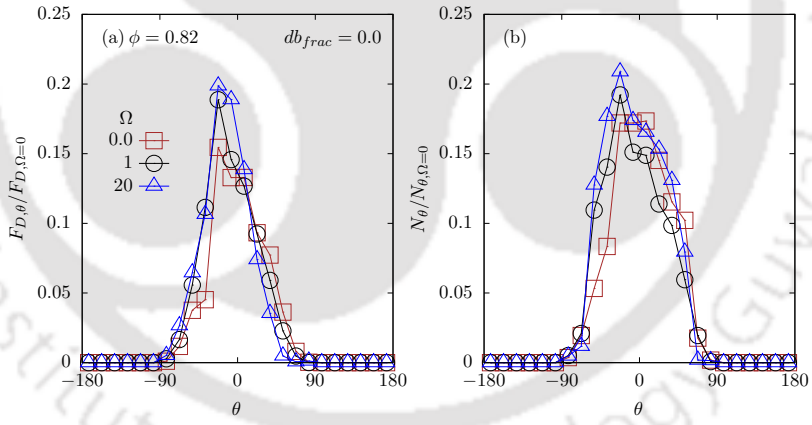

Figure 6.10: The distribution of drag force (a) $F_{D\Omega}/F_{D\Omega=0}$ and number of particle contact (b) $N_{C\Omega}/N_{C\Omega=0}$ as a function of its contact angle θ around the intruder surface for fraction of dumbbell $X_{db} = 0.0$ and $\phi = 0.82$.

$$\boldsymbol{v}(t) = \left[\sum_{i=1}^{n} \frac{\rho\pi d_i^2}{4} \boldsymbol{v_i} \mathcal{W}(\boldsymbol{r_p} - \boldsymbol{r_i(t)})\right] / \rho\phi \tag{6.3}$$

$$\boldsymbol{\sigma_{ij}}(t) = \sum_{i=1}^{n} \sum_{j=i+1}^{n} (\boldsymbol{F^{ij}} \boldsymbol{r_{ij}}) \int_{s=0}^{1} \mathcal{W}(\boldsymbol{r_p} - \boldsymbol{r_i(t)} + s\boldsymbol{r_{ij}}) ds \tag{6.4}$$

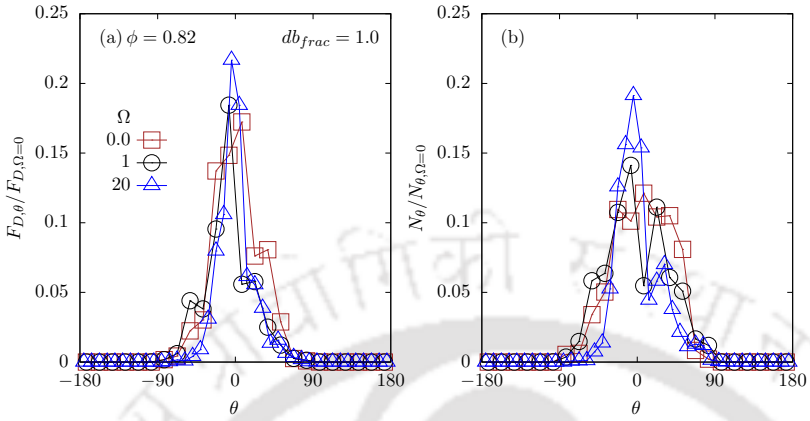

Figure 6.11: The distribution of drag force (a) $F_{D\Omega}/F_{D\Omega=0}$ and number of particle contact (b) $N_{C\Omega}/N_{C\Omega=0}$ as a function of its contact angle θ around the intruder surface for fraction of dumbbell $X_{db} = 1.0$ and $\phi = 0.82$.

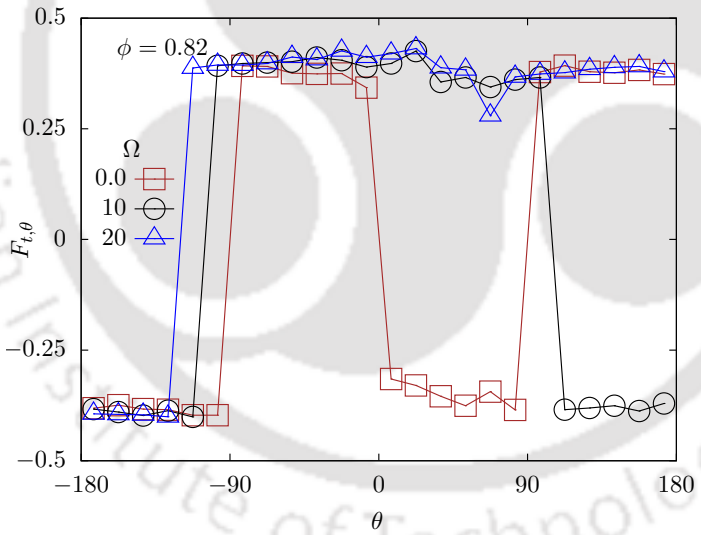

Figure 6.12: The distribution of tangential force $F_{t\theta}$ as a function of its contact angle θ around the intruder surface for fraction of dumbbell $X_{db} = 1$ and $\phi = 0.82$.

$$P(t) = \frac{-tr(\sigma_{ij}(t))}{2} \tag{6.5}$$

$$\mathcal{W}(\boldsymbol{r}) = \frac{1}{\pi w^2} e^{-\boldsymbol{r}^2/w^2} \tag{6.6}$$

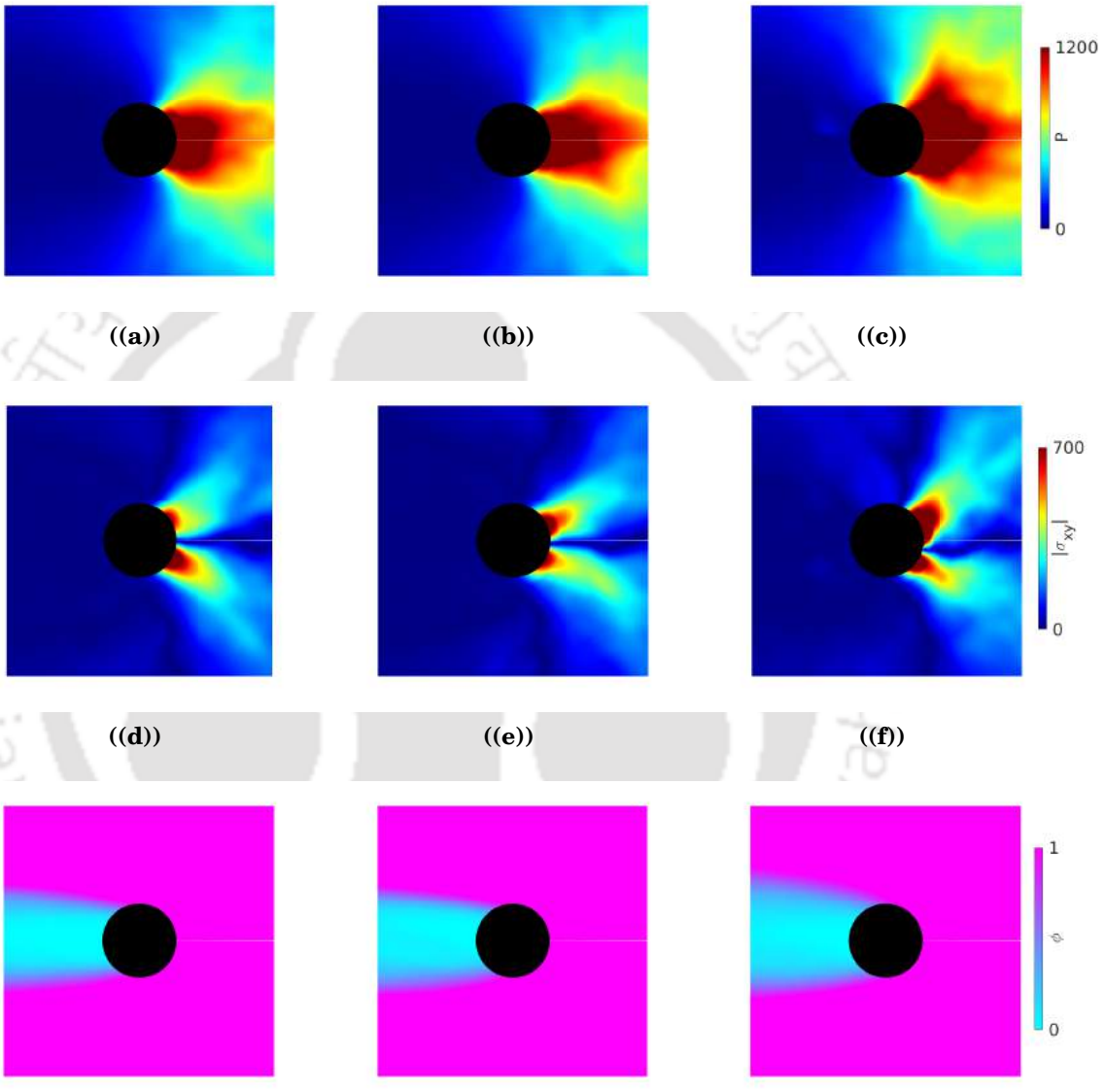

Figure 6.13: The time-averaged flow fields for depicting pressure P, shear stress $|\sigma_{xy}|$ and area fraction ϕ infront of the intruder for different spin ratio (Ω): (a), (d), (g) 0.0, (b) (e), (h) 1.0 and (c), (f), (i) 10.0. The velocity of the intruder is $V_i = 25cm/s$ and the fraction of dumbbell (X_{db}) in the system is 0.0.

Here, the coarse-graining function is $\mathscr{W}(\boldsymbol{r})$, and the density, diameter, and position vector of the particle i are ρ, d_i, and $\boldsymbol{r_i(t)}$. The force exerted on particle i by particle j is $\boldsymbol{F^{ij}}$, and $\boldsymbol{r_{ij}}$ is a vector pointing in the direction of the line connecting the centres of two particles i and j. In addition, $w = 1.0$ and $\mathscr{W}(\boldsymbol{r_p - r_i}) = 0$ if $|\boldsymbol{r_p - r_i}| > 3w$ and $\phi, \boldsymbol{v}$ and P are the time-averaged area fraction, velocity, and pressure, respectively. The flow fields presented are averaged over a minimum of 5000 frames and correspond to a circular area of $20cm$ radius from the intruder's centre ($D_i = 5\ cm$).

In Fig. 6.13 we have shown the flow fields depicting the pressure P, shear stress σ_{xy} and area fraction ϕ in the vicinity of the intruder during its movement for $V_i = 25cm/s$, $\mu = 0.5$ and $X_{db} = 0.0$. Figures 6.13 (a),(b), and (c) shows the pressure field around the intruder surface for spin ratio Ω = 0,1 and 10. The pressure is observed to be symmetric at $\Omega = 0$, but at high $\Omega = 10$, it is found to be asymmetric with the pressure on the intruder being higher at the upper side of the intruder, as shown in Fig. 6.12 (c). This is due to the intruder's high rotational velocity, making the pressure non-uniform and more on one side of the intruder. It is also evident by the mean flow field of shear stress $|\sigma_{xy}|$ for different Ω shown in Figures 6.13 (e), (f), and (g). The particles whose y position is almost identical to the intruder's y location do not take a detour around it but instead move forward with it. At y = (0,0), there is no shear stress as a result of this. Other than the particles stated above, particles near the intruder's front surface are compelled to detour around it due to its mobility. This causes relative motion between the contacting particles on the intruder's surface. As a result, these particles, which correspond to the deep red zones, are subjected to significant shear stress. However, this phenomenon is not noteworthy at a distance from the intruder because there is little relative motion between them. While at high $\Omega = 10$, the magnitude of $|\sigma_{xy}|$ of shear stress is more on the advancing (upper half of the intruder) side than on the retreating side(lower half of the intruder) of the intruder. The area fraction around the intruder is shown in Figures 6.13 (g), (h), and (i) for Ω = 0, 1 and 10. The wake observed at the rear end of the intruder during its movement within the granular medium increases with the increase in the Ω. As in the wake region, the ϕ is almost zero with no particle in it, while the region around the intruder other than the wake region has an area fraction as that of the system.

Further, Figs 6.14 and 6.15 shows the time-averaged pressure, shear stress, and area fraction around the intruder for $X_{db} = 0.5$ and 1.0. We have observed that with the increase in the fraction of dumbbells, the magnitude of pressure has also increased, as observed in Figures 6.15 (a), (b), and (c) as compared to the pressure in the vicinity of the

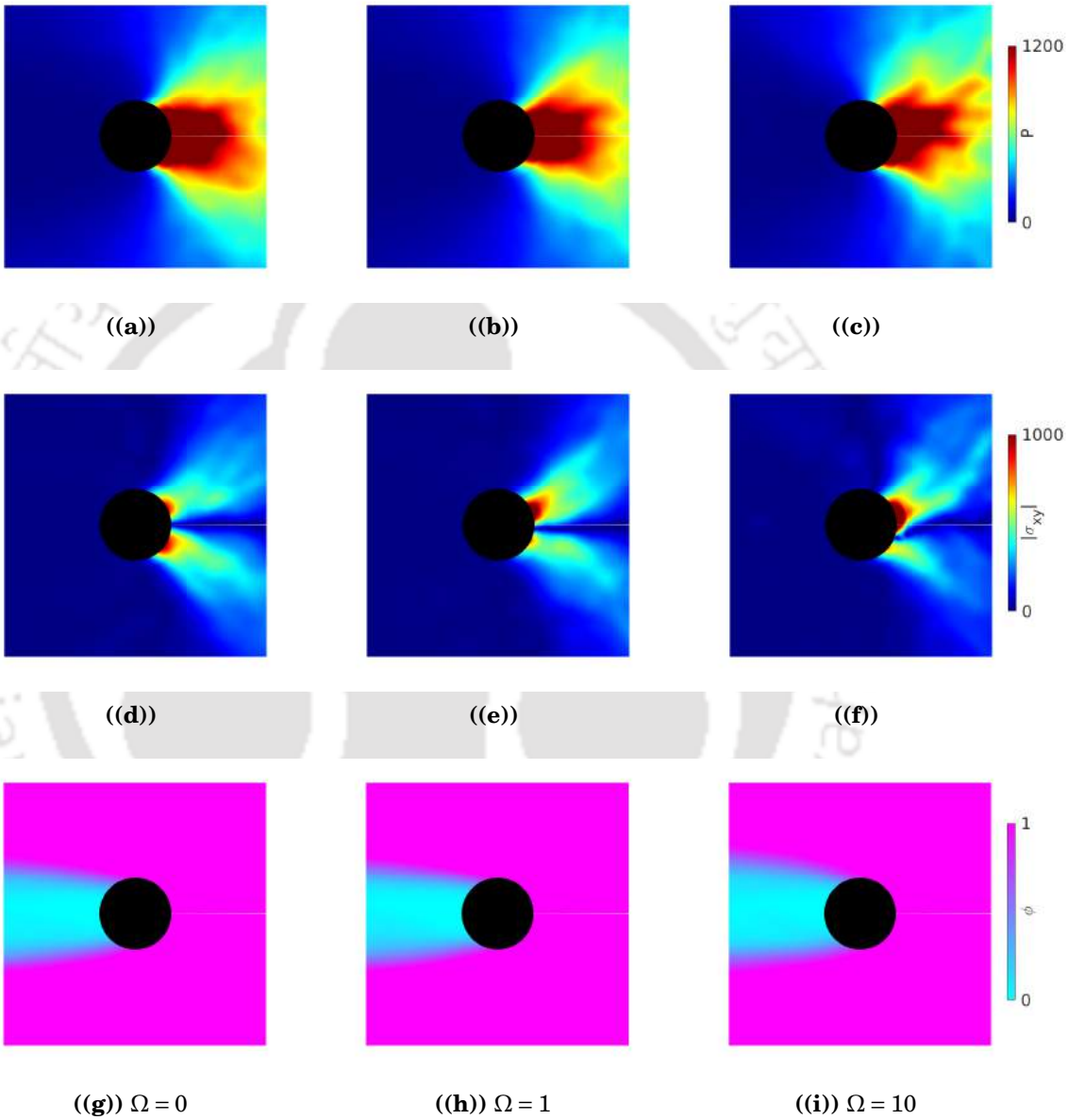

Figure 6.14: The time-averaged flow fields for depicting pressure P, shear stress $|\sigma_{xy}|$ and area fraction ϕ infront of the intruder for different spin ratio (Ω): (a), (d), (g) 0.0, (b) (e), (h) 1.0 and (c), (f), (i) 10.0. The velocity of the intruder is $V_i = 25cm/s$ and the fraction of dumbbell (X_{db}) in the system is 0.5.

intruder for $X_{db} = 0$ (Figures 6.13 (a) to (c)). It is observed that the intensity of pressure infornt of the intruder seems to gradually decrease as it moves away from the intruder surface in the direction of mmotion, which is due to the contacting particles sliding away from the cluster of particles rather than clinging to it up to a greater distance. In figures 6.15 (d) to (f), it is evident that with the increase in the spin ratio, the magnitude of shear stress becomes more on one side of the intruder, thereby creating a pressure difference between the lower and upper region of the intruder surface. This finally leads to the intruder's deviation from its original path, and a Magnus effect is observed opposite to the direction of spin. The wake region is also observed to widen with the increase in the spin ratio as shown in figures 6.15 (g) to (i) for the distribution of area fraction around the intruder.

6.4 Conclusions

We analysed the dynamics of a simultaneously rotating and translating intruder in a heterogeneous mixture of dumbbells and discs. The direction of the lift force is found to be -$r_v \times V_i$, which is opposite to the generally observed direction in fluids. The rotation of the intruder creates a change in the direction of relative motion between the intruder and the surrounding granular particles, due to which a lift is generated. We found that the lift force on the intruder increases with an increase in the fraction of dumbbells for its given spin ratio. We found that even at a very low intruder velocity of $V_i = 1cm/s$, there was lift generation on the intruder at a given spin ratio. For both the dilute and dense granular systems, we observe that the intruder experiences net lift force at a given rotational velocity.

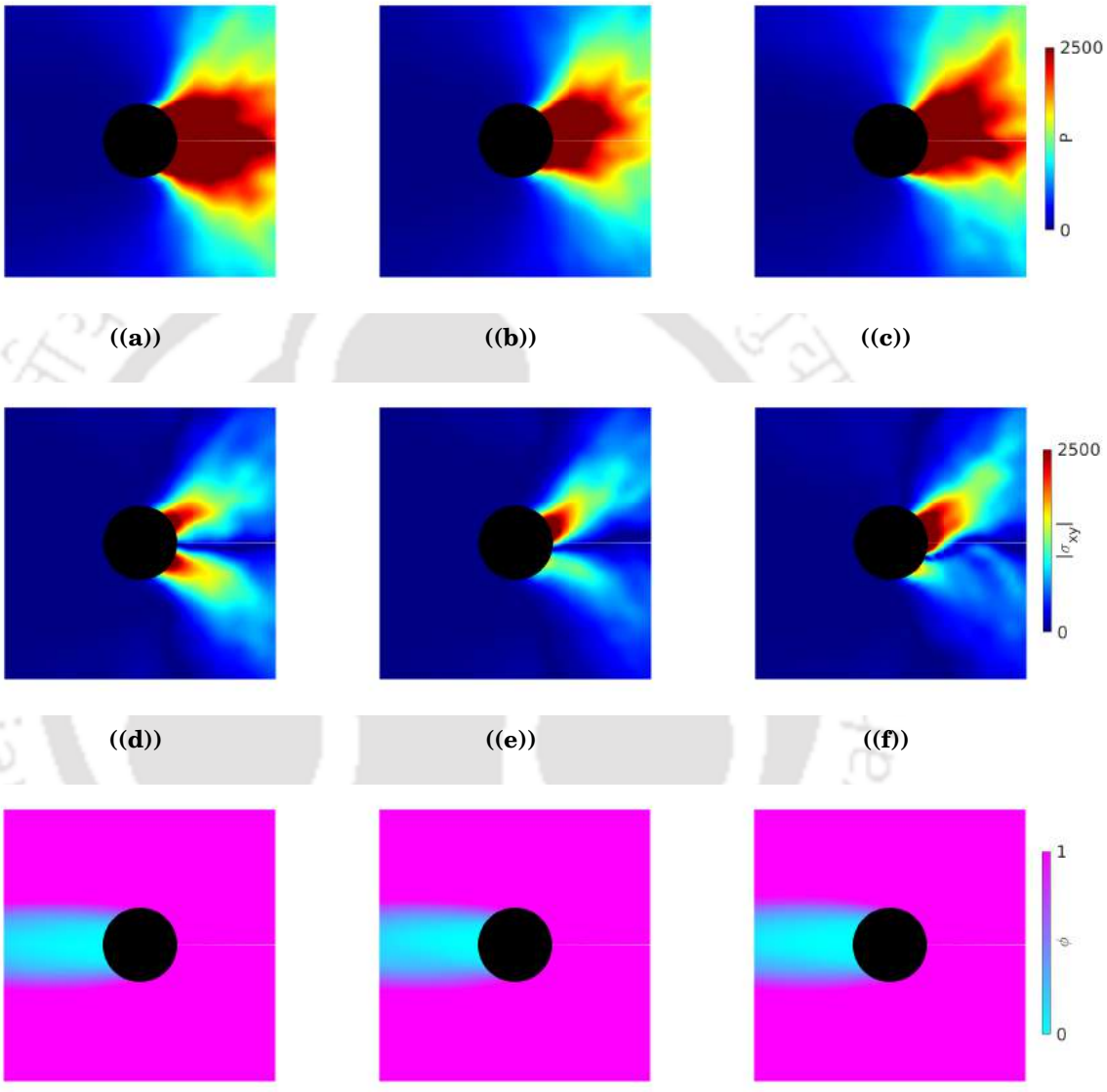

Figure 6.15: The time-averaged flow fields for depicting pressure P, shear stress $|\sigma_{xy}|$ and area fraction ϕ infront of the intruder for different spin ratio (Ω): (a), (d), (g) 0.0, (b) (e), (h) 1.0 and (c), (f), (i) 10.0. The velocity of the intruder is $V_i = 25cm/s$ and the fraction of dumbbell (X_{db}) in the system is 1.0.

BIBLIOGRAPHY

[1] Dietrich E Wolf, Farhang Radjai, and Sabine Dippel. Dissipation in granular materials. *Philosophical Magazine B*, 77(5):1413–1425, 1998.

[2] Sergiu C Dragomir, Mathew D Sinnott, S Eren Semercigil, and Özden F Turan. A study of energy dissipation and critical speed of granular flow in a rotating cylinder. *Journal of Sound and Vibration*, 333(25):6815–6827, 2014.

[3] Heinrich M Jaeger, Sidney R Nagel, and Robert P Behringer. Granular solids, liquids, and gases. *Reviews of modern physics*, 68(4):1259, 1996.

[4] Emilien Azéma, Farhang Radjai, and Gilles Saussine. Quasistatic rheology, force transmission and fabric properties of a packing of irregular polyhedral particles. *Mechanics of Materials*, 41(6):729–741, 2009.

[5] Sandip Mandal and DV Khakhar. A study of the rheology of planar granular flow of dumbbells using discrete element method simulations. *Physics of Fluids*, 28(10):103301, 2016.

[6] Raúl C Hidalgo, Balázs Szabó, Katalin Gillemot, Tamas Börzsönyi, and Thomas Weinhart. Rheological response of nonspherical granular flows down an incline. *Physical review fluids*, 3(7):074301, 2018.

[7] Carolyn Wightman and Fernando J Muzzio. Mixing of granular material in a drum mixer undergoing rotational and rocking motions i. uniform particles. *Powder Technology*, 98(2):113–124, 1998.

[8] Guy Metcalfe, Troy Shinbrot, JJ McCarthy, and Julio M Ottino. Avalanche mixing of granular solids. *Nature*, 374(6517):39–41, 1995.

[9] Julio M Ottino and DV Khakhar. Mixing and segregation of granular materials. *Annual Review of Fluid Mechanics*, 32(1):55–91, 2000.

[10] VN Dolgunin, AN Kudy, and AA Ukolov. Development of the model of segregation of particles undergoing granular flow down an inclined chute. *Powder technology*, 96(3):211–218, 1998.

[11] Jacob Uzan. Characterization of granular material. *Transportation research record*, 1022(1):52–59, 1985.

[12] Patrick Richard, Mario Nicodemi, Renaud Delannay, Philippe Ribiere, and Daniel Bideau. Slow relaxation and compaction of granular systems. *Nature materials*, 4(2):121–128, 2005.

[13] Isaac Newton. A letter of mr. isaac newton, professor of the mathematicks in the university of cambridge; containing his new theory about light and colors: sent by the author to the publisher from cambridge, febr. 6. 1671/72; in order to be communicated to the r. society. *Philosophical Transactions of the Royal Society of London*, 6(80):3075–3087, 2014.

[14] Benjamin Robins. *New Principles of Gunnery: Containing the Determination of the Force of Gunpowder, and Investigation of the Difference in the Resisting Power of the Air to Swift Ad Slow Motions.... By*

Benjamin Robins,... with an Account of His Life and Writings, by James Wilson, M. D. F. Wingrave, in the Strand, 1805.

[15] Gust Magnus. *Ueber die Abweichung der Geschosse nebst einem Anhange: Ueber eine auffallende Erscheinung bei rotirenden Körpern: Gelesen in dk Akad. d. Wiss. am 7 Aug. 1851 u. 17 Jun. 1852*. Dümmler, 1852.

[16] John D Anderson. Ludwig prandtl's boundary layer. *Physics today*, 58(12):42–48, 2005.

[17] WM Swanson. The magnus effect: a summary of investigations to date. 1961.

[18] Patrick D Weidman and Andrzej Herczynski. On the inverse magnus effect in free molecular flow. *Physics of Fluids*, 16(2):L9–L12, 2004.

[19] Jooha Kim, Haecheon Choi, Hyungmin Park, and Jung Yul Yoo. Inverse magnus effect on a rotating sphere: when and why. *Journal of Fluid Mechanics*, 754, 2014.

[20] Benzi John, Xiao-Jun Gu, Robert W Barber, and David R Emerson. High-speed rarefied flow past a rotating cylinder: the inverse magnus effect. *Aiaa Journal*, 54(5):1670–1681, 2016.

[21] Sonu Kumar, Manish Dhiman, and K Anki Reddy. Magnus effect in granular media. *Physical Review E*, 99(1):012902, 2019.

[22] P. A. Cundall and O. D. L. Strack. A discrete numerical model for granular assemblies. *Géotechnique*, 29(1):47–65, 1979.

[23] Yuka Takehara, Sachika Fujimoto, and Ko Okumura. High-velocity drag friction in dense granular media. *EPL (Europhysics Letters)*, 92(4):44003, 2010.

[24] Yuka Takehara and Ko Okumura. High-velocity drag friction in granular media near the jamming point. *Physical review letters*, 112(14):148001, 2014.

[25] I. Albert, J. G. Sample, A. J. Morss, S. Rajagopalan, A.-L. Barabási, and P. Schiffer. Granular drag on a discrete object: Shape effects on jamming. *Phys. Rev. E*, 64:061303, Nov 2001.

[26] Fuping Zhou, Suresh G Advani, and Eric D Wetzel. Simulation of the slow drag of a cylinder through a confined pressurized bed of dumbbell and elliptically cylindrical granules using the discrete element method. *Computer Modeling in Engineering and Sciences (CMES)*, 39(1):49, 2009.

[27] BJ Glasser and I Goldhirsch. Scale dependence, correlations, and fluctuations of stresses in rapid granular flows. *Physics of Fluids*, 13(2):407–420, 2001.

CHAPTER 7

CONCLUSIONS

The dynamics of submerged objects in dense granular media were investigated in this dissertation. In our research, we studied the movement of an intruder within dumbbell systems or systems that included both dumbbells and discs. The key findings of this dissertation is summarized as follows:

- The drag force gradually increases with velocity in a frictionless system but in a frictional system there is a constant drag regime at low velocities. For a fixed cross section, the drag force depends weakly on the intruder shape. The shape of the intruder has a significant effect on the distribution of contacts around its surface, which inturn is the main reason for the granular lift experienced by certain shapes.

- The drag force on a circular intruder translating through a heterogeneous mixture (disc and dumbbells) increases with the increase in the dumbbell fraction for a constant area fraction of the system. The presence of the dumbbell shape particle in the media offer additional resistance to the intruder in addition to the interparticle friction. The drag force on the intruder is also found to scale as the square of its velocity irrespective of the dumbbell fraction, the system area fraction or the intruder diameter. The mean flow field were presented for system of different dumbbell fractions. The time-averaged pressure was found to increase with increase in dumbbell fraction for a frictional system whereas for a frcitionaless system this pressure is almost same for different dumbbell fraction.

- The amplitude A/d, timeperiod $T/\sqrt{d/g}$ and intruder shape have a significant effect on the vertical dynamics of a horizontally oscilating intruder. For $A/d > 1$ the intruder objects show higher rate of sink for $T/\sqrt{d/g} = 1$. At an amplitude of $A \leq 1$ there is no significant vertical displacement of the intruder irrespective of the oscillating timeperiod. The time-averaged pressure field around the intruder informs that the pressure is higher at the base of the intruder for high $T/\sqrt{d/g}$ and pressure is lower for low values of $T/\sqrt{d/g}$. With the help of mathmatical model we identified an existence of a critical timeperiod beyond which the intruder object does not sink.

- A translating and rotating intruder in a heterogeneous granular mixture experiences a lift force for all non-zero spin ratios. In a normal fluid the direction of the lift force will be along the direction of spin however in granular medium it is opposite. This is due to the intruder's rotation, which causes a shift in the relative motion direction between the intruder and the surrounding granular particles, resulting in a lift. We found that the lift and drag ratio (F_L/F_D) saturates after a certain spin ratio within the granular medium. This is because at higher spin ratio most of the granular particles are found to slip through the intruder surface.

7.1 Scope for future work

Some interesting idea for the future work are summarized as:

- Understand the drag and lift on the intruder moving in a three-dimensional consisting of heterogeneous mixture of granules. In a three-dimensional system, it is simpler for particles to get out of the way of the intruder, therefore the dynamics should be considerably different.

- Force chains formation and breakage dynamics while the intruder is moving through a granular medium.

- To understand how the aspect ratio of the cylindrical intruder will effect its vertical displacement when oscillated within a dense granular medium.

- Study the impact of orientation for a triangular shape intruder on its rise or sink when oscillated horizontaly in a granular medium.

- Effect of the nature of the constituent granular particles on the rise/sink dynamics of oscillating intruders.
- The dynamics of a rotating and translating intruder through a three dimensional system.

List of Publications

.

Articles published

- Bitang Kwrung Tripur, Sonu Kumar, K. Anki Reddy and Julian Talbot. Role of shape on the forces on an intruder moving through a dense granular medium. *Praticulate Science and Technology*, pages 1-11, 2021.
- Bitang Kwrung Tripura, A. Vamsi Krishna Reddy, Sonu Kumar and K. Anki Reddy. Drag on a circular intruder traversing a shape heterogeneous granular medium. *Phys. Rev. E* (Accepted).

Manuscripts under preparation

- Bitang Kwrung Tripura, Sonu Kumar, A. Vamsi Krishna and K. Anki Reddy. Shape dependence on the rise and sink of a wiggling intruder. (for *J. Fluid Mech.*)
- Bitang Kwrung Tripura, A. Vamsi Krishna and K. Anki Reddy. Role of constituents of a granular medium on the lift force experienced by a translating and rotating intruder. (for *Physics of Fluids*)

Conferences attended

- Bitang K Tripura, Sonu Kurmar and Katha Anki Reddy, Effect of shape on the movement of an intruder object in dense granular medium. 12^{th} International conference on complex fluids and soft matter.(COMFLU-2018), Decemember 6-9, 2018, Indian Institute of Technology, Roorkee.
- Bitang K Tripura and Katha Anki Reddy, Dynamics of a horizontally wiggling intruder in a dense granular medium. International conference on advances in chemical engineering-2020.(AdChE-2020), February 5-7, 2020, University of Energy and Petroleum Studies, Dehradun.